REPORT DOCUMENTATION PAGE	Form approved OMB No.

1. AGENCY USE ONLY (LEAVE BLANK)	2. REPORT DATE	3. REPORT TYPE AND DATES COVERED
	10/2019	Final Report: 09/2017 – 10/2019

4. TITLE AND SUBTITLE	5. FUNDING NUMBERS
Development of a Computer Vision-Based Three-Dimensional Reconstruction Method for Volume-Change Measurement of Unsaturated Soils during Triaxial Testing	INE/CESTiCC 101418
6. AUTHOR(S) Xiong Zhang, and Xiaolong Xia	
7. PERFORMING ORGANIZATION NAME(S) AND ADDRESS(ES) Department of Civil, Architectural, and Environmental Engineering Missouri University of Science and Technology Butler-Carlton Hall Room 211 Rolla, MO 65409-0030	8. PERFORMING ORGANIZATION REPORT NUMBER INE/CESTiCC 19.28
9. SPONSORING/MONITORING AGENCY NAME(S) AND ADDRESS(ES) U.S. Department of Transportation 1200 New Jersey Avenue, SE Washington, DC 20590	10. SPONSORING/MONITORING AGENCY REPORT NUMBER FHWA-AK-RD-4000(137)
11. SUPPLENMENTARY NOTES	
12a. DISTRIBUTION / AVAILABILITY STATEMENT No restrictions	12b. DISTRIBUTION CODE

13. ABSTRACT (Maximum 200 words)

Problems associated with unsaturated soils are ubiquitous in the U.S., where expansive and collapsible soils are some of the most widely distributed and costly geologic hazards. Solving these widespread geohazards requires a fundamental understanding of the constitutive behavior of unsaturated soils. In the past six decades, the suction-controlled triaxial test has been established as a standard approach to characterizing constitutive behavior for unsaturated soils. However, this type of test requires costly test equipment and time-consuming testing processes. To overcome these limitations, a photogrammetry-based method has been developed recently to measure the global and localized volume-changes of unsaturated soils during triaxial test. However, this method relies on software to detect coded targets, which often requires tedious manual correction of incorrectly coded target detection information. To address the limitation of the photogrammetry-based method, this study developed a photogrammetric computer vision-based approach for automatic target recognition and 3D reconstruction for volume-changes measurement of unsaturated soils in triaxial tests. Deep learning method was used to improve the accuracy and efficiency of coded target recognition. A photogrammetric computer vision method and ray tracing technique were then developed and validated to reconstruct the three-dimensional models of soil specimen.

14- KEYWORDS : Triaxial Test, Three-Dimensional Reconstruction, Volume-Change Measurement, Ray Tracing, Computer Vision, Unsaturated Soils	15. NUMBER OF PAGES 129
	16. PRICE CODE N/A

17. SECURITY CLASSIFICATION OF REPORT	18. SECURITY CLASSIFICATION OF THIS PAGE	19. SECURITY CLASSIFICATION OF ABSTRACT	20. LIMITATION OF ABSTRACT
Unclassified	Unclassified	Unclassified	N/A

DEVELOPMENT OF A COMPUTER VISION-BASED THREE-DIMENSIONAL RECONSTRUCTION METHOD FOR VOLUME-CHANGE MEASUREMENT OF UNSATURATED SOILS DURING TRIAXIAL TESTING

FINAL REPORT

Prepared for

Center for Environmentally Sustainable Transportation in Cold Climates

Author(s):

Xiong Zhang, Ph.D., P.E.

Xiaolong Xia, Ph.D. Student

Missouri University of Science and Technology

INE/CESTiCC 19.28

October 2019

DISCLAIMER

This document is disseminated under the sponsorship of the U. S. Department of Transportation in the interest of information exchange. The U.S. Government assumes no liability for the use of the information contained in this document. The U.S. Government does not endorse products or manufacturers. Trademarks or manufacturers' names appear in this report only because they are considered essential to the objective of the document

ACKNOWLEDGMENTS

The authors wish to express their appreciation to the USDOT Tier 1 Center for Environmentally Sustainable Transportation in Cold Climates (CESTiCC) for providing the financial support to this research project. The authors would also like to thank all members of the Project Technical Advisory Committee. Acknowledgment is extended to Dr. Zhaozheng Yin, student Sara Fayek, and previous students Wei Luo and Dr. Lin Li for their valuable contributions with material collection, laboratory testing, and data analysis related to the project.

TABLE OF CONTENTS

LIST OF FIGURES

LIST OF TABLES

EXECUTIVE SUMMARY

Problems associated with unsaturated soils are ubiquitous in the U.S., where expansive and collapsible soils are some of the most widely distributed and costly geologic hazards. Solving these mentioned wide spread geohazards requires a fundamental understanding of the constitutive behavior of unsaturated soils. In the past six decades, suction-controlled triaxial test has been established as a standard approach to characterize constitutive behavior for unsaturated soils. However, this type of test requires advanced and usually costly test equipment (a double-wall cell testing system typically costs $150,000, only few research universities have the equipment in the U.S.), time-consuming testing processes (2-3 years for characterization of one soil), and the measurements are highly unreliable. These have been some of the major obstacles to the advancement, dissemination, and implementation of unsaturated soil mechanics and potentially lead to billions of dollars of loss each year.

The aim of this study was to develop an accurate, efficient, and cost-effective 3D reconstruction method to measure both global and localized deformation of unsaturated soils during triaxial tests. To this end, literature review was performed first to summarize the progress and limitations of previous studies related to triaxial tests on unsaturated soils, target recognition, and 3D reconstruction. Then, a deep learning-based method was developed to accurately and efficiently detect the coded targets on the triaxial cells and soil membranes. The ID numbers of each coded target were also determined using image processing techniques. Using these coded

target detection results as input, a 3D reconstruction approach was proposed for determining the 3D points on the triaxial cell and frame rods. A multi-ray tracings technique was proposed to correct the refraction occurring at the air-acrylic cell-interface and the acrylic cell-water interface. The 3D points on the unsaturated soils can also be obtained. Finally, the application of the photogrammetric method has been extended to the geosynthetics tests. A multi-cameras-based photogrammetric method was developed and used to measure the 3D full-field displacements of the geogrids.

A deep learning-based method for highly accurate target recognition was developed. In this method, a multi-stage detection approach using a faster R-CNN algorithm and a transfer learning technique was proposed. The triaxial cell detection, sub-region detection, and target detection were performed consecutively. This multi-stage detection approach has been proven to be five times more efficient than the template matching method. Based on the deep learning aided target recognition results, the high precision target center was obtained by the image processing technique. Results indicated that the average pixel coordinates difference obtained from the proposed method and commercial software is only 0. 1 pixel.

Validation of the proposed target recognition method has been performed on a cylinder and a triaxial cell, respectively. The cylinder recognition performed with 96.7% accuracy using 30 test images. The triaxial recognition performed with 100% accuracy using 120 test images. The target identification tests on both cylinder and the triaxial cell were capable of achieving a nearly 100% accuracy.

This study demonstrated that the deep learning aided target recognition method is suitable for target recognition even with a relatively small image dataset. In addition, a targets recovery algorithm has been proposed to recognize more targets. The proposed approach produces highly automated and accurate target recognition results which can be further used as input to 3D reconstruction projects for many different applications, such as volume-change measurement of unsaturated soils.

A joint approach from both photogrammetry and computer vision determined the camera poses from which the accurate 3D models of the unsaturated soils were proposed. Since it makes full use of the benefits of both photogrammetry and computer vision, this joint approach has the advantages of both high-accuracy and high-efficiency. The performance of this proposed method was validated by computing the camera poses and reconstructing the 3D models of a cylinder sample.

A method capable of creating accurate 3D models of target objects, like unsaturated soil specimens, from multiple views in a highly automated way, was also developed in this study. Combined use of computer vision technique and photogrammetry enables the 3D reconstruction process to be highly automated and accurate .The whole process was implemented in a Matlab program. Validation test results indicate that the relative error of our method is 0.067%. This method is easy to integrate with a newly proposed ray tracing technique and a fully automated and accurate program for measuring volume changes of unsaturated soil specimens in triaxial tests can be obtained.

A multi-camera-based photogrammetric method which extends from one-camera based photogrammetry to multi-camera based photogrammetry was also developed. This method can be successfully used in dynamic tests where the displacements continue to increase such as tensile tests on geosynthetics. The proposed photogrammetric method is a non-contact, cost-effective and highly accurate method. It is equivalent to installing unlimited non-contact LVDTs on the geosynthetics with high accuracy and large measurement ranges. Thus, much more information regarding the deformational and strength properties, such as displacement, strain, modulus and tensile strength at any locations of the geosynthetics can be obtained from the proposed photogrammetric method. Apart from conventional tensile test equipment, it only requires two commercially available digital cameras which cost about $ 2000. The average absolute difference in displacement obtained by the machine and the proposed photogrammetric method is 0.25%, and the average absolute error is 0.038 mm.

CHAPTER 1 INTRODUCTION

1.1 Problem Statement

Problems associated with unsaturated soils are ubiquitous in the U.S., where expansive and collapsible soils are some of the most widely distributed and costly geologic hazards. Expansive soils cover one-fourth of the U.S., and damage to infrastructure from expansive clays alone is estimated at $15 billion/year (Wray and Meyer 2004). According to the American Society of Civil Engineers' (ASCE) 2009 Report Card for America's Infrastructure, the infrastructure system in the U.S. has a grade of D. Most infrastructure is constructed on compacted soils that are typically unsaturated above the ground water table. Spiker and Gori (2003) reported that nearly all landslides in the U.S. are related to unsaturated soils and are rainfall-induced. Landslides result in 25–50 deaths/year and more than $2 billion/year in repair costs. Solving the above-mentioned wide spread geohazard requires a fundamental understanding of the constitutive behavior of unsaturated soils. In the past six decades, suction-controlled triaxial test has been established as a standard approach to characterize constitutive behavior for unsaturated soils. However, this type of test requires advanced and usually costly test equipment (a double-wall cell testing system typically costs $150,000, only few research universities in the U.S. have the equipment.), time-consuming testing processes (2-3 years for characterization of one soil), and the measurements are highly unreliable (Delage 2000). These

have been some of the major obstacles to the advancement, dissemination, and implementation of unsaturated soil mechanics and potentially lead to billions of dollars of loss each year.

Recently Zhang et al. (2015) proposed a new photogrammetry-based method to measure full-field deformations of unsaturated soils during triaxial testing. Only a digital camera (less than $2,000) is needed to measure the volume change of unsaturated soils during triaxial testing using the conventional triaxial test apparatus for saturated soils. Validation tests indicated that the average point position and volume change measurement accuracies were 0.065 mm and 0.05%, respectively. The proposed method will give almost every university and consulting firm who owns a conventional triaxial cell the ability to perform tests for unsaturated soils at a lower cost and higher accuracy than more advanced testing techniques. The major limitation of the proposed method is that it is very computation intensive. A prototype program called PhotoSoilVolume has been developed to facilitate the needed calculation. However, the program still needs further improvement, validation, and debugging before use by an ordinary laboratory technician.

1.2 Background

Triaxial test is commonly used to characterize both saturated and unsaturated soils. The volume or volume change of a soil is an essential parameter in understanding the deformation and strength properties of the soil. For triaxial test on a saturated soil, soil volume change can be directly measured through monitoring water exchange. For an unsaturated soil, due to the presence of air phase, the soil volume change is no longer equal to the change in water volume.

As a result, the conventional method to measure volume change of saturated soils cannot be used. In the past few decades, several methods have been developed to measure unsaturated soil volume changes during triaxial testing as summarized by Geiser et al. (2000), Sharma et al. (2006), Laloui et al. (2006), Hoyos et al. (2009), and Zhang et al. (2015). Table 1.1 compares the pros and cons of the existing methods.

Table1.1 Existing methods for total and local volume changes for unsaturated soils

Method	Require Modification ?	Deformation	Error Source	Accuracy	Cost	Reference	Comment
Double Cell System	Yes	Total	Water absorption, leakage, Air bubbles in channel	>0.25%	$50K-$150K	Bishop and Donald (1961) Sharma (1998)	Widely Used Difficult to calibrate
Differential Pressure Transducer	Yes	Total	Water absorption, leakage Air bubbles in channel	>0.25%	$50K-$150K	Ng et al. (2002)	Difficult to calibrate
Measurement of Air and Water Volume Changes	Yes	Total	Air Dissolution, Water Evaporation, Air bubbles	>0.25%	$30K	Geiser (1999)	Rarely used
LVDT	No	Local	Clamping problems	0.001mm	$1K/each	Blatz and Graham (2000)	Commonly used
Digital Image Analysis with Refracion Correction	No	Local	Refracion	0.2-0.3mm	<$2K	Macari et al. (1997) Sachan and Penumadu (2007)	Chamber deformation neglected Difficult to determine camera location
Digital Image Correlation	No	Local	Refracion	>5% (V)	<$2K	White et al. (2003)	Used in air only
Laser Scanner	Yes	Local	Refracion	>5% (V)	>$30K	Romero et al. (1997)	Boundary detection only
X-ray CT	Yes	Total & Local	Density correlation Boundary detection	>0.02mm	$200K-$2M	Desrues et al. (1996)	A completely new system For small size specimen
Photogrammetry with Refraction Correction	No	Total & Local		<0.008mm <0.25%	<$2K	This Study	Can use equipment for saturated soils No modification at all, high accracy

The double-wall cell method, proposed by Bishop and Donald (1961), is the most extensively used method for unsaturated soil volume change measurements. An inner cell was added to the conventional triaxial test apparatus and equal cell pressure was applied on both sides to ensure no lateral deformation of the inner cell. The volume change of the soil was then deduced by measuring the variation of the mercury level in the inner cell. Several modifications were made on the double-wall cell method later by Wheeler (1988), Cui and Delage (1996), and Ng et al. (2002). The double-wall cell method requires major equipment modifications on the conventional triaxial test apparatus for saturated soils and is expensive. A typical double-wall cell triaxial testing system costs over $100,000 and is complex to operate. The volume change

measurement accuracy can be influenced by water absorption of the inner cell. For the non-transparent inner cell, it is difficult to examine the existence of air bubbles in the chamber which is difficult to remove. A carefully calibrated double-wall cell can measure total volume change to an accuracy of 0.25% (GDS 2009).

Besides the double-wall cell method, other methods have also been developed to measure the volume change of unsaturated soils such as direct measurements of the air and water volumes using digital pressure volume controllers (Adams et al. 1996; Geiser 1999; and Laudahn et al. 2005), local displacement measurement using miniature LVDTs (Clayton et al. 1989), Hall Effect transducers (Clayton and Khatrush 1986), and profile determination using laser scanners (Romero et al. 1997). As pointed out by Geiser et al. (2000), Sharma et al. (2006), Hoyos et al. (2009), and Zhang et al. (2015), these methods also have their limitations and were not widely used.

With the increasing availability of inexpensive digital cameras, more and more image-based methods have been developed for soil deformation measurements during triaxial testing. The most widely used image-based method is presented by Macari et al. (1997). A stationary camera was mounted “far away” from the triaxial system. Images were captured for the soil specimen in the triaxial cell during loading. A two-dimensional (2D) refraction correction model (Parker 1987) was adopted to correct the magnification due to refractions caused by the confining fluid and triaxial cell wall. By detecting the edges of the specimen through the captured images, volume changes of the tested specimen were computed by assuming the soil

specimen always maintains a circular shape at any height. To implement the 2D refraction correction model, other requirements needed to be satisfied: (1) the soil specimen and the confining acrylic chamber are perfectly cylindrical and installed vertically; (2) the shooting direction of the digital pinhole camera exactly passes through the center of the chamber; (3) the soil specimen is installed exactly at the center of the confining chamber; (4) deformation of the acrylic cell wall under water pressure is negligible; and (5) the relative positions of the pinhole camera, triaxial chamber, and the soil specimen are accurately known. Zhang et al. (2015) indicated that none of the above assumptions hold true. With the similar system setup and refraction correction model, Lin and Penumadu (2006) presented a new image-based method to analyze the soil deformations in a series of combined axial-torsional tests under undrained condition. Instead of edge detecting, measurement points in a grid pattern with spacing of 10 mm were marked on the membrane which covered the soil specimen. The movements of these measurement points were tracked during testing through digital image analysis technique. The system setup in Macari et al. (1997) was also adopted by Gachet et al. (2007) to measure soil volume changes during triaxial testing. However, in this case, several calibrations, which included perspective correction, axial, and radial calibrations, were performed as a replacement of the 2D refraction correction model to correct the magnification effect due to the confining fluid and triaxial cell wall. For these image-based methods (Macari et al. 1997; Lin and Penumadu 2006; and Gachet et al. 2007), due to the difficulties in accurately determining the locations of the camera station and the triaxial cell for refraction correction, a sophisticated

system calibration is required for volume change measurement. Furthermore, the measurement accuracy of the image-based methods is not high. As addressed in Lin and Penumadu (2006), the obtained measurement accuracy was reported to be 0.2 mm and 0.3 mm in the vertical and circumferential directions, respectively. In Gachet et al. (2007), the volume measurement accuracy was determined to be 0.6%.

According to recent findings (Alshibli et al. 2000; Rechenmacher and Saab 2002; Desrues 2004; and Rechenmacher 2006), in addition to volume change, localized deformation has a significant impact on soil behavior. As addressed in Sachan and Penumadu (2007), strain localization is considered to be a major factor which controls the overall mechanical response of the soil, at or near failure. The development of appropriate constitutive models for these soils and the appropriate quantification of their failure states depends on accurate experimental quantification of shear band formation, growth, and evolution. Meanwhile, more and more attention has drawn on the investigation of localized deformation in soil during triaxial testing (Lin and Penumadu 2006; Rechenmacher 2006; Sachan and Penumadu 2007; Rechenmacher and Medina-Cetina 2007; and Bhandari et al. 2012).

In Lin and Penumadu (2006) and Sachan and Penumadu (2007), strain localization was obtained based on the deformation of the point grid. Digital image correlation (DIC) technique has also been utilized for soil deformation measurements during triaxial testing. (Rechenmacher 2006; Rechenmacher and Medina-Cetina 2007; and Bhandari et al. 2012). When using the DIC technique, the displacement measurement is derived by mapping between digital images

overlapping subsets of pixels or overlapping clusters of sand grains at many points across the specimen surface. However, in Rechenmacher (2006) and Rechenmacher and Medina-Cetina (2007), due to the difficulties in dealing with refraction, DIC cannot be directly used for deformation measurements on soils located in a triaxial chamber with or without confining fluid. Instead, the confining load was applied through vacuum pressure. Therefore, the applied confining load was limited to less than 100 kPa. Bhandari et al. (2012) reported the use of DIC technique for soil deformation measurements under triaxial condition. A 3D refraction model was developed to deal with the refractions at the interfaces of air-cell and cell-water. Three cameras around the testing system at intervals of 120^{o} were used to capture images of a deforming soil specimen at various instants. However, the deformation measurement using the DIC technique suffered many of the same limitations as those in the image-based methods Macari et al. (1997), Lin and Penumadu (2006), and Gachet et al. (2007) due to a similar system setup.

Until now, quantitative full-field 3D deformation measurement on unsaturated soils remained a great challenge for researchers. Recently, Zhang et al. (2015) proposed a new photogrammetry-based method to measure total and localized deformation of unsaturated soils during triaxial testing. In Zhang et al. (2015), the principle and mathematical derivation of the photogrammetry-based method were presented. Validation tests were performed on a stainless steel cylinder and a saturated sand specimen. The average point position and volume change measurement accuracies were evaluated to be 0.065 mm and 0.05%, respectively. The major

limitation of the proposed method is however that it is very computation intensive. This research developed a software which can overcome this limitation and make the novel technique available to any ordinary laboratory technician.

1.3 Objectives

The objective of this research is to further improve the software to accurately measure the total and local volume changes of unsaturated soil specimen during triaxial testing using the conventional triaxial test apparatus for saturated soils without any modification. Specifically, this software will use photographs taken by a commercial digital camera (less than $2000) to achieve measurement accuracies of 5-10 microns (μm) in length and 0.02%-0.05% in volume change for a soil specimen of 50mm in diameter and 100mm in height. This will be achieved by integrating computer vision-based target detection, photogrammetry, optical-ray tracing, and least-square optimization to reconstruct real-time 3D models for unsaturated soil specimen during shearing. In addition, laboratory testing procedures will be investigated for the newly developed method.

1.4 Structure of this Report

Chapter 2 reviews previous studies and current progress in characterization of unsaturated soils as well as the target recognition and 3D reconstruction approaches. The emphasis is on the existing volume change measurement methods for both saturated and unsaturated soils, methods to generate 3D mesh from point measurements, total and localized volume change calculation methods, and validation techniques.

Chapter 3 presents a deep learning aided target recognition approach for an improved photogrammetric method which is faster, simpler, fully automated and more accurate by using computer vision and image processing techniques. Faster R-CNN deep learning algorithm and fine-tuning technique will be used for target recognition.

Chapter 4 presents a method for 3D reconstruction from multiple views with combined use of computer vision technique and photogrammetry. In this method, coded target detection and camera calibration were performed first to obtain the input to the 3D reconstruction process. Then the camera poses and 3D points were estimated from the first two views, and the remaining views could be processed. Validation test results on a cylinder demonstrated that the proposed method can achieve high accuracy. Combining this method with a newly proposed ray tracing technique, a highly accurate and automated method for measuring the volume changes of unsaturated soil specimens in triaxial tests can be obtained. The method is then extended to multiple optical media to measure the total and local volume changes of soil specimens inside the triaxial cell. When a light ray passes through the water–acrylic and acrylic–air interfaces, it bends due to refractions. This disturbs the collinearity conditions and the proposed 3D reconstruction approach cannot be used directly any more. A ray-tracing technique is used to overcome this limitation. To apply the ray tracing technique, the geometric shape of the triaxial cell is required. Therefore determination of the shape and location of the triaxial cell is introduced first. Then the ray tracing process is discussed. Finally, based on multiple ray tracing

results, a least square optimization method is used to determine the 3D coordinates of points on the soil.

Chapter 5 presents an application of the proposed photogrammetry-based method on the tensile tests for geosynthetics. Conventional methods for measuring the deformational response of geosynthetics, such as LVDT, strain gauges, and extensometers have limitations in their ability to determine the complete strain distribution in geosynthetics. Recently an image-based method, which has many advantages over existing methods, was proposed to measure the deformational properties of geosynthetics. However, this method requires accurate manual control of the camera position and assumes that the geosynthetics remain planar during the entire testing process. Both of the requirements cannot be satisfied for several reasons, which can lead to misleading results. In this chapter, a multi-camera-based photogrammetric method was developed and used to measure the 3D full-field displacements of geosynthetics during tensile tests. A tensile test on a geogrid specimen was performed to verify the effectiveness and accuracy of the proposed photogrammetric method. This task is included in Chapter 5. Chapter 6 summarizes the literature survey and discussion of the results of other researchers, a description of the research methods and approach for this project, the test procedures and results, this project's findings, and suggestions for further study.

CHAPTER 2 LITERATURE REVIEW

2.1 Previous Studies of Triaxial Tests on Unsaturated Soils

Triaxial tests are commonly used to evaluate the stress-strain behavior of both saturated and unsaturated soils. In triaxial tests, the volume-change of a soil specimen is an indispensable parameter to determine and analyze. Triaxial test on saturated soils is relatively easy. This is because the volume change of the soil specimen is equal to the volume change of water. The volume-change of a saturated soil specimen can be obtained by measuring the amount of water which flows into and out of the triaxial cell. Triaxial tests on unsaturated soil, however, are much more complicated and challenging since the volume change of soil specimen is no longer equal to the volume change of water due to the existence of air phase in an unsaturated soil specimen.

To address this challenge, during the past several decades, many attempts have been made to measure the global and localized volume changes of unsaturated soils in triaxial tests, as summarized by Geiser et al.(2000), Laloui et al.(2006), Hoyos et al.(2009), Zhang et al.(2015), and Lin et al.(2015). Among these attempts, the double-wall cell system, proposed by Bishop and Donald (1961), is the most widely accepted method. An inner cell was added inside the conventional triaxial test apparatus and the equal cell pressure was applied to both sides of the inner cell so that there was no lateral deformation of the inner cell. As a result, the deformation of the soil can be measured by monitoring the volume-change of the mercury in the inner cell. Although the principle is theoretically sound and it indeed received considerable attention, there are several drawbacks to this method. As pointed out by Zhang et al. (2015) and Lin et al.

(2015), the expense is one of the major limitations of this method. A typical double-wall cell triaxial system costs over $100K and only a very limited number of universities and institutes can afford to purchase this equipment. In addition, this method is complicated to operate, and the calibration process is difficult and complex. Even though some researchers made modifications to the double-wall cell system (Wheeler, 1988; Cui and Delage., 1996; Ng et al., 2002), the abovementioned limitations still exist.

Other important developments include using digital pressure volume controllers for direct measurements of the air and water (Adams et al., 1996; Geiser 1999; and Laudahn et al. 2005), using LVDT for local displacement measurements (Clayton et al. 1989), and using laser scanners for profile determination. However, none of these methods have been widely used due to their limitations (Geiser et al. 2000; Hoyos et al. 2009, Zhang et al. 2015, and Lin et al. 2015).

Image-based methods are gaining more and more popularity in measuring the volume-changes of unsaturated soils in triaxial tests due to the availability of low-cost digital cameras. These methods include 2D refraction correction model (Macari et al. 1997, Lin and Penumadu. 2006) which is only for 2D measurements, and magnification effect correction model (Gachet et al. 2007) which requires sophisticated system calibration. In addition, as pointed out by Lin et al. (2015), the important parameters, such as the locations and orientations of cameras where the images were taken, cannot be accurately determined by these methods. Consequently, the accuracy of these methods is often a major concern.

More recently, Zhang et al. (2015) developed a photogrammetry-based method which can measure both the global and localized deformations of unsaturated soil during triaxial testing. In this method, a conventional triaxial test apparatus for saturated soils was utilized for triaxial tests on unsaturated soils. Only one commercially available digital camera was needed to take images of the triaxial tests from any arbitrary locations and orientations. The principle of this method is shown in Figure 1. The basic principle is photogrammetry. The camera positions and 3D model of the triaxial cell were determined by photogrammetric analysis in the air. The 3D model of the specimen was determined by a multi-ray tracing technique (Figure 1b) and a least-square optimization technique (Figure 1c). Since accurate camera positions were determined using photogrammetry this method can achieve high accuracy. The average point measurement and volume-change measurement accuracies were 0.065 mm and 0.05%, respectively.

In a somewhat similar way, Salazar et al. (2014) developed an internal camera-based method for measuring the volume-changes of unsaturated soils in triaxial tests using photogrammetry. The camera was placed inside of the triaxial cell to eliminate the refraction at the air-triaxial cell wall and triaxial cell wall-water interfaces. Photogrammetric analysis was performed to monitor the deformation of the specimen during triaxial testing. The capability of determining total and local strains, and total volume at any stage of triaxial testing was also validated. Although this method seems simple since refraction correction is no longer needed and it is capable of determining both total and localized strains, several concerns about this method have been raised by researchers (Lin et al. 2015). These include: (1) requirement of customized

camera; (2) requirement of saturation of camera in order to eliminate the refraction effect; (3) requirement of significant modifications of the triaxial test system; (4) the accuracy of the method affected by the blurred images taken in the silicon oil; and (5) the complicated image processing process. Therefore, many issues need to be addressed before this method can be used.

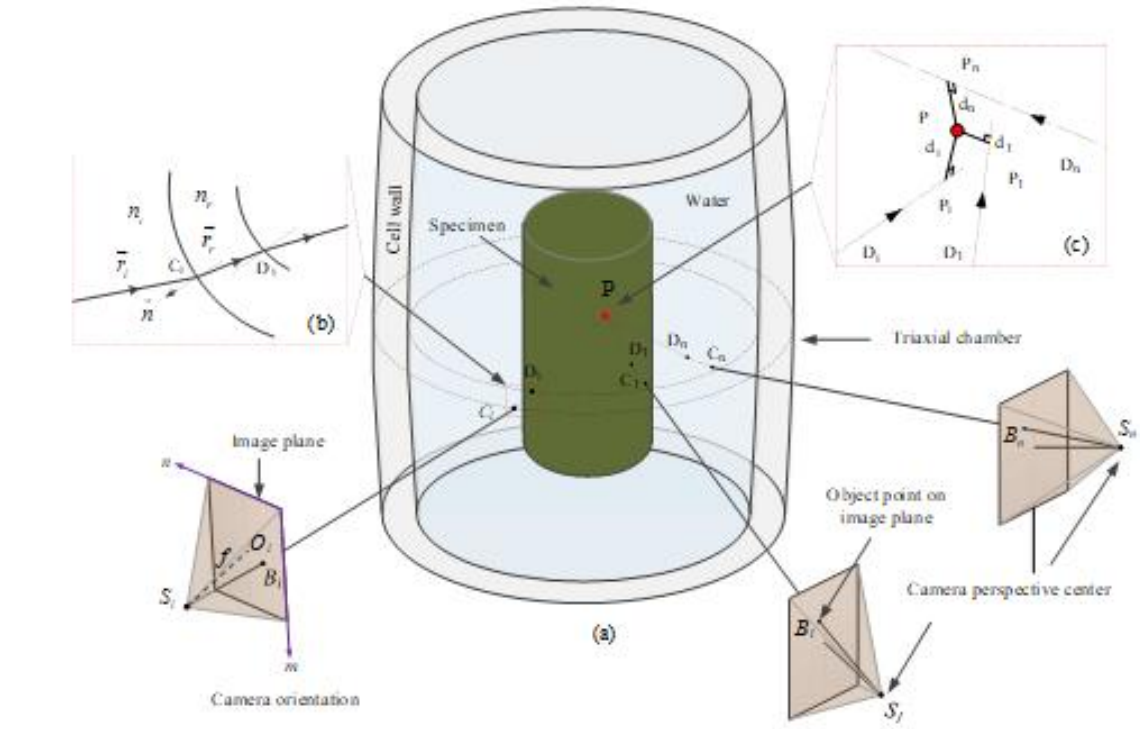

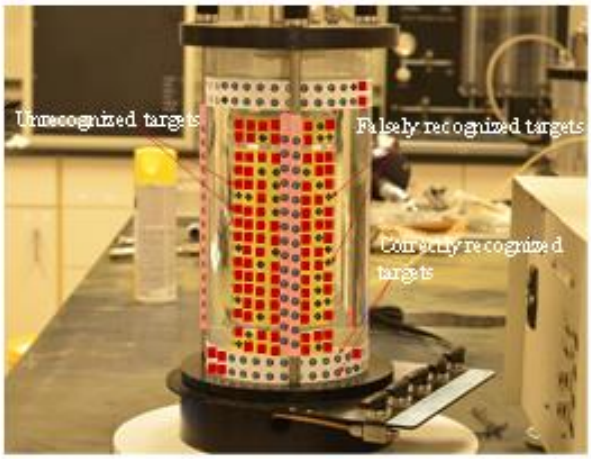

(d)

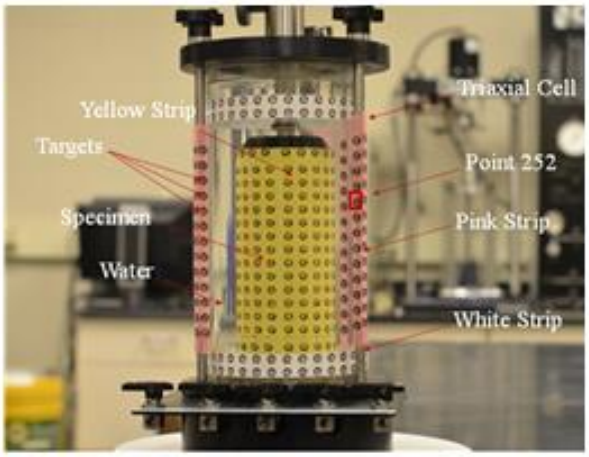

(e)

Figure 1.1 Principle of the photogrammetric method (modified from Lin et al., 2015) and system setup: (a) schematic representation, (b) ray tracing technique, (c) least-square optimization, (d) poor target recognition results, and (e) system setup of the proposed method.

The literature review indicates that the accurate and efficient volume-change measurement of unsaturated soils in triaxial tests remains a major challenge for researchers. Both the abovementioned photogrammetry-based method by Zhang et al. (2015) and the internal camera-based method by Salazar et al. (2014) use the principle of photogrammetry and have many advantages over other methods such as low-cost, high-accuracy, and both global and localized volume-change measurement. Therefore these two methods are expected to receive more attention. However, these methods still require improvements. In these methods, circular code targets, used to reconstruct the 3D models of the triaxial cell and specimen, are often posted on the triaxial cell and specimen (Figure 1.1d and 1.1e). Both methods rely on the use of commercial software for target recognition and photogrammetric analysis in the air for the triaxial cell. However, in many cases, many targets are falsely recognized or unrecognized by the commercial software. Figure 1.1d shows the typical target recognition results obtained from commercial software. In the figure, the circle denotes correctly recognized targets, the square denotes the unrecognized targets, and the cross denotes falsely recognized targets. As can be seen, a large percentage of targets were either unrecognized or falsely recognized. If the targets are falsely recognized, then both time-consuming and tedious manual correction of the target information is required, which leads to the low-efficiency of the photogrammetry-based method. On the other hand, if many targets are not recognized, this will influence the accuracy of the photogrammetry-based method. This is because the purpose of target recognition in the

photogrammetry-based is to obtain the target information which will be used in the subsequent 3D reconstruction of the triaxial cell and specimen. One critical step that ensures the high accuracy of 3D reconstruction projects is bundle adjustment, which is the problem of optimizing the 3D reconstruction results by jointly refining the 3D structure, camera positions, and camera parameters (Triggs et al. 2000). Bundle adjustment is actually an optimization process which requires information of large number targets to obtain better optimization results. Therefore, if many targets are not recognized, only the information of very limited number of targets can be used for 3D reconstruction and the photogrammetry-based method will be reduced. As a result, the poor target recognition is a major challenge to the efficiency and accuracy of the photogrammetry-based method. In fact, accurate and efficient target recognition is still a challenging problem in many fields, as it will be discussed in the next section. Therefore, this paper aims to develop a deep learning aided target recognition approach to improve the target recognition and photogrammetry-based method for measuring the volume-changes of unsaturated soils in triaxial tests. It is worth noting that the proposed approach can also be applied to the internal camera-based method.

2.2 Previous Studies of Target Recognition

As mentioned earlier, accurate and efficient target recognition is still a challenging issue for researchers. This will be demonstrated by the following literature review on target recognition. Targets have been widely used in photogrammetric measurement systems (Fraser, 1993; Moriyama et al., 2008; Luhmann et al., 2014; Scaioni et al., 2015). These targets are often

posted on the objects in order to obtain highly accurate three dimensional models of the objects for 3D measurement in photogrammetry. Many different types of targets have been used in practice. As summarized in Luhmann et al. (2013), the targets can be categorized into retro-reflective targets, circular targets, spherical targets, patterned targets, and coded targets. Among these targets, coded targets, dating from the 1990s, have been extensively used to facilitate the automated target detection, recognition, identification process. (Shortis and Seager, 2014). A summary of different coded target design and coding system can be found in Shortis and Seager. (2014)

One important component of photogrammetric measurement has been the automatic detection and recognition of targets, for example, coded targets (Fraser, 1993; Shortis and Seager, 2014). Some algorithms have been developed for automated target recognition and have been used in commercial metrology system (Knyaz and Sibiryakov, 1998; Ahn et al., 2001; Shortis and Seager, 2014). However, as pointed out by some authors, the target recognition task is challenging and difficult when the targets were subjected to a large perspective deformation, were freely rotated with regard to image frames and were displayed very large scale differences (Bernat and Tokarczyk, 2013). Zatarain et al. (2013) pointed out that many coded targets cannot be recognized by the photogrammetry system when the coded targets orientation with respect to the image axis is larger than 45°. This is consistent with the poor recognition results in the photogrammetry method in Figure 1.1d as mentioned previously.

Template matching is a common image processing technique used to determine the position of a given pattern in an image (Briechle and Hanebeck, 2001). This technique has also been used in coded target recognition (Barazzetti and Scaioni, 2010). In this method, the perfect image of the coded target, known as a template, is used to search in the whole image to find the image patch which has a very high similarity to the template by performing 2D normalized cross-correlation. However, this method can produce poor recognition results when there are scale and rotation variations, affine deformation, and illumination changes (Barazzetti and Scaioni, 2010). Accurate and robust target recognition is still a challenging issue in photogrammetric measurement.

2.3 Recent Advance in Deep Learning-Based Recognition

One possible solution to more accurate and robust target recognition is using deep learning to detect coded targets in images since the primary strength of deep learning has been in image analysis. Deep learning has shown an astonishing success during the last several years due to the availability of large datasets of images, increased computing power, and the development of algorithms (Mazurowski et al.2019). In the past several years, deep learning has also gained popularity in civil and infrastructure engineering applications (Cha et al. 2017; Yang et al. 2018). Soukup and Huber-Mork (2014) developed a convolutional neural network (CNN) for detecting railway defects in images under controlled conditions. Cha et al. (2017) proposed a deep learning-based method to detect the concrete cracks without calculating the defect features. The authors concluded that the proposed method is capable of detecting concrete cracks in realistic

situations. A faster region-based convolutional neural network (faster RCNN)-based structural visual inspection method was developed later to detect multiple structural damages in real time (Cha et al. 2018).Yang et al. (2018) developed a CNN-based deep learning architecture to predict pavement friction levels and demonstrated the potential of using deep learning for pavement friction evaluation.

Among the proposed CNN models, regions with convolutional neural network features (R-CNN), first proposed by Girshick et al. (2014), shows powerful object detection capability. R-CNN is a two-stage detection algorithm which combines region proposals with CNN features. The R-CNN has much better performance in terms of the accuracy of object detection in comparison with the CNN-based methods (Sermanet et al., 2014; Girshick et al., 2014; Cha et al., 2018). However, one limitation of R-CNN is that, an R-CNN detector generates region proposals and each region must be classified, thus is not efficient. Girshick (2015) proposed Fast R-CNN, where the entire image can be processed in a single stage. Fast R-CNN is more efficient and accurate than R-CNN. However, fast R-CNN is still slow and has limited accuracy due to the time-consuming selective search when generating object proposals. To improve fast R-CNN, a region proposal network (RPN) has been developed and implemented in Faster R-CNN, proposed by Ren et al. (2015). In Faster R-CNN, RPN was added to generate region proposals directly in the network. Faster R-CNN is faster in generating region proposals in the network and significantly increased the efficiency of object detection.

Transfer learning is commonly used in deep learning applications. One can take a pretrained network and use it as a starting point to learn a new task. Fine-tuning a network with transfer learning is usually much faster and easier than training a network with randomly initialized weights from scratch. You can quickly transfer learned features to a new task using a smaller number of training images. Fine-tuning a network is slower and requires more effort than simple feature extraction, but since the network can learn to extract a different set of features, the final network is often more accurate. Fine-tuning usually is better than feature extraction as long as the new data set is not very small because the network has data to learn new features from.

2.4 Multi-view 3D Reconstruction

Multi-view 3D reconstruction is a technology that allows the creation of 3D models of a given target scene from a series of 2D overlapping images obtained from a digital camera (Favalli et al., 2012). Due to its low cost and convenience, this technology has become more and more popular in geotechnical engineering. Kitahra et al. (2016) used 3D models obtained from multiple-view images to simulate rock fall. Oats et al. (2017) developed a method for retaining wall assessment based on 3D photogrammetry technique.

While promising, conventional 3D reconstruction techniques still suffer from significant limitations when dealing with optically challenging objects, for example, the unsaturated soil specimen in triaxial tests where multiple optical media (air, acrylic cell, water) are involved. This is because refraction will occur at the interfaces of two optical media, and conventional 3D reconstruction techniques cannot be applied directly.

To overcome this limitation, Zhang et al. (2015) proposed a method which integrated a ray tracing technique and 3D photogrammetry to correct the refraction and reconstruct the 3D models of unsaturated soil specimens. Based on these 3D models, the volume change of unsaturated soil samples was successfully calculated. In contrast with conventional 3D modeling techniques, this method has extended the 3D photogrammetric technique to multiple optical media, which seems a very promising technique for measurement of volume changes of unsaturated soil specimen in triaxial tests since it only requires one commercially available camera to take images from any arbitrary directions and locations. Additionally, both global and localized deformation of the soil samples can be measured and this method has been reported to have very good accuracy (Zhang et al. 2015, Li et al. 2015).

Many commercial software packages for image-based 3D modeling are available, but a program capable of deriving an accurate 3D model of unsaturated soil specimens considering refraction in a fully automated and efficient way from a series 2D experimental images is still missing.

Recent advancements in computer vision has enabled 3D modeling process to be highly efficient and automated. But its accuracy is rarely checked out and most results are primarily for visualization purposes (Barazzettia et al. 2009).

2.5 Gaps in the Body of Knowledge

Most research efforts in convolutional neural network applications in civil engineering are focused on structural damage detection. No results of deep learning aided target recognition

have been reported. On the other hand, the existing body of research on deep learning aided recognition is heavily skewed toward rough object detection and the location of the object in the images can only be estimated. While this detection result might be accurate enough in most vision tasks, applying deep learning aided detection techniques to the above-mentioned photogrammetry-based method for measuring the volume-changes of unsaturated soils needs to be very careful. This is because high precision target center data is required for the target recognition task in the photogrammetry-based method since this is essential information for the 3D reconstruction process. Considering the state of practice and body of research reviewed in the preceding sections, the following gaps in knowledge have been identified: (1) none of the existing methods tackle accurate, automated, and efficient target recognition, (2) no deep learning aided recognition method exists for automated and accurate target recognition for 3D reconstruction, and (3) there is no formal understanding of the challenges and limitations associated with adopting a deep learning aided target recognition in the photogrammetry-based method.

The objective of this study is to address gaps 2 and 3 by developing and testing a novel deep learning aided target recognition approach for automatically and accurately detecting targets for 3D reconstruction and volume-change measurement purpose. The authors examine the following research questions to accomplish this objective: 1. how can the powerful deep learning tool be utilized to allow accurate and automated target recognition? 2. What combination of deep

learning aided detection algorithm and image processing techniques will be required to produce the most desirable results?

In this research we present a method for fully automated 3D modeling of unsaturated soil specimens based on combined use of photogrammetry and computer vision techniques. As mentioned earlier, the accuracy is a big concern if computer vision technique is used for geotechnical purposes, the accuracy of our method will be carefully evaluated. It is worth noting that this method is easy to integrate with the ray tracing technique proposed by Zhang et al. (2015). Thus, a fully automated and accurate method for 3D modeling of unsaturated soil samples considering refraction can be obtained.

CHAPTER 3 CODED TARGET RECOGNITION AND IDENTIFICATION

3.1 Proposed Methodology

The proposed methodology involves a deep learning-aided approach that uses image acquisition to achieve the target recognition goal. Figure 3.1 illustrates the flowchart of the proposed method, which includes four major phases: target recognition using deep learning, image processing for recovering missing points, determination of target IDs, and determination of target center. After the 2D images were obtained by the digital camera, the images were processed for target recognition purpose using a deep learning algorithm called faster R-CNN. Next, an image processing technique was proposed to recover the missing targets in the images which were not successfully recognized, then the ID of each target was determined. Finally, the accurate center of each target was obtained using image processing technique.

3.1.1 Posting Targets on the Triaxial Cell

Figure 1.1e shows the system setup of the proposed method. As shown in Figure 1.1e, coded targets were posted on the triaxial cell, frame rods, and membrane at different locations. Specifically, there were two horizontal white strips which contained coded targets at the top and bottom of the triaxial cell. Multiple longitudinal pink strips with coded targets were posted on the triaxial cell as well as the frame rods.

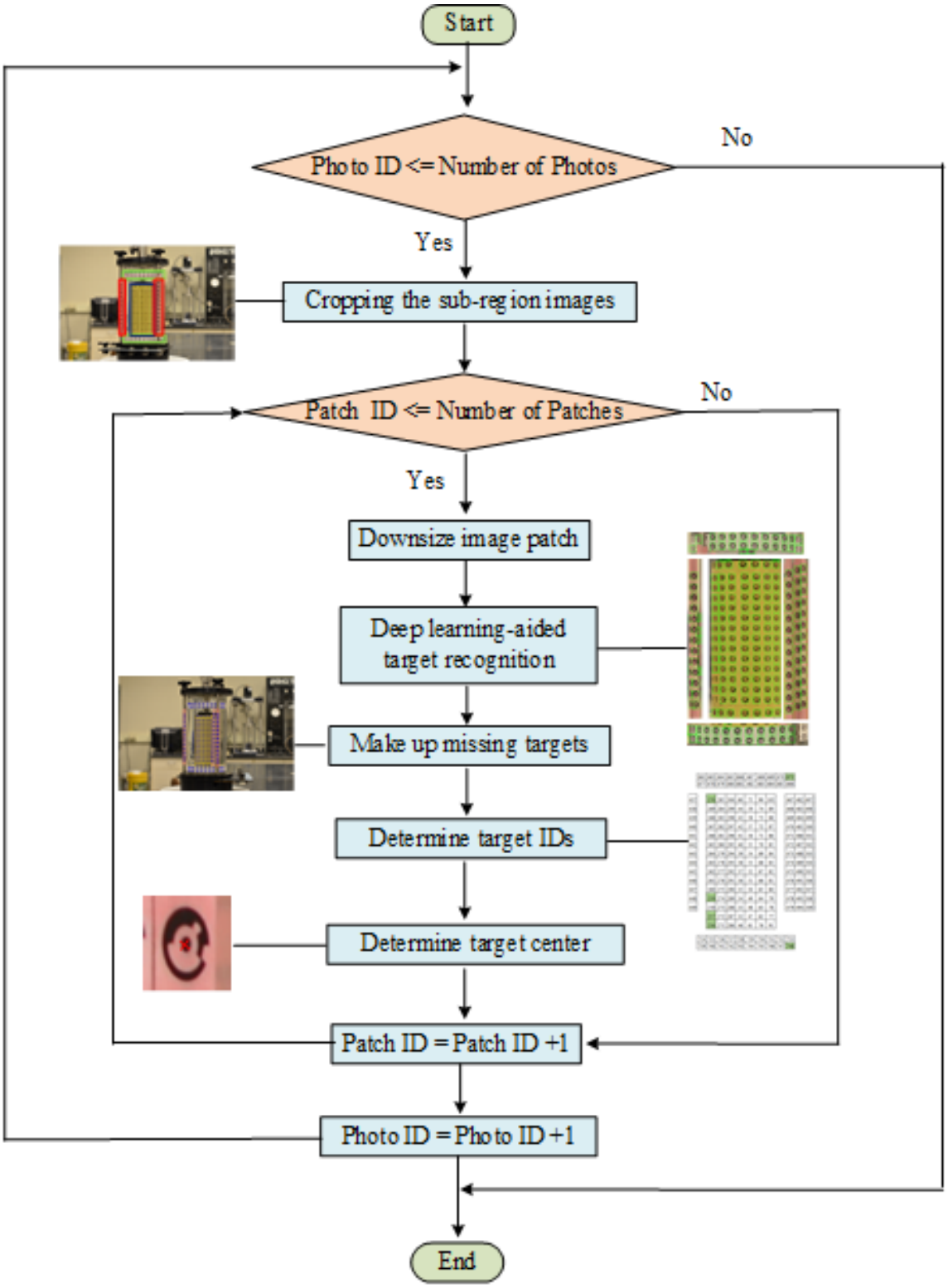

Figure 3.1 Flowchart of the proposed target recognition method.

The purpose of posting targets on the frame rods was to make full use of the space. This is because the view of targets behind the frame rods was blocked, and it is beneficial to add some targets on the frame rods to make the best use of the limited space for posting coded targets. Additionally, the coded targets were posted on the yellow membrane. For the convenience of description, the different aforementioned strips containing coded targets were called sub-regions.

3.1.2 Image Acquisition

A commercial Nikon digital camera was used for image acquisition. The camera parameters are listed in Table 3.1. Images of the triaxial cell in the lab from different angles were taken under normal lighting conditions. Approximately three hundred images were taken for training images and one hundred images were captured for testing images. It is worth noting that there were no specific requirements for the image acquisition process as long as the images were not blurred. This allows a novice without training to use the proposed methodology easily.

Table 3.1 Parameters of the camera used in this study

Focal length(mm)	Format size		Principal point		Radial distortion			Tangential distortion	
	Width(mm)	Height(mm)	P_X (mm)	P_Y (mm)	K_1	K_2	K_3	P_1	P_2
Before idealization									
55.7741	24.0022	15.8961	12.4170	7.9842	6.222×10^{-5}	0	0	2.205×10^{-5}	2.130×10^{-5}
After idealization									
55.7741	25.1509	16.6566	12.5754	8.3283	0	0	0	0	0

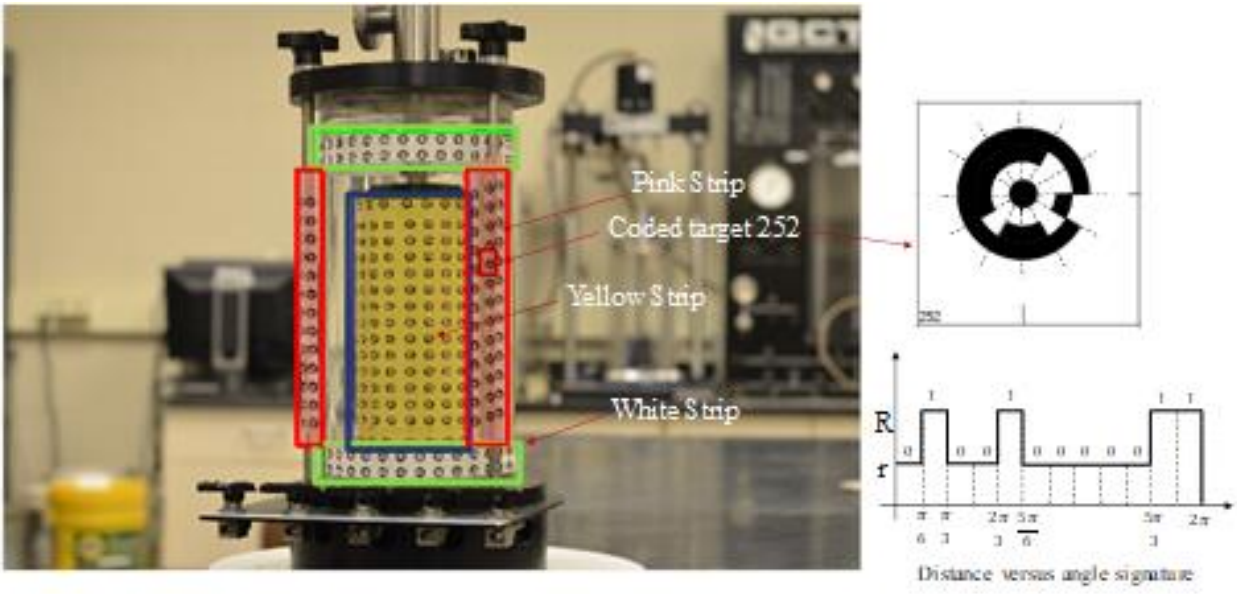
Pink Strip
Coded target 252
Yellow Strip
White Strip
R
r
Distance versus angle signature

(a) (b)

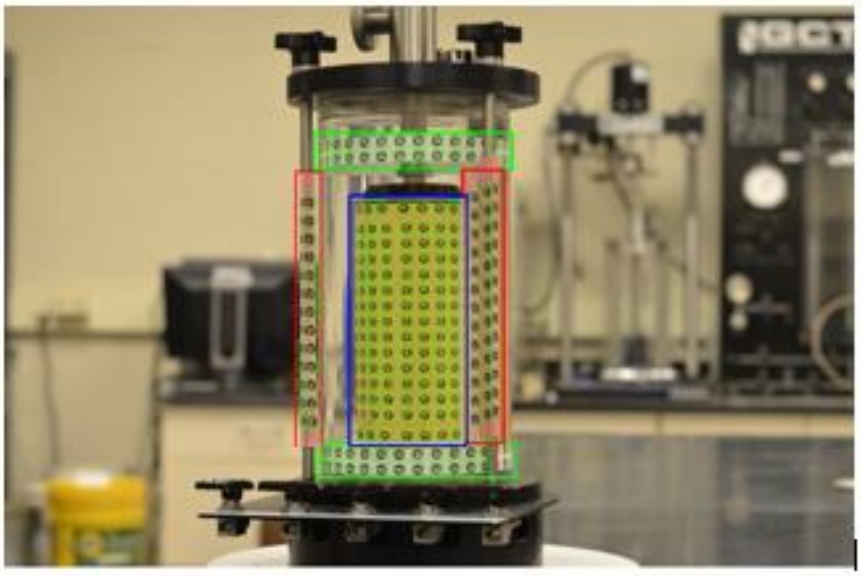

(c)

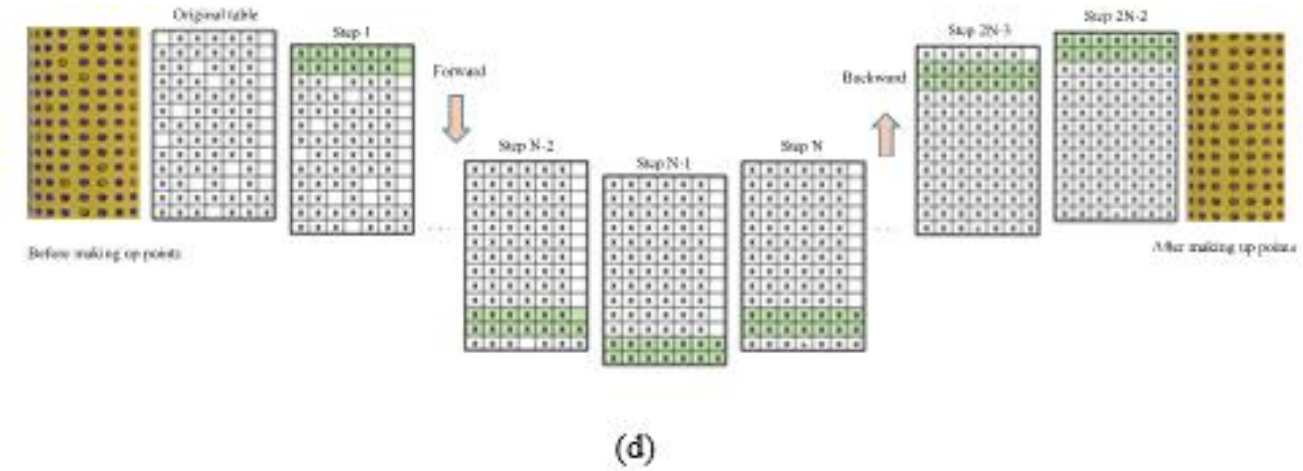

(d)

Figure 3.2 Deep learning-aided target recognition: (a) cropping the sub-region images, (b) a typical coded target, (c) bounding boxes of targets obtained from deep learning method, and (d) schematic plot of the proposed translation method for recovering lost points.

3.1.3 Image Preprocessing

After the images were collected, image preprocessing processes were done on each image. The objective of image preprocessing is to prepare the required images for training data. The first step is to downsize the original images. All the images were downsized by 256 (16 by 16) times for triaxial cell recognition and sub-regions recognition which will be discussed later. The purpose of downsizing images was to improve the recognition efficiency without influencing the recognition accuracy. Since the images processed were reduced by 256 times, the time required for recognition tasks was assumed to dramatically decrease. This assumption will be verified in the later section. After downsizing the images by 256 times, the triaxial cell image patches were manually cropped from the downsized images. These triaxial cell image patches

would be used as training data for sub-region recognition. The original images were downsized again for coded target recognition. However, this time they were only downsized by 16 (4 by 4) times. This is because coded targets were much smaller than triaxial cell and sub-regions and we wanted higher resolution images for coded targets recognition. Similarly, after downsizing the original images by 16 times, sub-region image patches were manually cropped from the downsized images. These sub-region image patches would be used as training data for target recognition.

3.1.4 Deep Learning Aided Target Recognition

In this approach, the triaxial cell detection was performed first. The recognized triaxial cell was then used as a new input image and the sub-region recognition was further performed. Finally, these recognized sub-regions served as input to CT detection. Figure 3.2a shows the results of this multi-stage recognition. The purposes of the multi-stage recognition were to improve detection efficiency and also reduce detection error. This is because when performing triaxial cell and sub-regions detection first, the size of images processed was much smaller. Additionally, there was less chance of recognition errors using the multi-stage recognition method.

In the multi-stage recognition method, three recognition tasks were mentioned. For each of these detection tasks, the object detectors were trained. These object detectors include triaxial cell detector, sub-regions detector, and CT detectors. To train these detectors, the labeled training data were created by manually labeling the area of interest in the images using Matlab Image

Labeler app. These training data were then fed to the machine to train faster R-CNN object detectors. There were four steps for each training process. Step 1 is training a Region Proposal Network (RPN); step 2 is training a fast R-CNN Network using the RPN from step 1 and extracting region proposals from all the training images; step 3 is re-training RPN using weight sharing with fast R-CNN; step 4 is re-training fast R-CNN using updated RPN.

Figure 3.2c shows the deep learning-aided target recognition results. The result of cropping sub-regions images is shown in Figure 3.2a. For each image, different sub-regions, namely top white strip, bottom white strip, pink strip, and yellow strip, were cropped and restored. Then deep learning recognition was performed on each sub-region image. Figure 3.2c shows the target recognition results using deep learning method. As can be seen in Figure 3.2c, most targets were successfully recognized. However, there were still some missing targets which were not recognized. This problem will be addressed in the following section.

3.1.5 Recovering the Lost Targets

In the last step, most code targets were recognized by the deep learning-based method. However, it is unavoidable that some coded targets were "missing", or not successfully recognized. In order to recover these missing targets, a translation method has been developed. Figure 3.2d shows a schematic plot of the proposed translation method for recovering lost targets. The yellow membrane strip was used as an example, and a similar method can be applied to white and pink strips. As can be seen in Figure 3.2d, the proposed method consists of two stages. The first stage involves recovering lost targets from top to bottom. This means that,

starting from the first row, the first row of targets were moved, or translated to the second row. Then the overlapping area between each target in the translated first row and that in the second row was calculated. An assumption was made herein that if the overlapping area is larger than 50% of the area of one coded target, it means there is no missing targets at the examined location, and there is no need to recover targets in this location. However, if the overlapping area is less than 50%, it means that there is a target in this location which is not recognized. Therefore, the unrecognized target should be made up in this location. Then, moving to the next row, the same procedures apply. This process is repeated until the bottom row of targets are processed. The second stage is in the opposite order in which the recovery method is applied from the bottom row to the top row. In this way, all the targets are successfully recognized as shown in Figure 3.2d.

3.1.6 Determination of the ID of Each Target

Each CT was designed to be unique. Figure 3.2b shows a typical CT. In the figure, six dotted lines were added to the CT for explanation. The six dotted lines divided the targets into twelve portions. Each portion was 30 degrees. If we evaluate the distances from the CT center to the CT boundary points, there were only two types of distances, larger distance R and smaller distance r. Then, number 0 was assigned to distance r and number 1 was assigned to distance R. Consequently, a distance versus angle plot called “signature” was obtained. This plot includes a series of binary numbers, 0 and 1, which was further converted into a decimal number. This decimal number is also the ID number of this CT.

The idea introduced above is the ideal case where the CT was standard and in circular shape. In most cases, however, the CTs appearing in the images were not in good image quality and in elliptical shape, resulting in an irregular signature. Thus, the histograms become much more irregular which makes the problem more challenging. The case becomes even worse when the shooting direction deviates far from the normal direction of the object surface. This is also the reason why many existing methods for coded target detection suffer from low detection accuracy. To overcome this problem, blob analysis is performed first to fit the coded targets using ellipses. Then we rotate the coded target to have the major axial parallel to the x-axis. After that we translate the boundaries of the coded target so that the centroid coincided with the origin. Finally the ellipses are normalized to circles by reducing the length of the major axis.

3.1.7 Determination of the Accurate Target Center

Although the deep learning aided target recognition method can find the rough locations of the targets, it cannot determine the accurate locations of the target center. This is because when we create training data for the targets, it is very difficult to manually mark the accurate target center. Figure 3.3d shows the procedures of using deep learning recognition results to find the target center. It is noted that typically a deep learning project produces bounding boxes of the candidate objects that are recognized. Figure 3.3a shows the bounding boxes of the targets obtained by deep learning method.

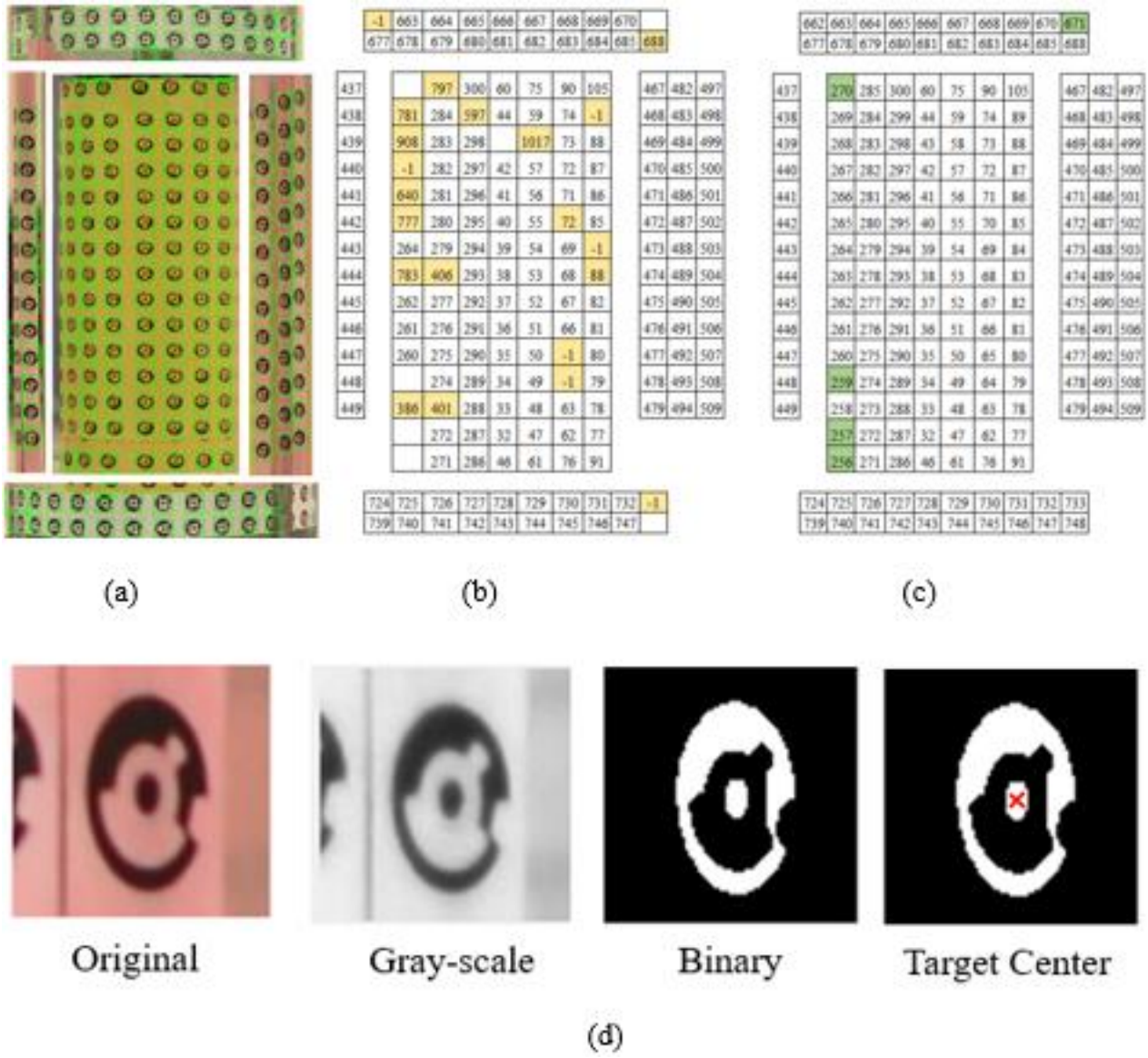

Figure 3.3 Target IDs results and determination of the accurate target center: (a) original target recognition results obtained from deep learning recogniton method, (b) target IDs before ID correction, (c) target IDs after ID correction, and (d) intermediate results of determination of accurate target center.

Consequently, the deep learning aided target recognition results cannot be used directly in the 3D reconstruction process. To address this problem, the image processing technique is used to determine the accurate target center. The procedures are introduced as follows: (1) Converting the original color image into a gray-scale image; (2) cropping an image patch for the target from the gray-scale image; (3) Converting the gray-scale image patch into a binary image patch; (4) Removing the noise information in the binary image patch; (5) Finding the centroid of the inner dot of the targets using blob analysis; (6) Adding correction of XY pixel coordinates into the initial guess of pixel coordinates. Steps (1) to (4) are explained in Figure 3.3d. These steps are applied to each of the targets. Figure 3.3d shows the results of refined pixel coordinates. In the figure, the cross denotes the center location. As can be seen in the images, after using the image processing techniques described previously, the accurate target center is determined.

3.2 Validation of the Proposed Method

3.2.1 Validation of the Efficiency of the Deep Learning-Aided Target Recognition Method

To evaluate the efficiency of the proposed target recognition method, the time taken for target recognition by the proposed method was compared with that by the template matching method. Template matching is a technique in digital image processing for finding small parts of an image which match a template image. It can be used in manufacturing as a part of quality control, a way to navigate a mobile robot, or as a way to detect edges in images. A basic method of template matching uses an image patch (template), tailored to a specific feature of the search image, which we want to detect. This technique can be easily performed on grey images or edge

images. The cross correlation output will be highest at places where the image structure matches the mask structure, where large image values get multiplied by large mask values.

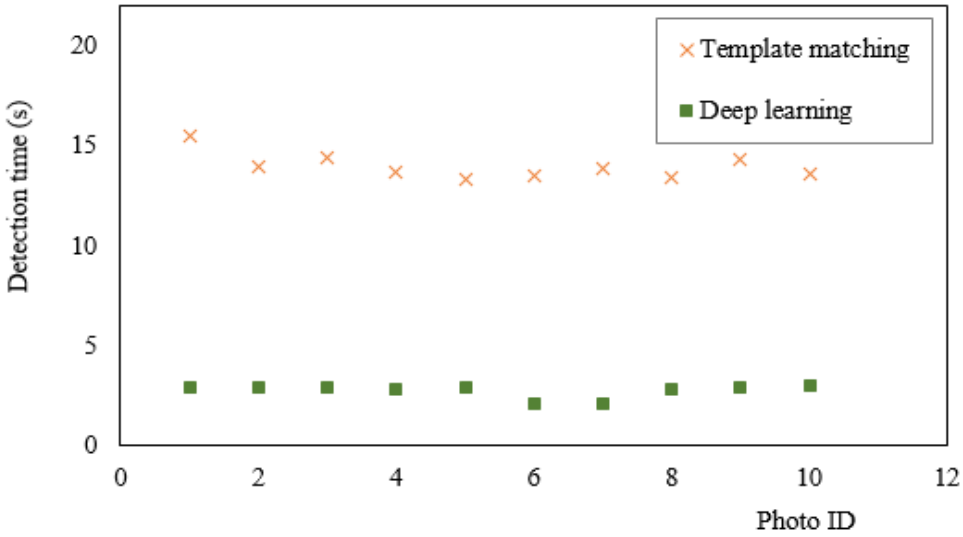

(a)

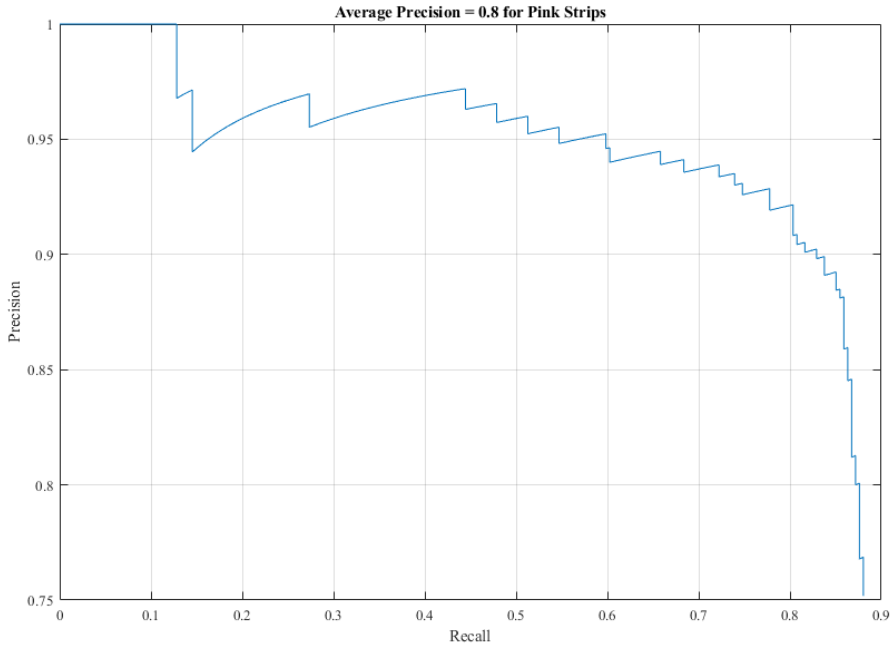

(b)

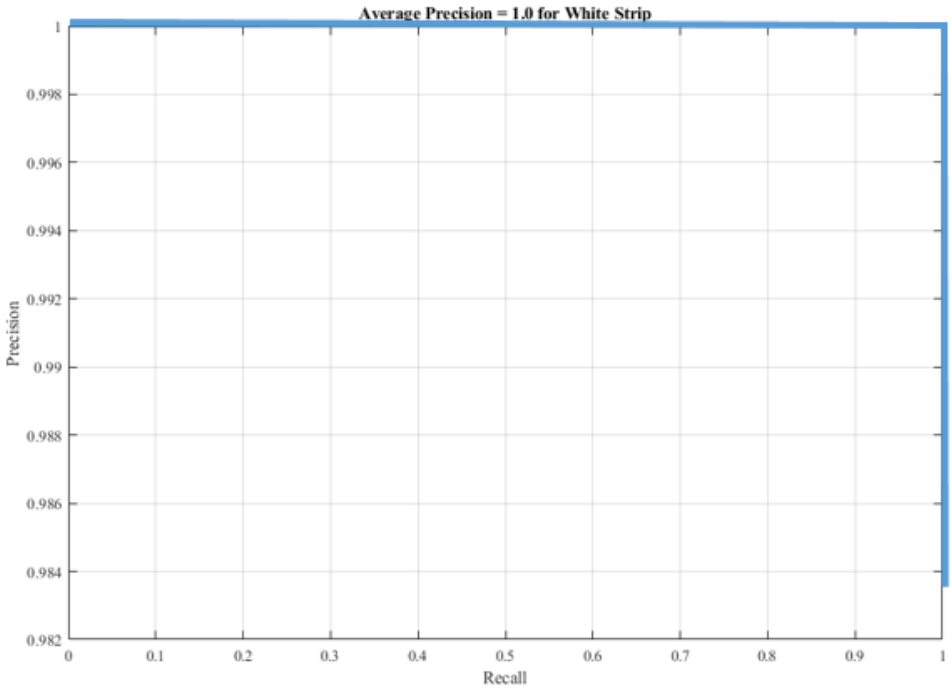

(c)

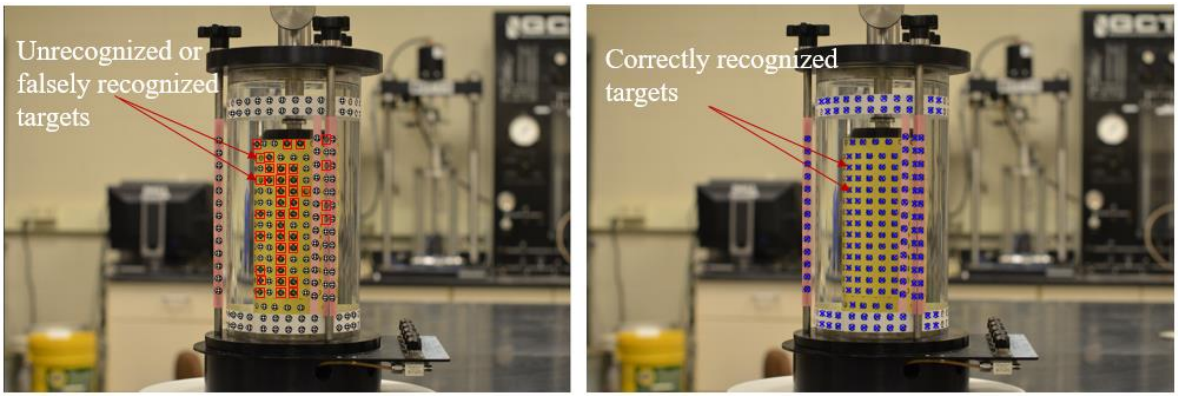

(d) (e)

Figure 3.4 Validation of the deep learning-aided target recognition method and the unrecognized targets recovery algorithm: (a) Validation of the efficiency of the deep learning aided target recognition method, (b) Validation of the accuracy target recognition results for pink strips, and (c) Validation of the accuracy target recognition results for white strips, (d) target recognition

results obtained from commercial software, and (e) target recognition results obtained from the our method.

Figure 3.4a presents the comparison in terms of detection time by the two methods. It can be seen that the average time spent on an image for template matching method is 14 seconds while only an average of 3 seconds is spent on one image using the deep learning method. This indicates that the deep learning method is almost five faster than the template matching method. This will greatly improve the efficiency of target recognition. One possible reason for the high detection efficiency of deep learning method is that while the training stage of a deep learning project may take a little longer time, the testing stage when the detectors are used for target recognition takes much shorter time. This explains why the proposed deep learning method for target recognition is much faster.

3.2.2 Validation of the Deep Learning-aided Target Recognition Algorithm

The performance of the proposed target recognition method was evaluated. For this purpose, the target recognition results obtained by the proposed deep learning method were compared with groundtruth of the target locations of the same images. The groundtruth of the target locations was obtained by careful manual cropping of the area required to be recognized using the Matlab Image Labeler App. Three key performance metrics were applied: recall, precision, and accuracy. Recall, also identified as sensitivity, measures the detection completeness. Precision refers to the detection exactness or reliability, while accuracy describes

the average detection correctness. Figure 3.4b and 5c presents the results calculated with this procedure. The figure demonstrates that the proposed method attained an average precision of 0.8 for pink strips and an average precision of 1.0 for white strips. Therefore, the proposed method can achieve very high accuracy for target detection from the point of view of deep learning object detection. Although this shows promising results for target recognition, we also mentioned earlier that the deep learning recognition results cannot produce accurate target center results, and the thus cannot be directly used for 3D reconstruction purpose. Therefore we proposed an image processing technique to refine the locations of the target centers, and we demonstrated that by using the image processing results the accurate target centers can be determined.

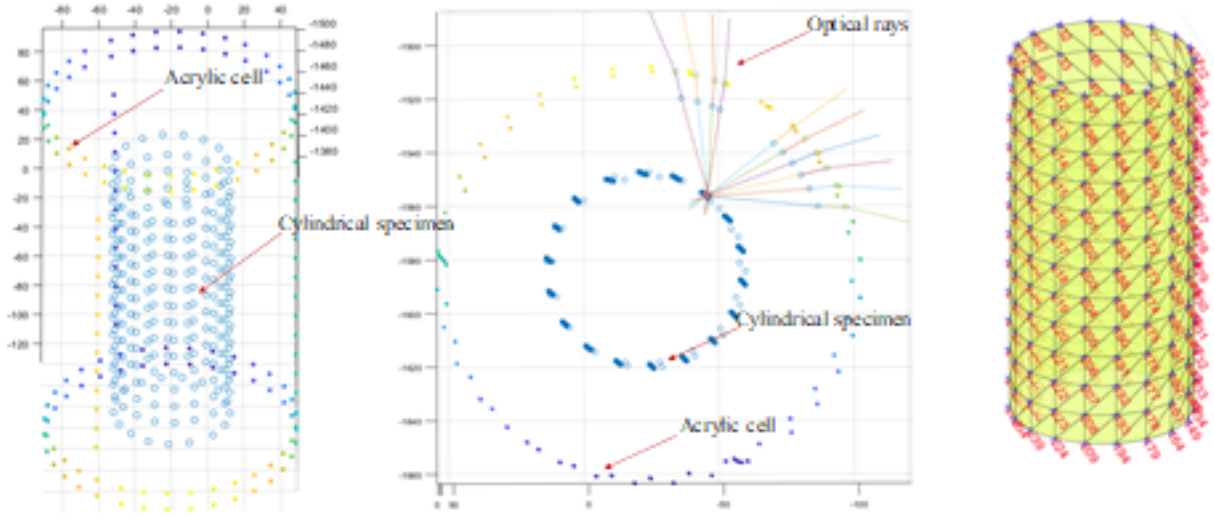

Figure 3.5 3D reconstruction results using the target recognition data: (a) 3D models of the

acrylic cell and cylindrical specimen, (b) ray tracing results, and (c) generated meshes for the 3D model of specimen.

3.2.3 3D Reconstruction Results Using the Target Recognition Data

As mentioned earlier, our objective is to reconstruct the 3D model of the triaxial sample. This paper presents a target recognition method which produces results that serve as input to 3D construction. Therefore the effectiveness and accuracy of the proposed target recognition method can also be validated by evaluating the 3D models of the cylindrical sample. Figures 3.5a and 3.5b show the 3D model of the triaxial cell as well as the cylindrical sample. Each circle on the cylindrical sample represents one target, and the 3D location of this target was determined by a multiple ray tracings technique proposed by Zhang et al (2015). Each 3D target was determined by nine optical rays on average using a least-square optimization technique. Since multiple optical rays were used to determine one point, this ensures the high accuracy of the 3D location of each target. The distance between the final points to each of the optical rays was calculated, and the average distance was 70 micron. This indicates that the target recognition method proposed in this paper is capable of producing highly accurate target location information which can be used for the accurate 3D reconstruction project. The generated mesh for the 3D model of

specimen is shown in Figure 3.5c. This mesh can be used to calculate the volume of the specimen. Detailed procedures for calculating the volume based on the generated mesh can be found in Zhang et al. (2015). Therefore, the volume-change of the specimen can be obtained.

3.3 Summary and Conclusions

This study proposed a method for target recognition using deep learning and showed that highly accurate target recognition was successfully performed. In this method, a multi-stage detection approach using faster R-CNN algorithm and transfer learning technique was proposed. The triaxial cell detection, sub-region detection, and target detection were performed consecutively. This multi-stage detection approach has proven to be five times more efficient than the template matching method. Based on the deep learning aided target recognition results, the high precision target center has been obtained by the image processing technique.

Validation of the proposed target recognition method has been performed on a triaxial cell. The proposed method attained an average precision of 0.8 for pink strip detection and an average precision of 1.0 for white strip detection. It is also verified that the proposed method is almost five faster than the template matching method in target recognition.

There are three aspects to the contributions of this study. First, this is the first study to successfully perform accurate and automated target recognition using deep learning. This study demonstrated that deep learning aided target recognition method is suitable for target recognition even with a relatively small image dataset. Second, a targets recovery algorithm has been

proposed to recognize more targets. Third, the proposed approach produces highly automated and accurate target recognition results which can be further used as input to 3D reconstruction projects for many different applications, such as volume-change measurement of unsaturated soils. Therefore, a highly efficient 3D reconstruction system can be expected using the target recognition and identification approach proposed in this study.

In order to discover more about the abilities of the proposed deep learning aided target recognition and identification approach, further research is needed. This work should aim to (1) further improve the detection efficiency using other new deep learning-based detection algorithm such as YOLO v2, (2) perform target recognition with more complicated loading scenarios and real soil samples.

CHAPTER 4 3D RECONSTRUCTION FROM MULTIPLE VIEWS

4.1 Camera Calibration with Matlab

Camera calibration in the context of 3D modelling is the process of determining the internal camera geometric and optical characteristics (intrinsic parameters) (Tsai 1987). The accuracy of camera calibration will largely influence the performance of 3D modelling.

Zhang (2000) proposed a flexible new technique for camera calibration using planar plane calibration sheet, which is perhaps the most popular camera calibration method in the computer vision community. The calibration procedures have been implemented in the Matlab toolbox based on this method. In this paper we used Single Camera Calibration App in Matlab Computer Vision System Toolbox to obtain the camera parameters, which include focal length, principal point, lens distortion coefficients and so on.

The three binders tested in this study were all used. However, the tests conducted on virgin binders were only proposed to further develop the materials library in Alaska for typical binders that can be used with RAP. The binder properties of asphalt mixtures containing RAP were not evaluated.

4.2 Determination of the Camera Positions for Unsaturated Soil Deformation Measurement

At present there is no cost-effective and efficient method to accurately measure both the global and localized deformations of unsaturated soils during triaxial tests. Recently a photogrammetry-based method has been proposed to tackle this problem. Only one camera is

required to take images of the unsaturated soil specimens from which the 3D models of the unsaturated soils can be reconstructed. This method has many advantages over existing methods including low-cost, high-accuracy and easy to use and operate. Camera position (or poses) is one of the most important parameters which can largely influence the accuracy and performance of this photogrammetry-based method. This paper presents a joint approach from both photogrammetry and computer vision to determine the camera poses from which the accurate 3D models of the unsaturated soils can be obtained. Since it makes full use of the benefits of both photogrammetry and computer vision, this joint approach has the advantages of both high-accuracy and high-efficiency. The performance of this proposed method was validated by computing the camera poses and reconstructing the 3D models of a cylinder sample.

4.2.1 Photogrammetric Approach and Its Limitation

Camera pose, also known as exterior orientation, is an essential parameter in most 3D reconstruction projects. It is one of the fundamental photogrammetric problems (Grussenmeyer and Khalil, 2002). In the following session the widely accepted methods for estimating the camera poses using photogrammetric approach will be introduced first. Then their limitations will also be discussed.

In photogrammetry the determination of the six exterior orientation parameters (X_L, Y_L, Z_L, ω, φ, κ) of a single titled photo is called space resection (Said., 2010). One widely accepted method for space resection is an iterative method based on collinearity condition. Collinearity condition states that the object point, image point and camera center lie on a straight line. Figure

4.1 shows the schematic of space resection using photogrammetry. The problem is to determine the six camera pose parameter. The following collinearity equations given by (Wolf and Dewitt, 2000) are used to solve the camera poses parameters:

$$x_a = x_o - f\left[\frac{m_{11}(X_A - X_L) + m_{12}(Y_A - Y_L) + m_{13}(Z_A - Z_L)}{m_{31}(X_A - X_L) + m_{32}(Y_A - Y_L) + m_{33}(Z_A - Z_L)}\right] \quad (1)$$

$$y_a = y_o - f\left[\frac{m_{21}(X_A - X_L) + m_{22}(Y_A - Y_L) + m_{23}(Z_A - Z_L)}{m_{31}(X_A - X_L) + m_{32}(Y_A - Y_L) + m_{33}(Z_A - Z_L)}\right] \quad (2)$$

where x_a and y_a are the image coordinates of the point a; X_A, Y_A and Z_A are 3D coordinates of object point A; X_L, Y_L and Z_L are 3D coordinates of camera locations and are the unknowns to be solved; f is the camera focal length; x_o and y_o are the coordinates of principal point; and the m's are coefficients which are functions of three rotational angles ω, φ and κ. These angles are also unknowns to be solved.

These two equations are highly non-linear and can be linearized using Taylor's theorem. The linearized form of the collinearity condition are given by:

$$b_{11}d\omega + b_{12}d\phi + b_{13}d\kappa - b_{14}dX_L - b_{15}dY_L - b_{16}dZ_L = J + v_{xa} \quad (3)$$

$$b_{21}d\omega + b_{22}d\phi + b_{23}d\kappa - b_{24}dX_L - b_{25}dY_L - b_{26}dZ_L = K + v_{ya} \quad (4)$$

where v_{xa} and v_{ya} are residual errors in measured x_a and y_a values ; $d\omega$, $d\phi$ and $d\kappa$ are corrections to the initial estimations of three angles; dX_L, dY_L and dZ_L are corrections to the initial estimations of three camera locations coordinates; J, K, b's are coefficients which are functions of the parameters mentioned above.

For one object point the above two linearized collinearity equations can be obtained. Since there are a large number of object points available, multiple linearized equations can be obtained in the same way. These linearized equations are estimations to the original collinearity equations. An iterative method is thus required to solve the unknown parameters.

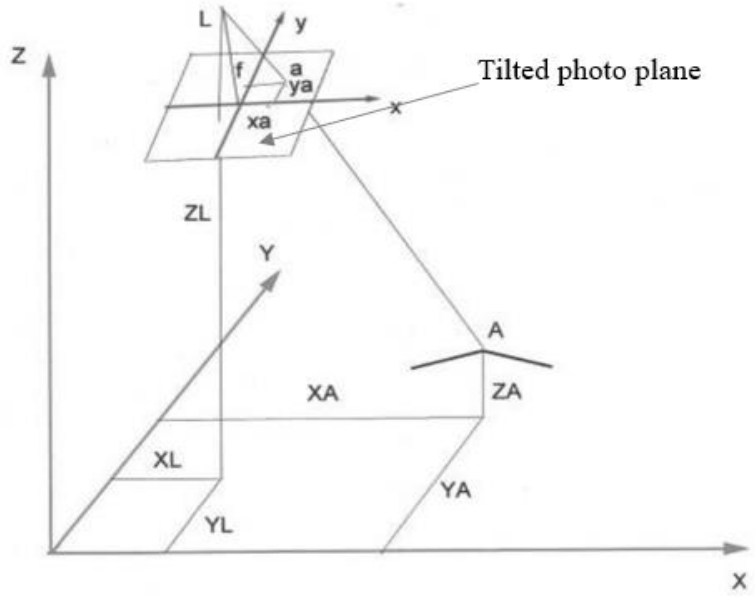

Figure 4.1: A schematic of space resection using collinearity condition (Said, 2010)

However, it has been well recognized that this iterative method requires initial estimation of the unknown parameters, which is usually difficult to obtain (Said., 2010, Wolf and Dewitt., 2000, Zeng., 2010). This is one limitation of this photogrammetric method.

4.2.2 Computer Vision Approach and Its Limitation

Exterior orientation, often called camera poses, has been discussed a lot in the computer vision community (Taketomi et al., 2014, Noll et al., 2011). While the photogrammetric approach for determination of camera poses is based on collinearity condition, the computer

vision approach to computing camera poses relies on coplanarity condition. Figure 4.2 shows the epipolar geometry. In Figure 4.2, the object point P, the optical centers of the two cameras, and the image points p_0 and p_1 all lie in the same plane. This coplanarity condition can be expressed by the following equation:

$$\overrightarrow{C_0 p_0} \cdot \left(\overrightarrow{C_0 C_1} \times \overrightarrow{C_1 p_1} \right) = 0 \tag{5}$$

Base on this coplanarity equation, the Longuet-Higgins Equation can be derived:

$$p_0^T E p_1 = 0 \tag{6}$$

where $p_0 = \begin{pmatrix} x_0 & y_0 & 1 \end{pmatrix}^T$, $p_1 = \begin{pmatrix} x_1 & y_1 & 1 \end{pmatrix}^T$ and $E = [t]_x R$,and is called essential matrix; t is the translation vector and R is the rotation matrix. If the coordinate system is constructed at the optical center of the first camera, then this translation vector t and rotation matrix define the camera poses of the second camera with respect to the first camera. Obviously, once the essential matrix E is known, the camera poses of the second camera can be determined. We have one equation for each point correspondence. Essential matrix can be calculated from a set of known point correspondence.

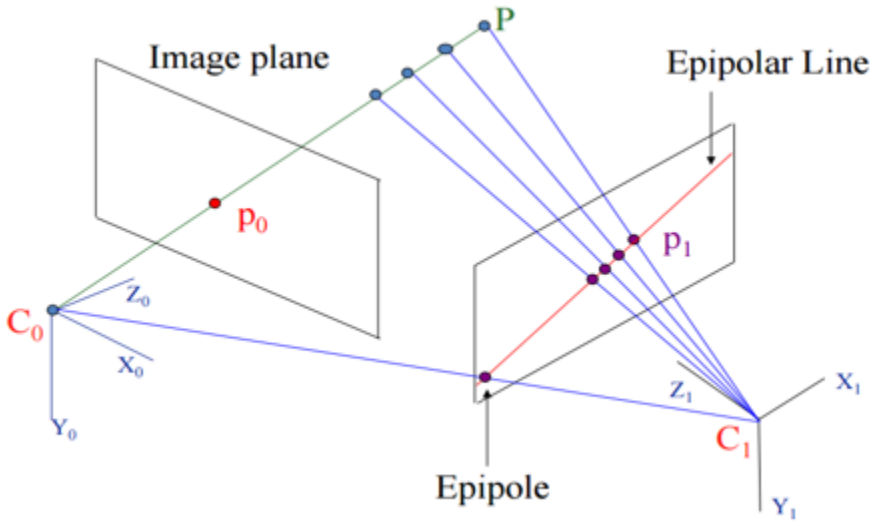

Figure 4.2 Epipolar geometry (Hoff, 2017)

Although no iterative process is required in this approach, applying this computer vision approach to measuring deformations of unsaturated soil needs to be done very carefully. This is because often the goals of computer vision are object recognition, navigation and object modeling, and the emphasis of computer vision applications is fast and time-efficient technique which sometimes sacrifices some precision for speed (Hartley and Mundy., 1993). Our goal is to develop a highly accurate method to reconstruct the 3D models of unsaturated soil samples and measure the deformations of unsaturated soils. Therefore accuracy is one concern about this computer vision approach.

4.2.3 The Proposed Approach to Determining Camera Positions

As discussed in the previous sessions, both the iterative method in photogrammetry and computer vision approach can be used to determine the camera poses. However, both methods

have limitations and cannot be directly used for accurate 3D reconstruction of unsaturated soil samples during triaxial tests. To tackle this problem, a joint photogrammetric computer vision approach is proposed. The main idea of this approach is to integrate the photogrammetric and computer vision approach to overcome their limitations.

The first step of this approach is camera calibration. The purpose of camera calibration is to correct image distortions as well as to obtain the camera intrinsic parameters such as focal length, principal point, and format size. These are also important parameters that could largely influence the accuracy and performance of 3D reconstruction. Zhang (2000) proposed a flexible camera calibration method which has been commonly used in computer vision. Based on this method, recently a Matlab Single Camera Calibtation App has been developed by the MathWorks, Inc. This app is simple and easy to use and is adopted in this approach. The second step is to use the computer vision approach to computing the camera poses of the first views (photo). An assumption is made here that the coordinates system is constructed at the optical center of the first camera. Then the camera pose of the second camera can determined using the computer vision approach discussed in the last section. Obviously this camera pose is a rough result but is still accurate enough to serve as the initial estimation to the camera pose of the next view (the 3rd view) since the second view and the 3rd view are very close. The third step is to use the results from the first view as described in step 2 to perform space resection, and in this stage the photogrammetric approach will be applied. The camera poses for the third view will be calculated in an iterative way until the small tolerant correction is satisfied. The flowchart of the

iterative process is shown in Figure 4.3. The fourth step follows the same procedure, using the camera poses of the third view obtained in step 3 as the initial guess of camera poses of the fourth view. The iterative method is applied again to determine the accurate camera poses for the fourth view; step 5 repeats this procedure until all the views (photos) are processed. Once processing completes, the camera poses for all the photos can be determined.

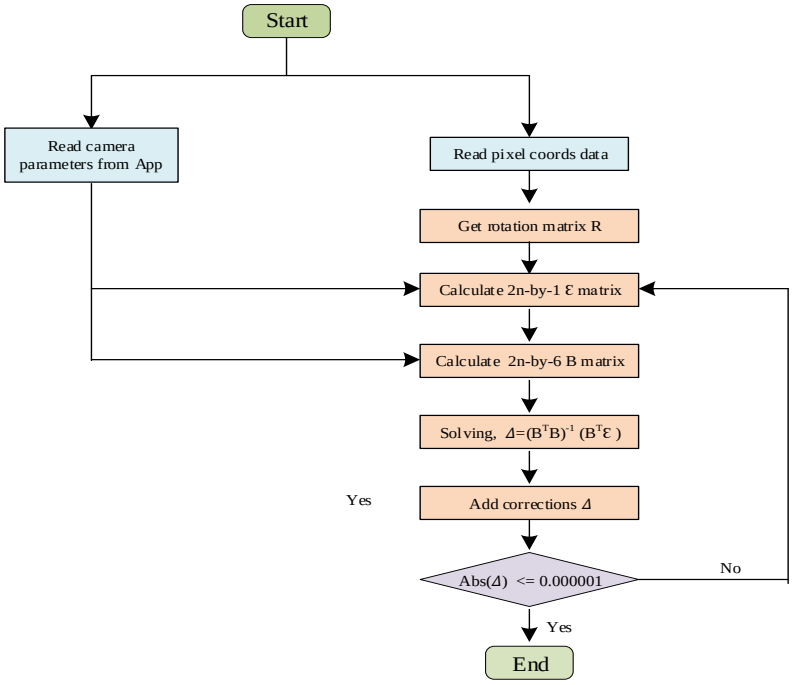

Figure 4.3 Flowchart of the photo resection method

Table 4.1 Camera parameters obtained by Matlab App

Focal length		Principal point		Radial distortion		Tangential distortion	
X (pixel)	Y (pixel)	X (pixel)	Y(pixel)	K_1	K_2	P_1	P_2
11557.6	11537.3	2580.3	1596.2	-0.542	19.7842	0.0030	-0.0021

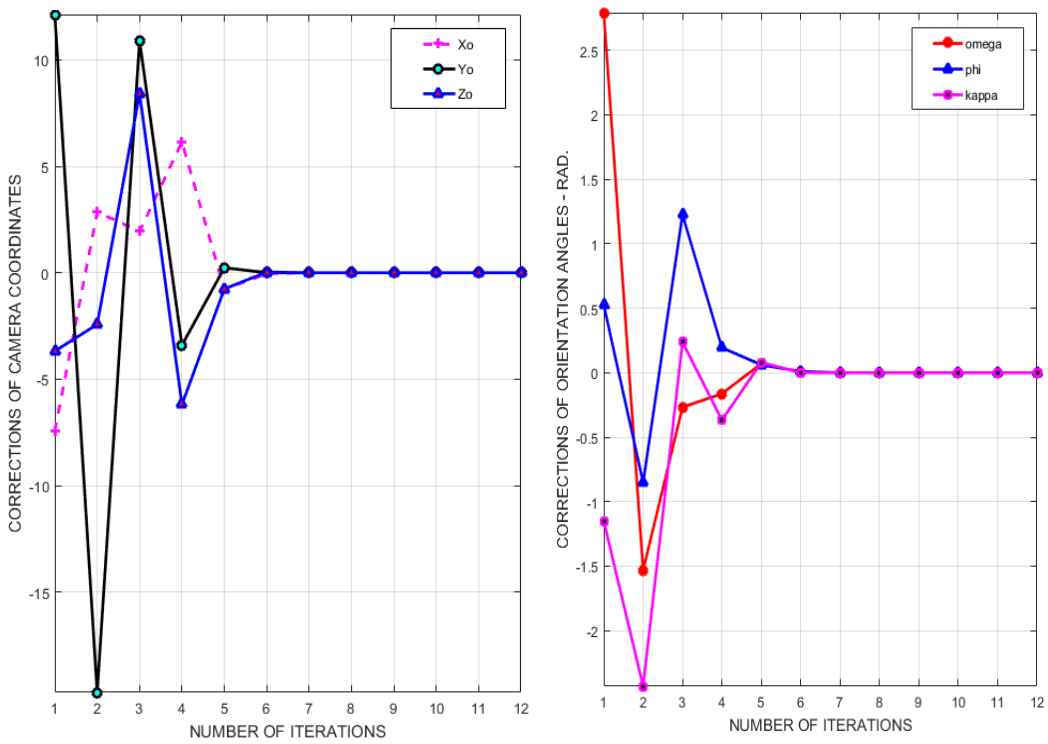

(a) (b)

Figure 4.4 Least square adjustment for (a) camera coordinates; (b) orientation angles

4.3 3D Reconstruction from Multiple Views Workflow

4.3.1 Point Matching between Two Neighboring Views

The coded target detection and camera calibration results described in the previous sections serve as inputs to the 3D modelling from multiple views. An input file stores the information regarding the coded target ID, photo ID and pixel coordinates for each coded target in each image. Since 3D modelling from multiple views requires the overlapping interest points (coded targets) between each two neighbouring views, the overlapping interest points for each two neighbouring views are matched first based on their coded target IDs and photo IDs. These matched points are then stored and will be used in the following procedures.

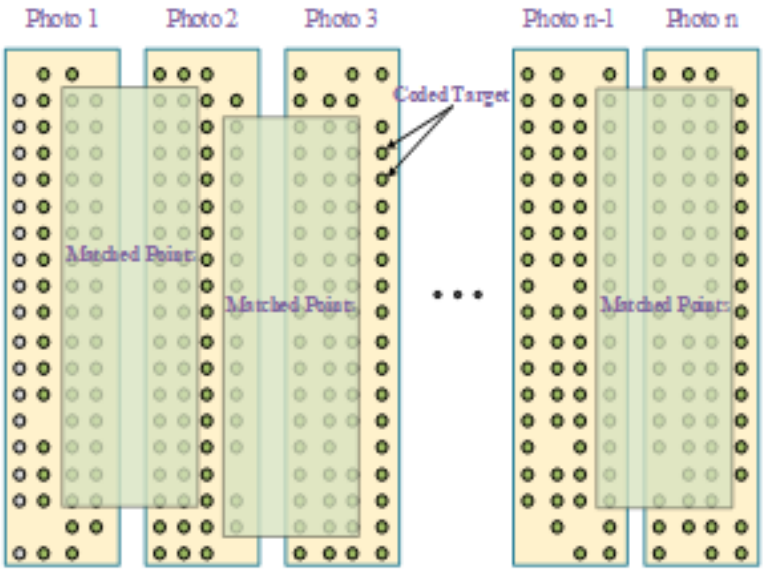

Figure 4.5 Point matching for the coded targets between each two neighbouring views

4.3.2 3D Reconstruction from the First Two Views

As mentioned earlier, the 3D reconstruction from the first two views (photos) was performed using the computer vision approach. In this approach, the coplanarity condition was used and given by:

$$\overrightarrow{C_0p_0} \times (\overrightarrow{C_0C_1} \times \overrightarrow{C_1p_1}) = 0 \qquad (1)$$

where C_0 and C_1 are camera positions of the left and right cameras, respectively and p_0 and p_1 are the image points in the left and right images, respectively.

Another important equation involved in this approach is Longuet-Higgins equation, which is given by:

$$p_0^{T} E\, p_1 = 0 \qquad (2)$$

where E is essential matrix which contains information regarding camera positions. The essential matrix has five degrees of freedom. Therefore, if there are five pairs of known image points in the left and right images, five equations can be obtained to solve the essential matrix. Then, by decomposing the essential matrix, the camera positions can be determined.

After the camera positions were obtained, the photo intersection can be performed. Photo intersection is the process of using camera positions and pixel coordinates information of the targets to find the 3D coordinates of the object points in space. Therefore, the 3D models of the triaxial cell from the first two images can be obtained.

4.3.3 3D Reconstruction from the Rest of Views

A photogrammetric approach called photo resection was utilized to calculate the camera positions for the rest of views. Photo resection is a terminology in photogrammetry for the recovery of camera position parameters. The principle of photo resection is based on the collinearity condition in which the three points, namely the object point, the images point, and the optical center of the camera, lie on the same line. One then has the linearity equations. The iterative method can be used to solve these highly non-linear equations to obtain the camera positions.

One limitation of the photo resection method is that at least three control points are required. In many cases, however, it is difficult to obtain the control points with known 3D coordinates. To address this limitation, the 3D reconstruction results from the first two views were used. Ten to fifteen points with known 3D coordinates obtained from 3D reconstruction of

the first two views were selected as control points. Therefore, the joint approach from computer vision and photogrammetry proposed in this paper is capable of overcoming the limitations of conventional 3D reconstruction methods.

The next step is similar to the 3D reconstruction from the first two views. The photo resection process will be performed to determine the 3D coordinates of points (CTs) on the triaxial cell and frame rods. A typical 3D reconstruction result for the rest of views was shown in Figure 4.6. In the figure, both the points on the triaxial cell and frame rods, and the camera positions were presented.

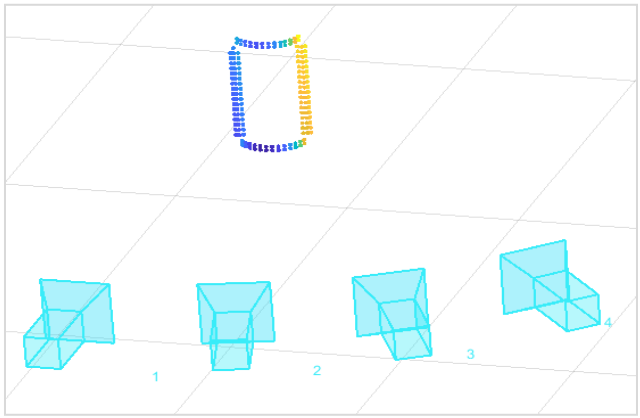

Figure 4.6 3D reconstruction results for the first four views.

4.3.4 3D Bundle Adjustment

Bundle adjustment refines a visual reconstruction system so that the 3D structure and viewing parameter (camera poses and/or calibration) estimates are optimal (Triggs et al.2011). Bundle adjustment is an essential step in achieving highly accurate 3D reconstruction results since many parameters, such as camera positions and 3D coordinates of the points, are optimized

simultaneously. This process is usually performed after photo intersection. For the rest of views, bundle adjustment will be performed to produce a high-accuracy 3D reconstruction project. After all the images are processed, the 3D model of the triaxial cell can be obtained.

4.4 Ray Tracing for Refraction Correction

The 3D reconstruction of triaxial cell in the air was presented in the last section. Our purpose is to reconstruct the 3D models of the soil sample which is more challenging due to refraction. Existing 3D reconstruction methods cannot be applied because refraction occurs at the interfaces between different optical media and the pinhole model cannot be used. In our case, there is refraction at the air-acrylic cell interface and acrylic cell-water interface (as shown in Figure 4.7b).

To address this challenge, a multiple ray tracing technique based on Snell's law was developed by Zhang et al., 2015 to correct the refraction. To apply the ray tracing technique, the geometric shape of the triaxial cell is required. Therefore the determination of the shape and location of the triaxial cell is introduced first in this section. Then the ray tracing process is discussed. Finally based on multiple the ray tracing results, a least square optimization method is used to determine the 3D coordinates of points on the soil specimens and the 3D model of soil specimen as well. Many of the concepts will only be briefly discussed here while a more detailed description can be found in Zhang et al., 2015.

4.4.1 Determination of the Shape and Position of the Confining Chamber

It was found that the confining chamber (triaxial cell) expanded to a barrel shape after vertical load and applied water pressure (Zhang et al., 2015). Consequently, a quadratic equation that describes the deformed shape of the confining chamber was given as follows:

$$X'^2 + Z'^2 = AY'^2 + BY' + C \qquad (3)$$

or in a matrix form:

$$[X' \quad Y' \quad Z'] \begin{bmatrix} 1 & 0 & 0 \\ 0 & -A & 0 \\ 0 & 0 & 1 \end{bmatrix} \begin{bmatrix} X' \\ Y' \\ Z' \end{bmatrix} - [X' \quad Y' \quad Z'] \begin{bmatrix} 0 \\ B \\ 0 \end{bmatrix} - C = 0 \qquad (4)$$

where X', Y', and Z' are coordinates of the points on the surface of triaxial cell in the local coordinate system. The center of the triaxial cell is set as the origin of the local coordinate system. X', Y', and Z' can be expressed by the 3D coordinates of points on the triaxial cell X, Y, Z, and the positions of the triaxial cell, including locations X_R, Y_R, Z_R, and rotation angles ω', ϕ', κ'. The 3D coordinates of points on the triaxial cell obtained in the last section can be used to best-fit the geometric shape of the deformed triaxial cell. A least square optimization method was used to determine the nine parameters (A, B, C, X_R, Y_R, Z_R, ω', ϕ', κ') regarding the geometric shape of the triaxial cell.

4.4.2 Ray Tracing Process

An optical ray-tracing technique is proposed to take into account the refraction effect. It is well known that the refraction of an optical ray at the interface of different optical media follows Snell's law:

$$n_1 \sin\theta_1 = n_2 \sin\theta_2 \qquad (5)$$

where n_1 and n_2 are refractive indices, and θ_1, θ_2 are incident and refraction angles.

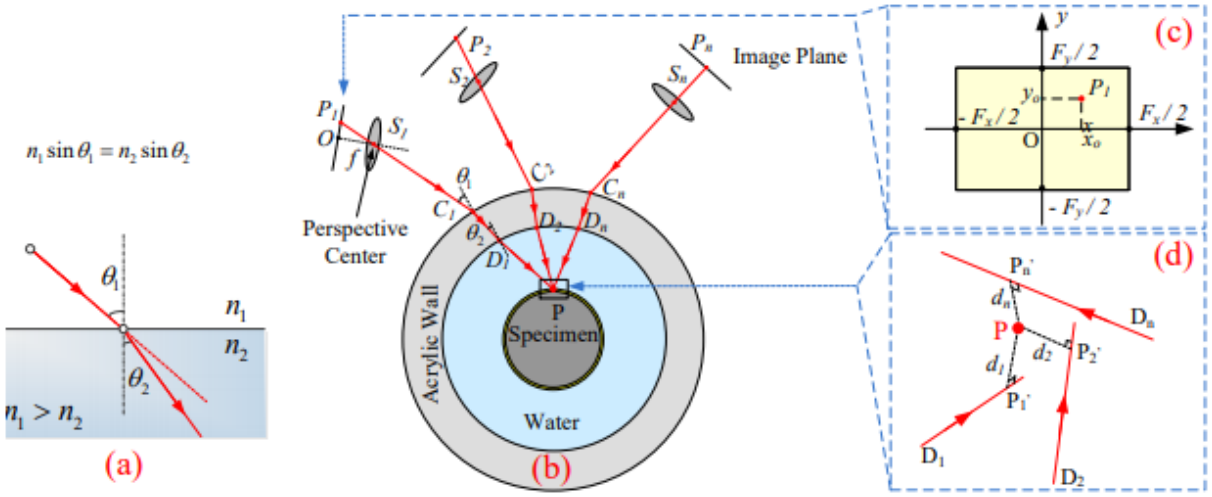

Figure 4.7 Refraction correction based on Snell's law.

Refraction between two surfaces is reversible; that is, if all conditions were identical, the angles would be the same for light propagating in the opposite direction. It is the theoretic basis for the optical ray-tracing technique (see Figure 4.7b). As shown in Figure 4.7b, the perspective center S_1 and shooting direction OS_1 for photograph 1 can be accurately found using photogrammetry, described in section 4.3.3. The coordinate of the point of interest on the image plane P_1 can be translated to the global coordinate based on the camera parameters such as the focus length f and principal point value of the image center O (Px and Py in Figure 4.7c). The direction vector of the ray P_1S_1 can also be obtained. Since the shape and location of the acrylic chamber are known in the global coordinate system through photogrammetry using the measurement targets posted on the acrylic chamber surface, the intersection point between the

ray P_1S_1 and the outside surface of the acrylic chamber (C_1 in Figure 4.7b) can therefore be solved. By finding the normal of the acrylic chamber at point C_1, the incident angle θ1 of the ray at point C_1 can be found. By applying Snell's law, the direction vector C_1D_1 can be obtained. Since the acrylic confining chamber is thin, the change in wall thickness under pressure is negligible. The inner surface of the confining chamber can therefore be calculated from the outside surface. With a known inner surface and the direction vector C_1D_1, the coordinate of their intersection, point D_1, can be solved. By applying Snell's law a second time, the direction vector D_1P can be solved (note that the coordinate of point P is still unknown at this time). This process is called optical ray tracing. The same optical ray-tracing process can be applied to photographs 2 to n in Figure 4.7b using the corresponding points P_2 through Pn and the coordinates of D_2 through D_n and direction vector D_2P through D_nP can be found. If there is no error, D_1P, D_2P…, and D_nP will all meet at the point P. By solving the intersection of any two rays among D_1P, D_2P, and D_nP, the coordinate at P is obtained.

4.4.3 Least Square Optimization for 3D Coordinates of Points on the Soil Specimens

Snell's law is a theoretical equation and gives the analytic solution as long as all inputs are accurate. Although the photogrammetric method is highly accurate, some errors are still expected in the obtained camera orientations and acrylic chamber positions. Consequently, it is very likely that D_1P, D_2P, and D_nP do not intersect at a common point P, as shown in Figure 4.7b. Instead they might be rays D1P1', D2P2', and D_nP_n' in the 3D space with no intersection, as shown in Figure 4.7d. To overcome this limitation, a least square optimization approach is

used to best approach the real coordinate of point P by finding a combination of the coordinates (x, y, z) that minimizes the sum of the square of the distances from the point to the optical rays, that is, to find a point with the coordinate (x, y, z), which minimizes $\sum_{i=1}^{n} d_i^2$ where d1, d2, and dn are the distance from P to the optical rays D_1P_1', D_2P_2', and D_nP_n' in Figure 4.7d. At least three photographs (measurements) are needed to perform the search. The more photographs used, the higher the accuracy. Photographs are also captured from orientations, which can provide the best quality and accuracy. Using this approach, no assumptions about the initial shape, position, and deformation patterns of the specimen are needed.

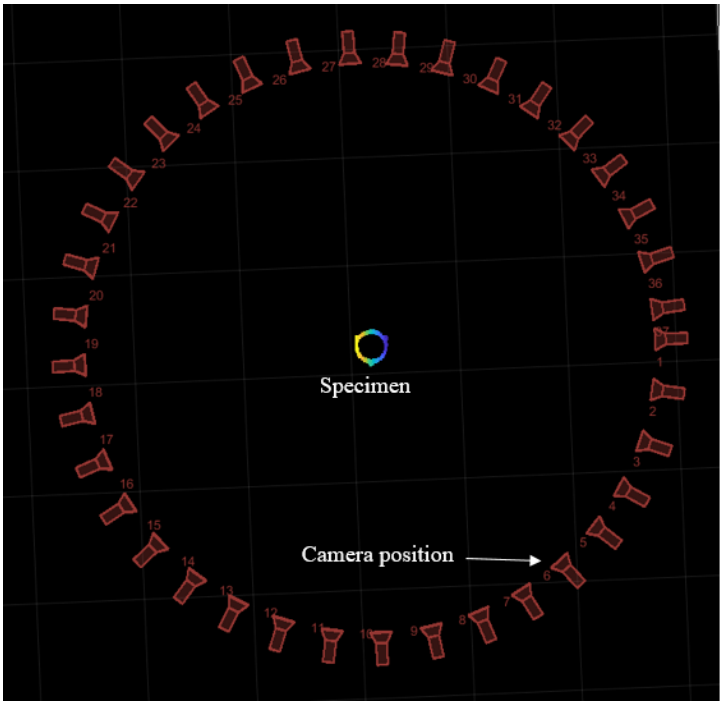

(a)

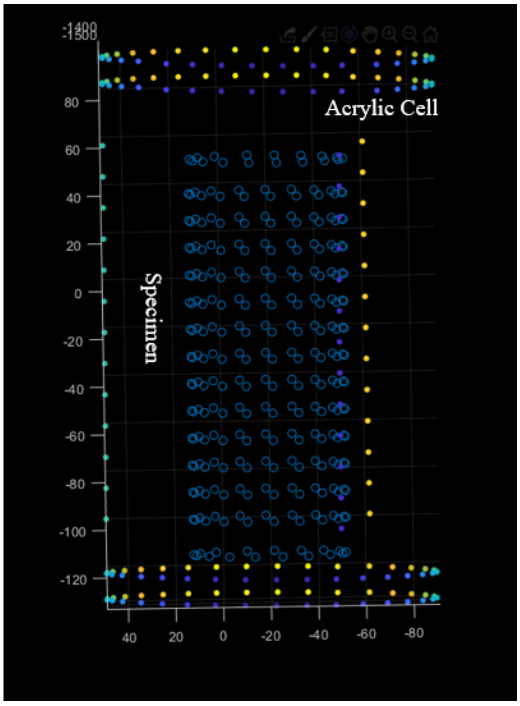

(b)

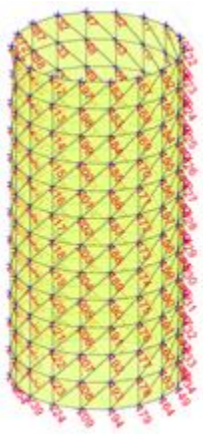

(c)

Figure 4.8 3D reconstruction and ray tracing results.

Figure 4.8 shows the 3D reconstruction and ray tracing results obtained by the proposed method. In Figure 4.8a, the three-dimensional model of a cylindrical specimen was reconstructed and the camera positions were accurately determined. The camera positions were obtained by the proposed photogrammetric computer vision approach as described in section 4.3 while the three-dimensional model of the specimen was determined by the ray tracing technique as previously discussed in section 4.4. By constructing a global coordinate system in which the origin is at the optical center of the first camera position, the three dimensional coordinates of the coded targets on the specimen and the acrylic cell were determined. Figure 4.8b provides a better visualization of the three-dimensional models of the specimen as well as the acrylic cell. Based on the point cloud of the cylindrical specimen shown in Figure 4.8b, mesh was generated for volume calculation as shown in Figure 4.8c.

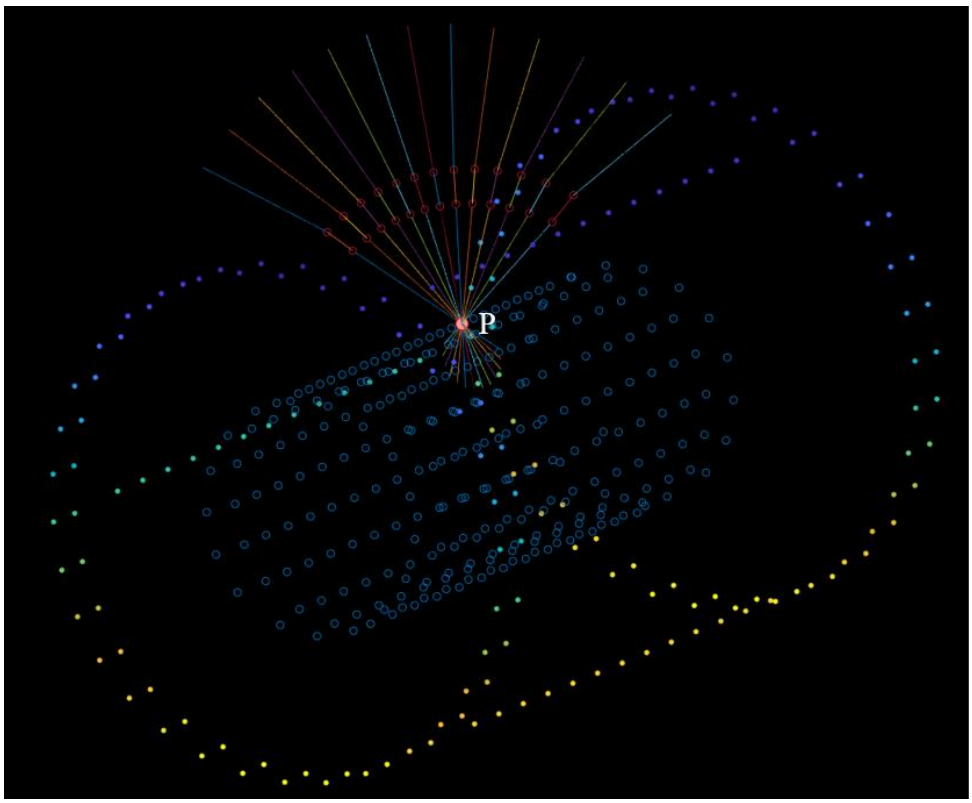

Figure 4.9 Ray tracing results with multiple rays.

Figure 4.9 shows the process of ray tracing with thirteen optical rays. Note that these thirteen rays were all used to determine the three-dimensional coordinates of one single point P on the specimen as denoted by the pink circle in the figure. The path of each optical ray was recovered and presented in the figure. For each optical ray, it first traveled in the air and intersected with the acrylic cell. Then refraction occurred at the air-acrylic cell interface and the first refractive ray went through the acrylic cell. As can be seen in the figure, the rays came from different angles, and the corresponding refraction angles were also different. The optical rays with larger incident angles had larger refractive angles. This is consistent with the Snell's law. The optical ray then intersected with the inner wall of the acrylic cell and the second refraction

occurred. Finally, the optical ray that experienced two refractions traveled towards point P. While with a large range of incident angles, the thirteen optical rays finally travelled toward one single point P. Then the final 3D coordinates of P were determined using the least square optimization technique as discussed previously.

In some cases, one or several optical rays have larger errors, which are called outliers, and can influence the accuracy of determining the 3D coordinates of the points on the specimen. These outliers often have a larger distance from the final 3D point P to the outliers themselves. Therefore, they need to be removed to achieve more accurate results. An automated program was developed to automatically delete the outliers. Figure 4.10 shows enlarged views of the optical rays before and after removal of the outliers. As can be seen in Figure 4.10a, the red line has larger distance from the determined 3D point to the line itself. This line was then removed, and the updated result was shown in Figure 4.10b. This automatic detection and removal of outlier rays can greatly improve the accuracy of the 3D reconstruction of specimen with consideration of refraction.

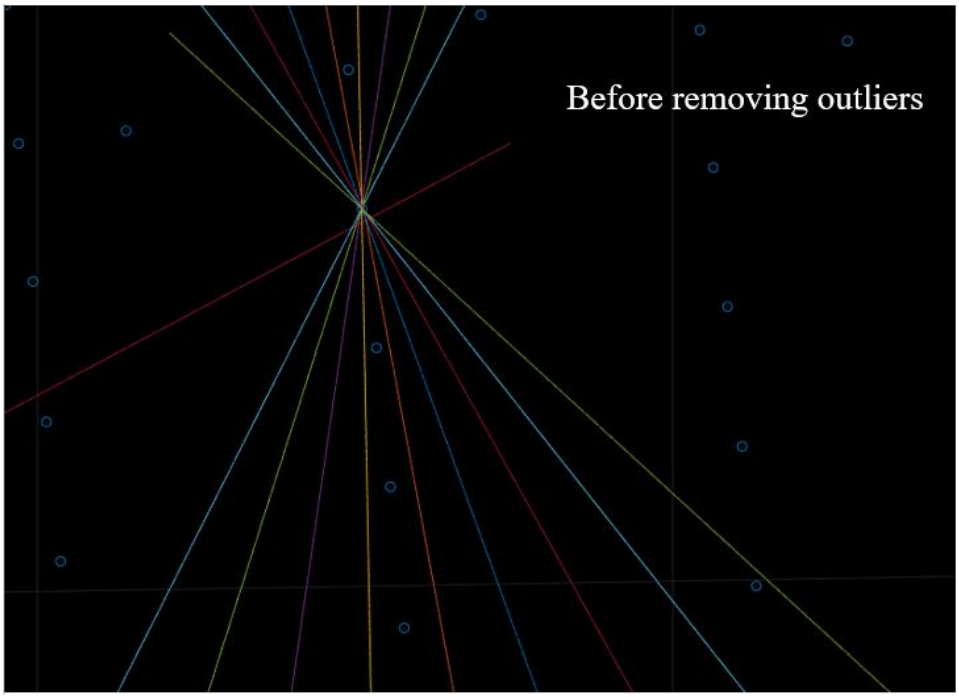

(a)

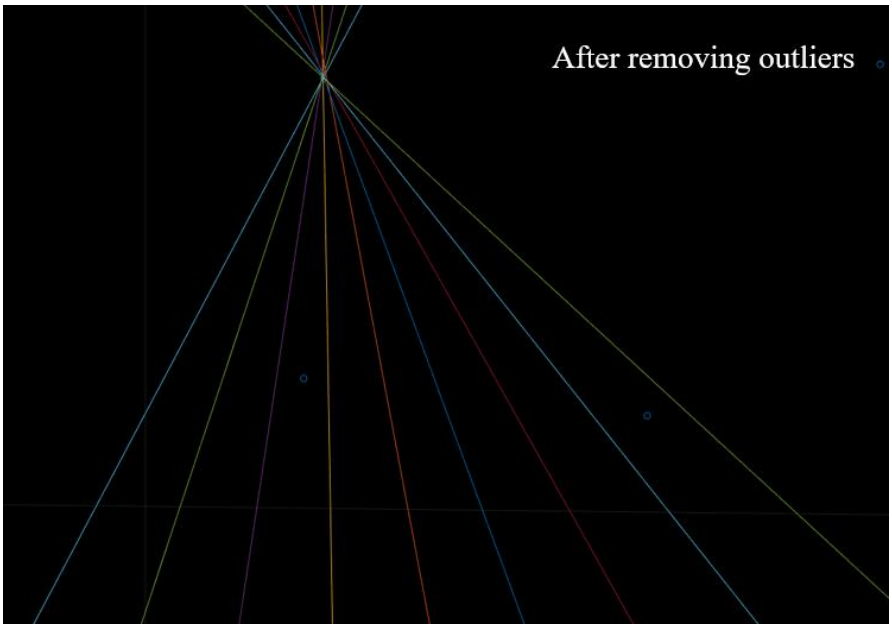

(b)

Figure 4.10 Removal of outliers during ray tracing

CHAPTER 5 APPLICATION IN GEOSYNTHETIC TESTS

Conventional methods for measuring the deformational response of geosynthetics, such as LVDT, strain gauges, and extensometers have several limitations in fully determining the complete strain distribution in geosynthetics. Recently, an image-based method which has many advantages over existing methods has been proposed to measure the deformational properties of geosynthetics. However, this method requires accurate manual control of the camera position and assumes that the geosynthetics remain planar during the whole testing process. Both of the requirements cannot be satisfied for several reasons, which can lead to misleading results. To overcome the limitations of existing methods, this paper presents a multi-camera-based photogrammetric method which can accurately measure the 3D full-field displacements of geosynthetics during tensile tests. A tensile test on a geogrid specimen was performed to verify the effectiveness and accuracy of the proposed photogrammetric method. The proposed method is non-contact, cost-effective, highly accurate, and capable of measuring 3D deformation of geosynthetics and identifying the localized strain. It is shown that the average absolute difference in displacement obtained by the machine and the proposed photogrammetric method is 0.25%, and the average absolute error is 0.038 mm. 3D deformation analysis shows that the R-squared of fitting planes of the geogrids is initially 97.2%, and can decrease to 95.2% during the tensile tests, which indicates that the geogrids are not initially planar and can undergo large out-of-plane deformations during the tensile tests. The proposed photogrammetric method also demonstrates that the manual control of camera positions and shooting direction is impossible, and the proposed method does not require the camera positions and shooting direction to be controlled.

5.1 Theoretical Basis of the Proposed Method

The proposed method is based on the principles of photogrammetry. Photogrammetry is defined as the science and technology of obtaining reliable information about physical objects through processes of recording, measuring, and interpreting photographic images and has been widely used for 3D reconstruction and deformation measurements in multiple fields, such as surveying, geology and mining, agriculture, architecture, and civil engineering. (Wolf and Dewitt, 2004; Zhang et al., 2015; Lin and Zhang, 2016).

Since photogrammetry is a well-established tool that has been in use for a long period of time, the principle of photogrammetry is only briefly introduced here. The fundamental principle of photogrammetry is triangulation. Triangulation determines the precise three-dimensional coordinates of the points of interest by mathematically intersecting multiple converging rays. Another important step in photogrammetry is bundle adjustment. Bundle adjustment is refining the 3D reconstruction by jointly optimizing the 3D coordinates of points of interest and viewing parameter (camera positions and/or calibration) estimates. By performing bundle adjustment, all the related parameters, for example, 3D coordinates and camera positions are optimized simultaneously. This enables photogrammetry to achieve very good accuracy. Zhang et al. (2015) did validation tests and reported that the accuracy of photogrammetry is 2-5 μm.

Based on photogrammetry, a multi-camera based photogrammetric method, also known as a mid-point method, has been developed. In the next section, the principle of the proposed multi-camera based method will be explained in detail.

5.1.1 A Mid-Point Method for Geogrids Deformation Tracking Using Two Cameras

One problem in using photogrammetry is that the measured objects photogrammetry projects deal with are often stationary. In this case, we only need one moving camera to take

multiple images of the scene and can obtain expected results. However, conventional photogrammetry cannot be used for dynamic tests with continuous measurements of displacement. For many cases, the measured objects are moving. In our case, the geogrid specimens will undergo continuous deformation and are no longer stationary. There are generally two solutions to this problem. The first one is to use multiple cameras to capture images simultaneously during the tests. This method requires a lot of cameras which is not cost-effective. In addition, too many cameras make the measuring system much more complex and difficult to operate. The second solution is to use only two cameras since triangulation requires at least two converging rays. This method seems more cost-effective and simpler. However, to the authors' knowledge, no related work using such a method has been reported, and the effectiveness and accuracy of this method also needs to be validated. In the following section, the detailed mathematical descriptions of this method, which is also called mid-point method, will be presented, and the validation results of this method will be presented and discussed in section 5.3.3 and 5.3.4.

Here we assume that the camera positions and orientation are known. The method for determining camera positions and orientation was described in section 4.3.3 and commercial photogrammetric software, such as PhotoModeler, PhotoScan, are available to obtain these camera position parameters. The procedures for deriving the mathematical description of the two image rays are very similar to the one adopted by Zhang et al. (2015). Many concepts will consequently be briefly recalled here while a more detailed description can be found in Zhang et al. (2015). Assume image point I is one of the points of interest in the images. The coordinates of point I in the pixel coordinate system are m_I, n_I. The physical coordinates of point I can be expressed as:

$$\begin{bmatrix} x_I^{'} \\ y_I^{'} \end{bmatrix} = \begin{bmatrix} F_x / M & 0 \\ 0 & F_y / N \end{bmatrix} \begin{bmatrix} m_I \\ n_I \end{bmatrix} \tag{1}$$

where $x_I^{'}, y_I^{'}$ are physical coordinates of point I(mm), F_x, F_y are format size of the image sensors in the x and y directions, respectively (mm), M, N are total numbers of pixels in x and y directions, respectively (mm).

These two-dimensional physical coordinates are then converted to three-dimensional coordinates in the local coordinate system, which can be calculated as follows:

$$\begin{bmatrix} x_I \\ y_I \\ z_I \end{bmatrix} = \begin{bmatrix} x_I^{'} - P_x \\ -y_I^{'} + P_y \\ -f \end{bmatrix} \tag{2}$$

where $x_I, y_{I,} z_I$ are coordinates of point I in the local coordinate system (mm), P_x, P_y are principal point of the camera (mm), which can be obtained by camera calibration. f is the focal length of the camera after camera calibration (mm). The coordinates of point I in the global coordinate system are calculated as follows:

$$\begin{bmatrix} X_I \\ Y_I \\ Z_I \end{bmatrix} = R(\omega, \varphi, \kappa) \begin{bmatrix} x_I \\ y_I \\ z_I \end{bmatrix} + \begin{bmatrix} X_S \\ Y_S \\ Z_S \end{bmatrix} \tag{3}$$

where $X_I, Y_{I,} Z_I$ are coordinates of point I in the global coordinate system (mm), $X_S, Y_{S,} Z_S$ are the camera locations, ω, φ, κ are the camera orientation, and R is the rotation matrix.

Combining equations (1), (2), and (3) yields

$$\begin{pmatrix} X_I \\ Y_I \\ Z_I \end{pmatrix} = R(\omega,\phi,\kappa)\begin{pmatrix} x_I \\ y_I \\ z_I \end{pmatrix} + \begin{pmatrix} X_S \\ Y_S \\ Z_S \end{pmatrix} = R(\omega,\phi,\kappa)\begin{bmatrix} \frac{F_x}{M} & 0 & -p_x \\ 0 & -\frac{F_y}{N} & p_y \\ 0 & 0 & -f \end{bmatrix}\begin{bmatrix} m_I \\ n_I \\ 1 \end{bmatrix} + \begin{pmatrix} X_S \\ Y_S \\ Z_S \end{pmatrix} \quad (4)$$

Let $\begin{bmatrix} \frac{F_x}{M} & 0 & -p_x \\ 0 & -\frac{F_y}{N} & p_y \\ 0 & 0 & -f \end{bmatrix}$ be M, and $\begin{bmatrix} m_I \\ n_I \\ 1 \end{bmatrix}$ be P . The mathematic description of the image ray corresponding to point I from the first camera is given by:

$$\overrightarrow{SI} = \begin{pmatrix} X_I \\ Y_I \\ Z_I \end{pmatrix} - \begin{pmatrix} X_s \\ Y_s \\ Z_s \end{pmatrix} = R \cdot M \cdot P + \begin{pmatrix} X_s \\ Y_s \\ Z_s \end{pmatrix} - \begin{pmatrix} X_s \\ Y_s \\ Z_s \end{pmatrix} = R \cdot M \cdot P \quad (5)$$

Point I also appears in the second image which was taken by the second camera. Similarly, we can obtain the equation for the second optical ray from the second camera as follows:

$$\overrightarrow{S_1 I_1} = R_1 \cdot M_1 \cdot P_1 \quad (6)$$

Based on the mathematic description of the two image rays discussed in the last section, the two straight lines that pass these two image rays can be expressed as two three-dimensional vectors as follows:

$$\text{Line 1: } L_1 = C_1 + t_1 \overrightarrow{SI} \quad (7)$$

$$\text{Line 2: } L_2 = C_2 + t_2 \overrightarrow{S_1 I_1} \quad (8)$$

where C_1 and C_2 are the three-dimensional coordinates of the perspective centers of the two cameras, which are also the camera positions that determined in step 2.2.1. $\overrightarrow{SI}$ and $\overrightarrow{S_1I_1}$ are the two optical rays obtained in step 2.2.1.

In the ideal case of no error, these two lines should converge to the same point P. Unfortunately, measurement error and computation error are unavoidable and these two lines are skew lines in 3D space, so they will not intersect (as shown in Figure 5.1). To solve this problem a midpoint method is proposed to find the 3D coordinates of the point of interest. In this method, we assume that the midpoint of the shortest line segment joining the two lines is the point in 3D space which can minimize the distance from this point to the two lines. The 3D coordinates of this point are also the closest to the "true" location of point P.

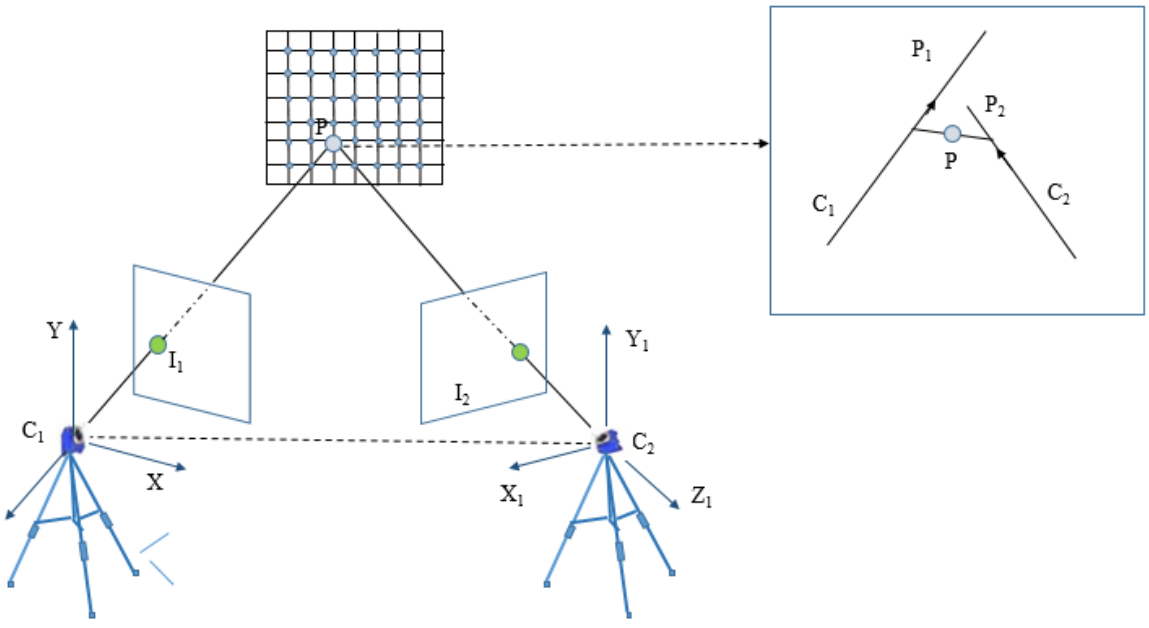

Figure 5.1 Principles of the mid-point method

The cross product of $\overrightarrow{SI}$ and $\overrightarrow{S_1I_1}$ is perpendicular to the two lines, and can be calculated as:

$$\vec{n} = \overrightarrow{SI} \times \overrightarrow{S_1 I_1} \tag{9}$$

The plane formed by the translation of line 1 along $\vec{n}$ contains the point p_1 and is perpendicular to

$$\overrightarrow{n_1} = \overrightarrow{SI} \times \vec{n} \tag{10}$$

The plane formed by the translation of line 2 along $\vec{n}$ contains the point p_2 and is perpendicular to

$$\overrightarrow{n_2} = \overrightarrow{S_1 I_1} \times \vec{n} \tag{11}$$

The intersecting point of line 1 with the above-mentioned plane is given by

$$p_1 = C_1 + \frac{(C_2 - C_1) \cdot \overrightarrow{n_2}}{\overrightarrow{SI} \cdot \overrightarrow{n_2}} \overrightarrow{SI} \tag{12}$$

Similarly, the intersecting point of line 2 is given by

$$p_2 = C_2 + \frac{(C_1 - C_2) \cdot \overrightarrow{n_1}}{\overrightarrow{S_1 I_1} \cdot \overrightarrow{n_1}} \overrightarrow{S_1 I_1} \tag{13}$$

Thus, the midpoint of the segment formed by intersecting point 1 and intersecting point 2 is given by

$$p = \frac{C_1 + C_2 \frac{(C_2 - C_1) \cdot \overrightarrow{n_2}}{\overrightarrow{SI} \cdot \overrightarrow{n_2}} \overrightarrow{SI} + \frac{(C_1 - C_2) \cdot \overrightarrow{n_1}}{\overrightarrow{S_1 I_1} \cdot \overrightarrow{n_1}} \overrightarrow{S_1 I_1}}{2} \tag{14}$$

5.2 Experimental Design

5.2.1 Specimen Preparation and Test Method

Biaxial geogrids (BasXgrid 11) produced by TenCate company were used as a representative geosynthetics to demonstrate the effectiveness and accuracy of the proposed method. The same method can be easily applied to a wide range of other geosynthetics such as

geotextile, geomembrane, and even geocells. Geogrids are commonly used in geotechnical projects and BasXgrid 11 has many unique properties which makes it ideal for base course reinforcement.

Table 5.1. Properties of the geogrid tested

Material	Mass per unit area (g/m^2)	Aperture size (mm)	Tensile modulus (at 1% strain)	Wide width tensile strength (kN/m)			
				At 1% strain	At 2% strain	At 5% strain	At ultimate
Polyester	405	25.4	437	4.3	7.3	13.4	29.2

The material properties of the geogrids used in the tests are listed in Table 5.1. The dimensions of each specimen were approximately 25 cm in width and 35 cm in length. These dimensions were selected in accordance with ASTM D6637/D6637M-15 (2015). In order to employ the photogrammetric method to obtain the full field displacements of geogrid, marked coded targets were placed within the whole geogrid sample. A typical image of the specimen with marked coded targets placed on it is shown in Figure. 5.2a.

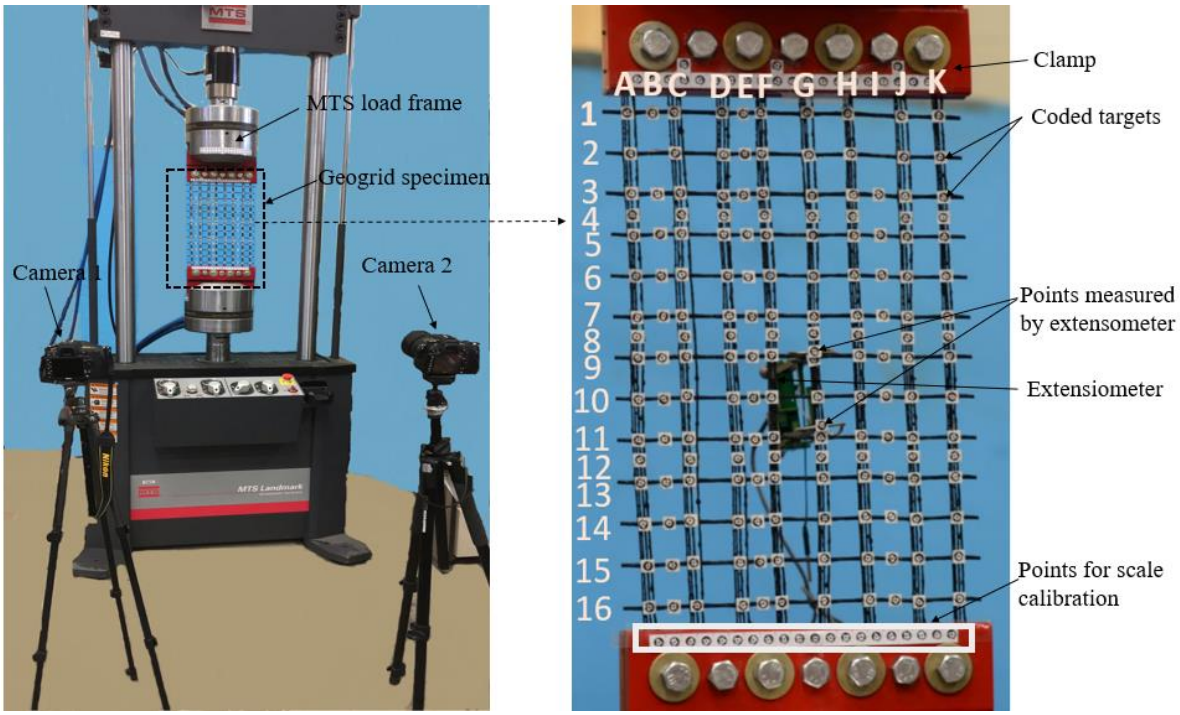

a) b)

Figure 5.2 Geogrid tensile test setup and geogrid specimen: a) geogrid tensile test setup for deformation analysis using photogrammetric method and conventional methods; and b) geogrid specimen with coded targets placed on it.

An MTS Landmark 370 load frame equipped with a 250kN load frame rated capacity was used for testing the geogrid specimens. The selected displacement rate was 2.54 mm/min. Self-designed clamps were used to fix the top and bottom edges of the specimens to the machine. In order to compare the accuracies of the proposed method with conventional methods, an extensometer was mounted at the middle of the back of the specimen, and two coded targets were placed on the extensometer. The displacements of these two points will be measured by both the extensometer and the proposed photogrammetric method so that the results from the two methods can be compared. It is noted that the machine itself also measured and recorded the specimen deformation data, which will be compared with our proposed method.

5.2.2 Image Acquisition

To acquire the required images, two commercial Nikon digital cameras were used. The optical properties of the cameras are listed in Table 5.2. First, each camera was used to take 10 images in any arbitrary orientations and locations. This allows for many flexibilities of image capturing. After all the 10 images were taken, the camera was fixed on a tripod. The position of the camera fixed on the tripod was predesigned which will be discussed later. Then, the 11th image was taken using fixed camera on the tripod. These 11 images were later used to back-calculate the camera positions where each image was taken. This will ensure that the camera positions were always known during the whole testing process. After the two cameras were fixed, the cameras were ready for capturing images of the tensile tests. During the tests, the two cameras took the images simultaneously for each minute. This image acquisition rate was selected so that a total of 30 images were obtained for photogrammetric analysis using the proposed method. The two cameras were controlled by wireless shutter release timer remote control, which can avoid damaging image integrity and quality caused by camera vibration when pressing the camera shutter button. The image frames were saved into a file and analyzed for the 3D deformation and the strain distribution.

Table 5.2. Parameters of the camera used in this study

Camera IDs	Focal length(mm)	Format size		Principal point		Radial distortion			Tangential distortion	
		Width(mm)	Height(mm)	P_X (mm)	P_Y (mm)	K_1	K_2	K_3	P_1	P_2
		Before idealization								
Camera 1	55.7741	24.0022	15.8961	12.4170	7.9842	6.222×10^{-5}	0	0	2.205×10^{-5}	2.130×10^{-5}
Camera 2	83.3400	36.0025	24.0000	18.2279	11.8929	2.551×10^{-5}	0	0	3.363×10^{-6}	4.688×10^{-6}

Camera IDs	Focal length(mm)	Format size		Principal point		Radial distortion			Tangential distortion	
		Width(mm)	Height(mm)	P_X (mm)	P_Y (mm)	K_1	K_2	K_3	P_1	P_2
		After idealization								
Camera 1	55.7741	25.1509	16.6566	12.5754	8.3283	0	0	0	0	0
Camera 2	83.3400	36.8866	24.589	18.4433	12.2945	0	0	0	0	0

5.2.3 Camera Position Design

In the abovementioned procedures, we mentioned that the camera position was predesigned. Camera position design is a key step in the proposed method. Camera position design means the determination of a location where we place and fix the two cameras during the tensile tests. This step is important because it can largely affect the results of the proposed method. If the camera positions were not appropriately designed, it may lead to inaccurate results or even failure in the photogrammetry analysis. Therefore, the camera positions should be carefully designed before image acquisition. To design the camera position, we drew two concentric arcs on the floor in front of the tensile test equipment. The center of the arcs was located at the center of the load frame. Two arcs were needed because the two cameras have different focal lengths and the relative distances between the geogrid specimen and the two cameras are different. Eleven candidate camera positions were selected on each of the arcs (as shown in Figure 5.3).

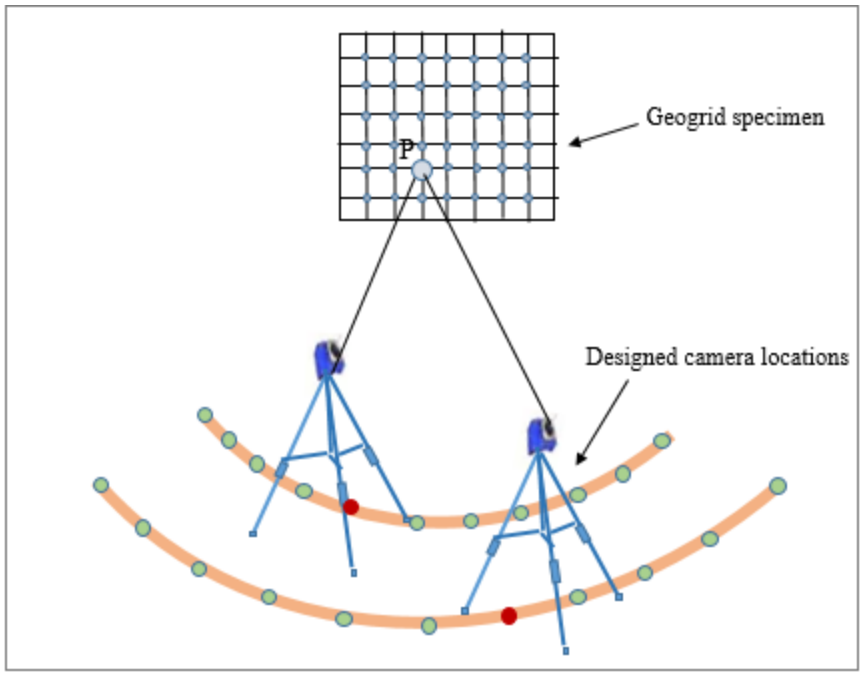

Figure 5.3 Camera position design

In order to determine the two optimum camera positions for the two cameras, we randomly selected one candidate camera position on each of the arcs and placed the cameras at these locations to perform 3D reconstruction of the geogrid using PhotoModeler UAS. For some camera positions, it was easier to obtain better quality images which means more coded targets on the geogrid specimen were correctly recognized in these images. In addition, it can obtain relatively stable and accurate 3D reconstruction results when using these camera positions. These camera positions were then selected as predesigned camera positions. Figure 5.3 shows the results of camera position design. The two red dots represent the designed camera positions.

5.3 Results and Discussions

The camera positions and 3D coordinates of the specimen before the tensile test are determined by conventional photogrammetry. In this study, a commercial photogrammetry software called PhotoModeler UAS was used to back-calculate the camera positions and

reconstruct the 3D models of the specimen before the tensile test. The results are shown in Figure 5.4.

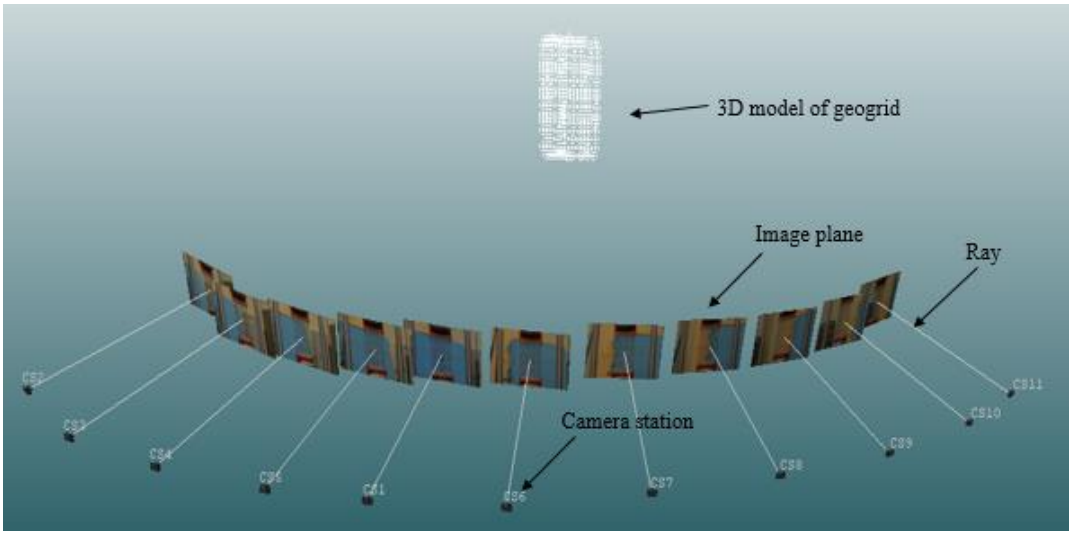

a)

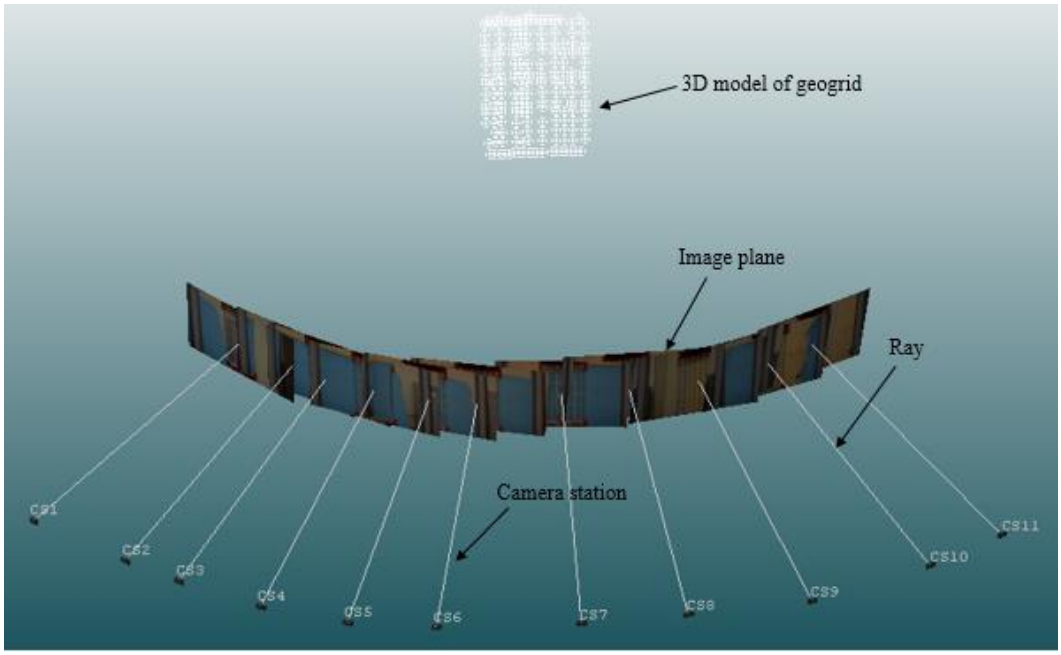

b)

Figure 5.4 3D models of the specimen and camera stations: a) 3D model of the specimen and camera stations for the first camera; and b) 3D model of the specimen and camera stations for the second camera.

5.3.1 Actual and Designed Camera Positions and Shooting Directions

As discussed previously, most existing image-based methods require manual control of camera positions and shooting directions. Figure 5.5 shows the comparison of actual camera positions and designed camera positions. Actual shooting directions and designed shooting directions are also shown in Figure 5.5. Square points and dashed lines represent designed camera positions and shooting directions for manual control. Round points and solid lines represent actual camera positions and shooting directions back-calculated from photogrammetry. As can be seen from the figure. It is not possible to accurately control neither the camera positions nor the shooting directions. The average deviation of camera positions between actual camera positions and the designed camera positions is 53.9 mm and the average deviation of shooting direction between actual shooting direction and the designed shooting direction is 1.1 degrees. This is probably because the center of the camera is difficult to control and unknown. In addition, it requires moving of camera and tripods and this manual operation can unavoidably lead to misleading results.

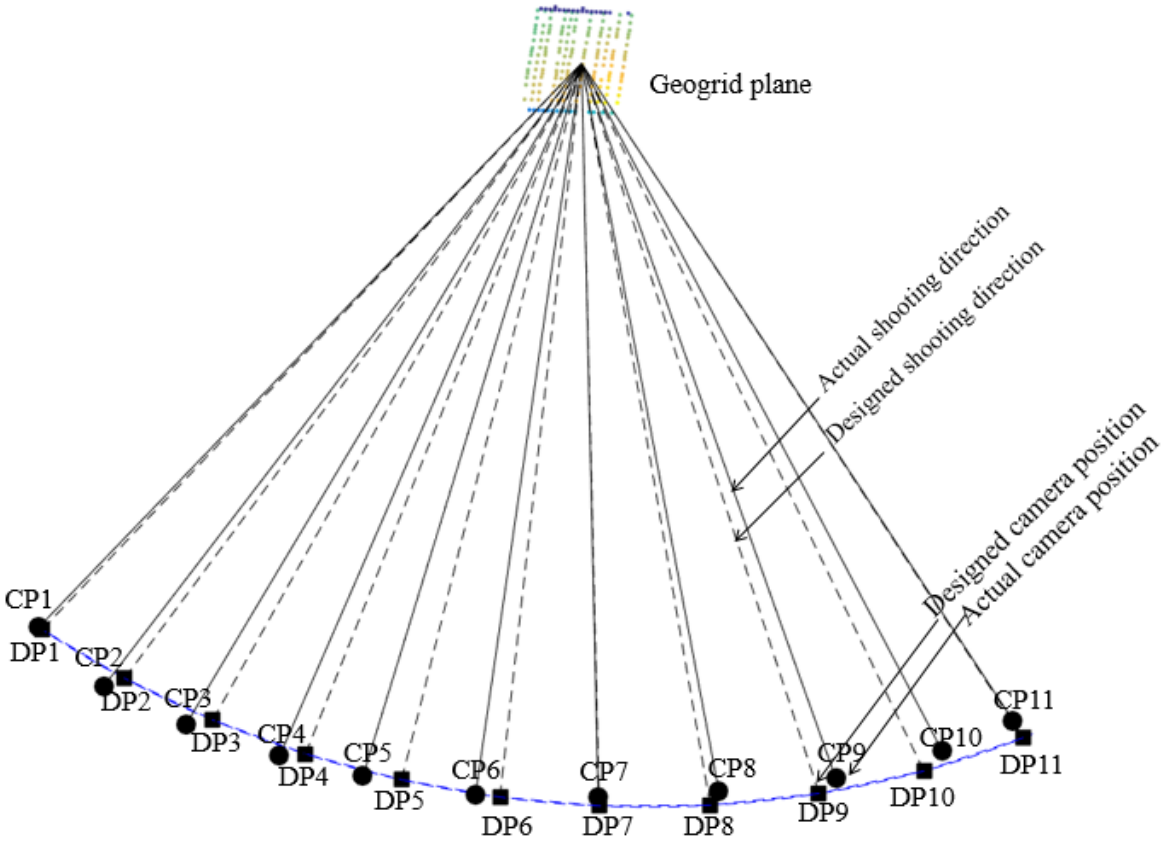

Photo ID / Deviation	1	2	3	4	5	6	7	8	9	10	11
Camera location (mm)	9.22	56.11	63.05	59.10	86.84	55.08	22.96	48.59	63.27	77.36	51.52
Shooting direction (degree)	0.26	0.75	1.35	1.49	2.46	1.58	0.10	0.78	1.50	1.90	0.16

Figure 5.5 Comparison of actual and designed camera positions and shooting direction.

Therefore, it can be concluded that it is almost impossible to accurately control the camera positions and shooting directions. This limitation in the existing image-based methods can lead to unreliable results. In addition, as discussed later, the geosynthetics plane is changing

due to non-uniform deformation. Therefore, the requirement that the shooting directions are always exactly perpendicular to the geosynthetics plane is impossible to satisfy.

5.3.2 Analysis of the Accuracy of the Proposed Method

To validate the effectiveness and accuracy of the proposed method, two validation tests were performed. The first validation test involves comparisons of the deformation results obtained from the proposed method and machine. The second validation test deals with the comparison of the deformation results obtained by the proposed method and the extensometer. The accuracy analysis results are presented in this section.

The proposed photogrammetric method requires a scale to determine the 3D real-world coordinates of the points on the geogrids. This scale must be consistent with the real size of the geogrid. We already know that the MTS Landmark 370 load frame machine is used for testing purposes to perform strain controlled tests and the displacements of the machine are calibrated using the machine's own scale. As a result, the controlled displacement of the machine was used as the scale in the photogrammetric method. As can be seen in Figure 5.2b, a row of coded targets on the clamp were used for scale calibration. The 3D coordinates of these points over time were calculated using the photogrammetric method. Then the displacements of these points can be obtained. These displacements were also measured by the machine. The average displacements of the points obtained by the photogrammetric method and the machine were compared and the scale of the photogrammetric method can thus be determined.

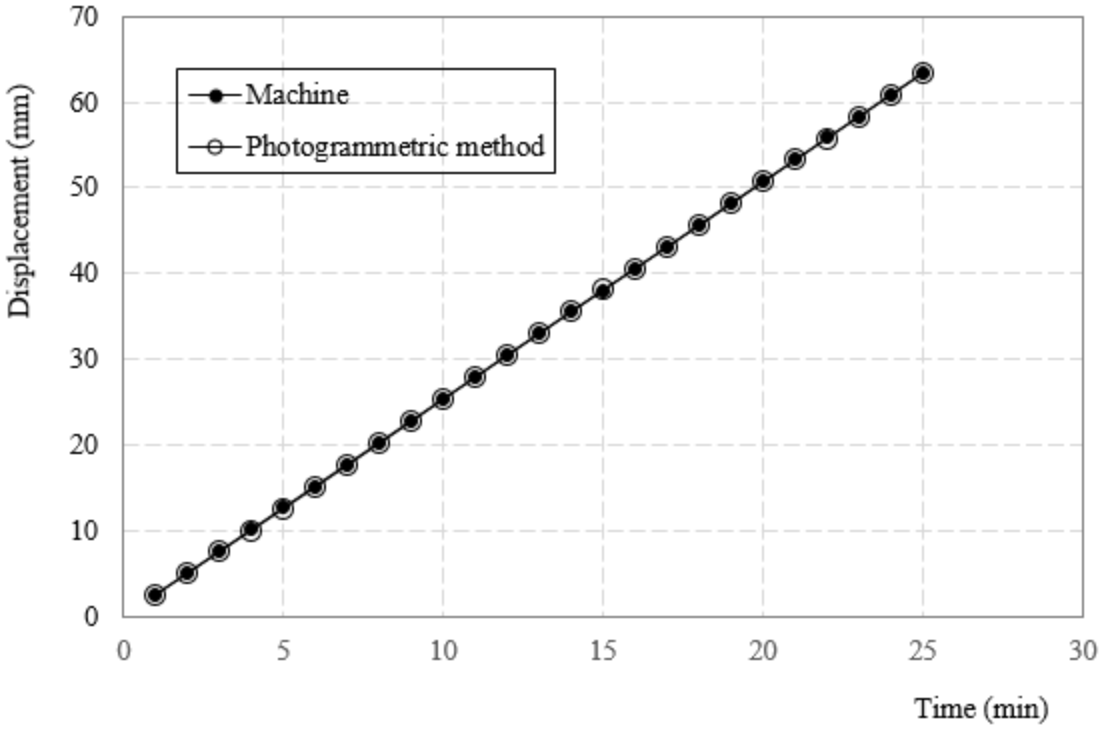

Figure 5.6 Comparison of displacements obtained by machine and the proposed method

Figure 5.6 shows the comparison of displacement results from the proposed method and machine with time. The average displacement difference between the two methods is 0.25% and the average absolute displacement difference is 0.038mm. An image-based method for measuring the strain distributions in geosynthetics has gained much attention in the past years (Aydilek et al., 2004; Kutay et al., 2006). In their paper, an average accuracy of 8% has been reported by comparing their image-based method and extensometer (Aydilek et al., 2004). Therefore, our proposed method shows much higher accuracy than existing methods.

There are several reasons why the proposed photogrammetric method has such high accuracy. First, the cameras used for tensile tests are calibrated. As discussed previously, camera calibration is important for eliminating image distortion and obtaining the optical camera parameters which are important for back-calculating the camera positions and determining the

3D coordinates of objects. However, many existing image-based methods fail to calibrate cameras, which can lead to unreliable results. Second, the camera positions and shooting directions are back-calculated using photogrammetry rather than being controlled manually. In addition, these back-calculated camera positions and shooting directions can be further refined using a global optimization called bundle adjustment. Bundle adjustment has been discussed in section 5.1 and will not be talked here. However, it is worth emphasizing that it is crucial for obtaining the accurate camera positions and 3D coordinates of the objects. Third, coded targets were used in the photogrammetric method. These coded targets are center dot targets whose 3D coordinates will be determined. With these coded targets, computer-vision-guided marking can produce point positions precise to less than a pixel. This is far more precise than both feature matching or manual marking methods.

5.3.3 Evaluation of the Full Field Displacement and Strain of Geogrids

The 3D coordinates of the coded targets placed on the geogrids are calculated using the proposed multi-camera based photogrammetric method. The full field displacements and strain in the geogrid during the tensile test can thus be obtained. Conventional methods such as LVDT and extensometer simply assume that the deformation of the geogrid specimen during the tensile tests is uniform within the geogrids and local deformation is not considered in the geogrid deformation measurements. However, by using our photogrammetry method in this study, it is demonstrated that the geogrid specimens can undergo large local deformation, and the proposed method is capable of capturing this local deformation.

Figure 5.7 shows the changes in displacement with time. Although the displacements of all points on each column rib are obtained, some representative column ribs or row ribs are selected to demonstrate the effectiveness of the proposed photogrammetric method. In this study,

we focused on the changes in displacement of four column ribs in the vertical direction, column A rib, column F rib, column G rib, and column J rib, and the ninth row rib in the horizontal direction. The changes in displacements of column A with time are shown in Figure 5.7a. As can be seen from the figure, the points at the lower locations have larger displacements. For example, the displacement of A4 is larger than A2 and A16 has the largest displacement. This makes sense because the lower points have accumulative displacements that transferred from the displacements of the upper points. From this figure, a sudden change in displacement when the testing time was 15 minutes is observed for almost all points. One possible reason for this sudden change is that dismounting the extensometer has disturbance on the geogrid specimen, which causes additional displacements of the geogrid. This is partly verified by the fact that at testing time 15 minutes the extensometer was carefully removed from the geogrid specimen in order to protect the extensometer from damage. Another interesting phenomenon on this figure is that the response of different points to the disturbance caused by dismounting the extensometer is different. The lower the point is, the smaller effects it has on this point. The extensometer disturbance has the largest effects on A2 while the effect on A16 is almost neglected. This indicates that the mechanical interruption can cause localized deformation of the geogrid specimen and the deformation of the geogrid is not uniform. This will be further verified in the following discussion.

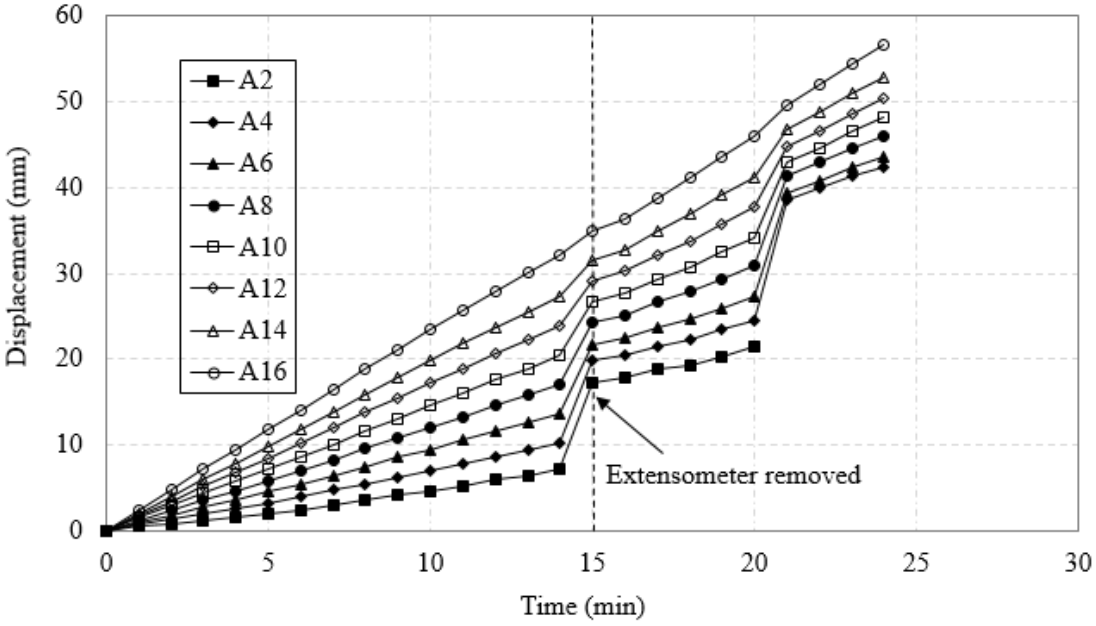
A2
A4
A6
A8
A10
A12
A14
A16
Displacement (mm)
Time (min)
Extensometer removed
0
10
20
30
40
50
60
0
5
10
15
20
25
30

a)

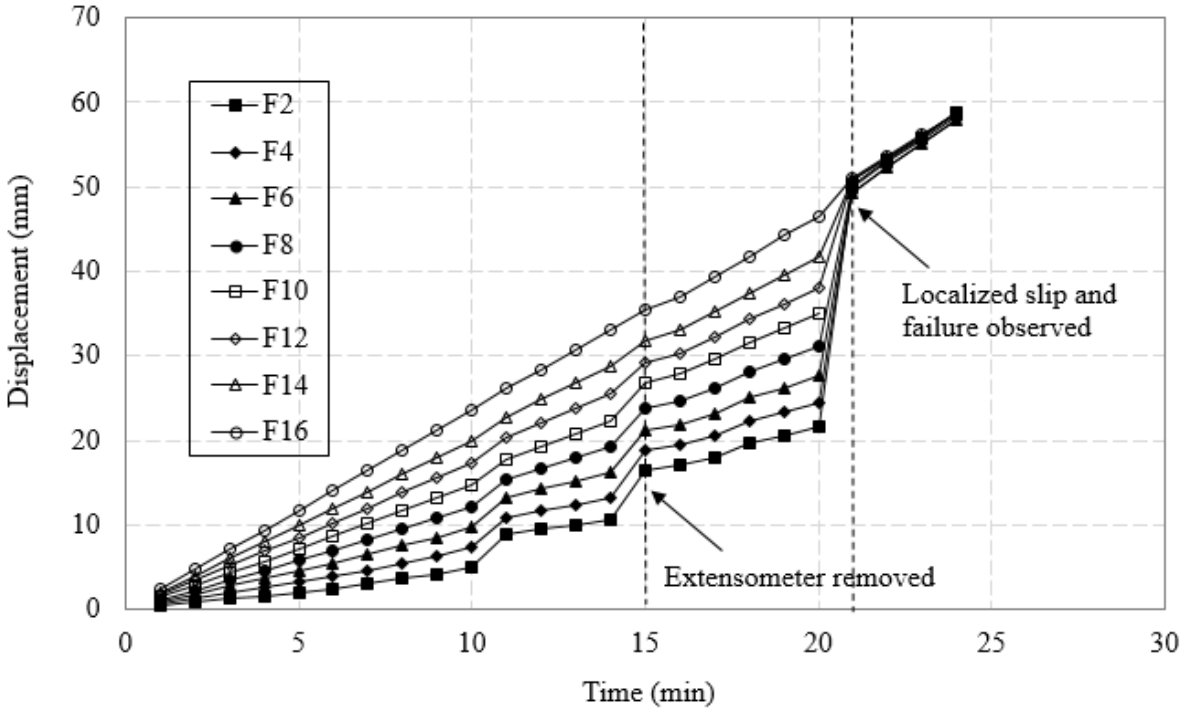
F2
F4
F6
F8
F10
F12
F14
F16
Displacement (mm)
Time (min)
Localized slip and
failure observed
Extensometer removed
0
10
20
30
40
50
60
70
0
5
10
15
20
25
30

b)

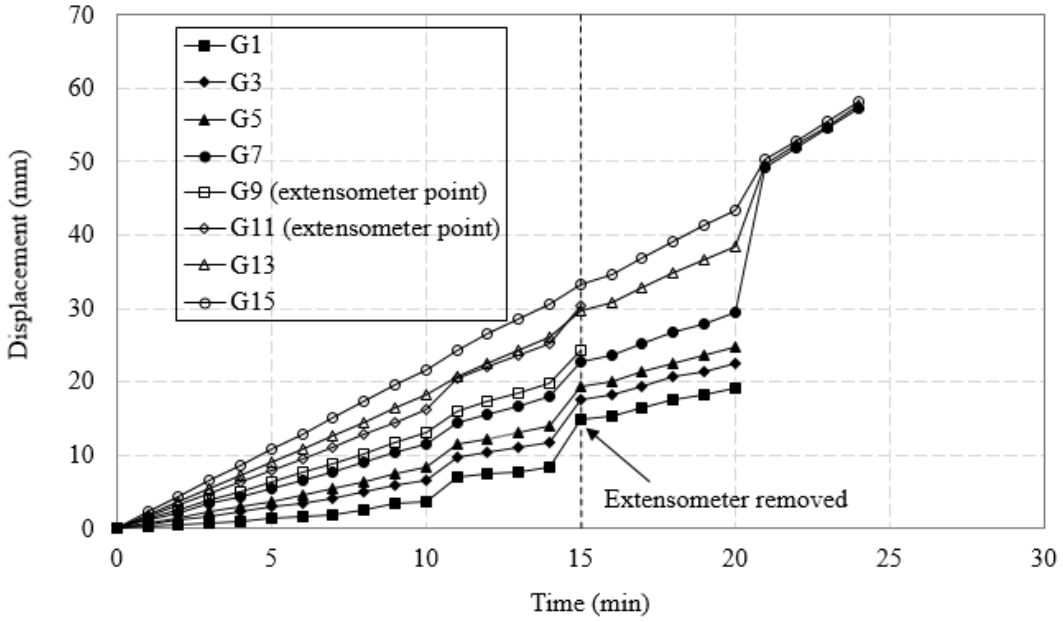

c)

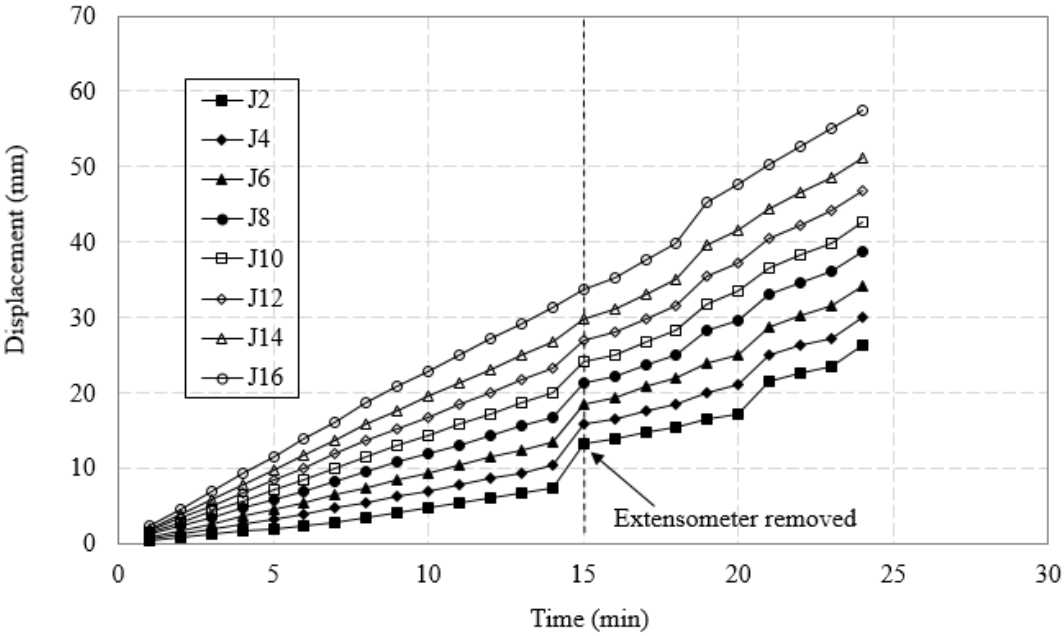

d)

Figure 5.7 Displacement-time relationship curve of the geogrid: a) column A in the vertical direction; b) column D in the vertical direction; c) column G in the vertical direction; d) column J in the vertical direction.

Figure 5.7b shows the displacement versus time curve for column rib F. Similar results to column rib A were found for this column rib. The possible disturbance caused by dismounting the extensometer leads to a jump in displacements for almost all the points. However, different from column rib A, after a testing time of 20 minutes, all the points converged into one point and have almost the same displacement. This is perhaps due to the fact that the top part of the geogrid specimen experienced a localized slip and failure around the testing time of 20 minutes. As a result, this column rib on the geogrid experienced rigid translation instead of continuous elongation. This hypothesis can also be supported by the figure of the specimen when testing time is larger than 20 minutes (as shown in Figure 5.9b). In Figure 5.9b, it can be clearly seen that the top of column rib F reached failure (marked by a small ellipse), and one horizontal row rib slipped out of the clamp, which is marked by a long ellipse.

Figure 5.7c shows the displacement curve of column rib G, which contains two points measured by extensometer. The points measured by extensometer have similar displacements to other points. This demonstrates the effectiveness of the proposed method. It is also noted that the displacements of G1, G3, G5, and G7 are missing after testing time of 20 minutes. This is because as the deformation of the geogrid becomes larger and larger, many coded targets on the geogrid dropped down.

Figure 5.7d presents the changes in displacement of column rib J. Similar to other column ribs, extensometer disturbance induced localized deformation observed continuously in this column rib. However, as shown in the figure, after the testing time of 20 minutes the displacement curves of the points are separated from each other and all the points have independent displacements. It seems that the localized slip and failure discussed previously has very limited influence on the displacement of this column rib. This is also supported by the

picture of the localized slip and failure (Figure 5.9b). In Figure 5.9b, no localized failure is found in column J. However, the localized slip and failure detected in other column ribs still has a small influence on the displacements of this column. Thus, a small jump in displacement at testing time of 20 minutes is also observed.

In order to evaluate the displacement of points in the same horizontal line, the ninth row column is selected as a representative row rib and the displacements of points on this rib are investigated. The results are shown in Figure 5.7e. Since all the points on this rib are almost on the same horizontal line their displacements and the changes in displacements are expected to be almost the same or at least very similar. This is true for the time period of 0 to 20 minutes. However, a discrepancy exists between displacements of different points when the testing time is greater than 20 minutes. The displacements of these points can roughly be divided into two categories. The first category involves A9, C9, D9, E9, and H9 and is affected by a jump in displacement occurred at testing time 21 minutes. As discussed previously, localized slip and failure at the top of geogrid was detected at testing time 21 minutes. Therefore, the points in the first category experienced localized deformation caused by localized slip and failure. The second category contains J9 and K9. The displacements of these two points after testing time 20 minutes, however, do not seem to be affected by the observed localized slip and failure. This is again confirmed by the picture of observed localized slip and failure of the geogrid (Figure 5.9b). In Figure 5.9b, compared with other column ribs, column rib J and column rib K did not undergo any slip or rupture. This is the reason why only the displacements of points on these two column ribs are not affected by the localized slip and failure. The results clearly indicate that the proposed photogrammetric method is capable of identifying the localized deformation of the geogrid.

In order to evaluate the strain distribution in the geogrid. The localized strain in each short segment formed by two adjacent points is calculated. For example, A9-11 represents the segment formed by point A9 and A11. The localized strain in segment A9-11 is calculated as follows:

$$\varepsilon = \frac{L_t - L_0}{L_0} \tag{15}$$

where L_t is the length of segment A9-11 at testing time t, and L_0 is the initial length of segment A9-11. Therefore, using the 3D coordinated of the points in each time step the strain in each segment can be calculated and the strain distribution can thus be obtained.

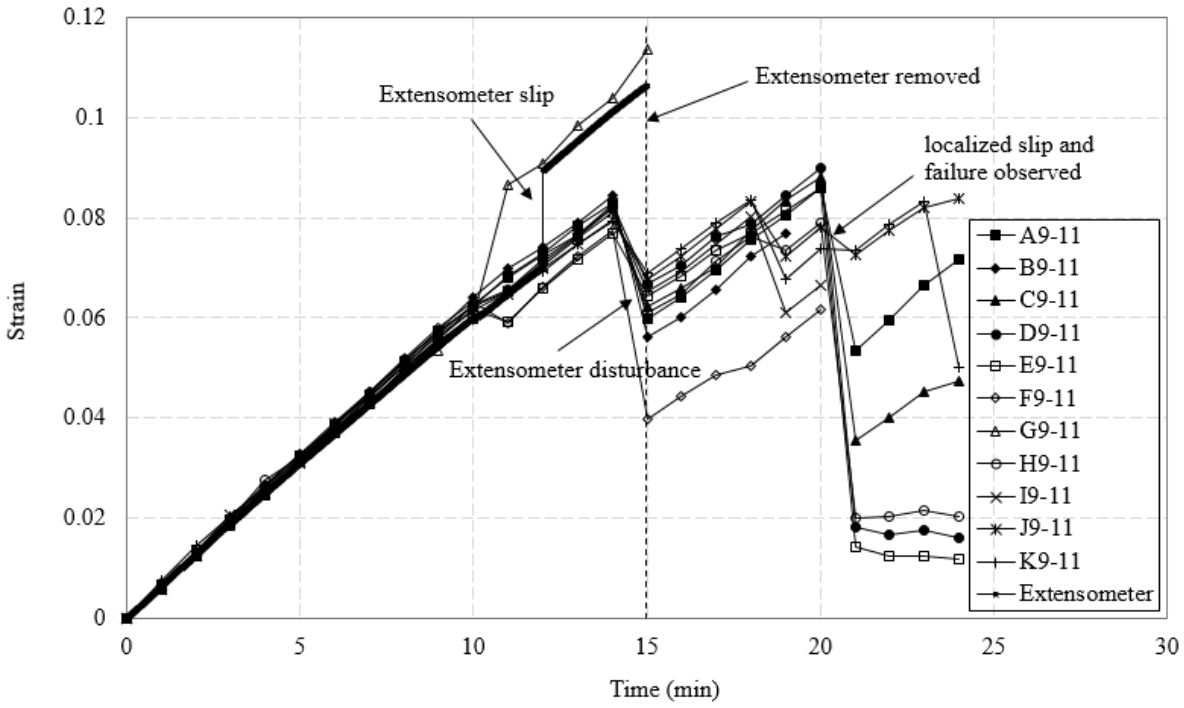

Figure 5.8 Comparison of strain obtained by extensometer and the proposed method

Figure 5.8 shows the localized strain in the segments which are formed by the points on the ninth row and the eleventh row. The points on these two rows are selected because the two measuring points of extensometer are also on the ninth and eleventh row so that the results from the photogrammetric method and extensometer can be compared. The measured results by the two methods agree very well for the first stage of the test. However, an interesting phenomenon was observed when a large deformation rate occurs. It seems that the extensometer failed to capture this deformation rate change, and the obtained deformation data from extensometer lagged behind the real deformation. On the other hand, our proposed method can fully capture the whole deformation rate change process, and the data points are more smooth and reasonable. One potential reason for this might be that the photogrammetric method is a non-contact method which receives no physical interruption and is always capable of tracking the real-time deformations of the specimen. Another advantage of the method is that it can measure a large range of displacements until the specimens reach failure. As can be seen in Figure 5.9a, the extensometer was removed when the testing time was 15 minutes in order to protect the extensometer from damage, which means only the deformation of geogrid during the first 15 minutes can be recorded by the extensometer. In contrast, the photogrammetric method can measure a much larger range of displacements. As can be seen from Figure 5.8, the deformation of the geogrid continued to increase after the extensometer was removed and this increase was not monotonous.

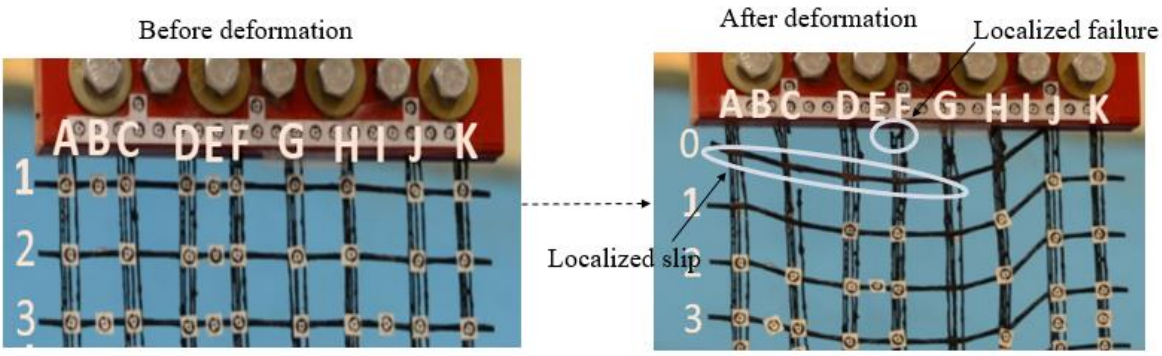

a) b)

Figure 5.9 Picture of observed localized slip and failure of the geogrid: a) the top part of the geogrid before the deformation; and b) the top part of the geogrid after deformation and the observed localized slip and failure.

Figure 5.10 shows the load versus strain curve of the geogrid at different locations. In Figure 5.10a, the load versus strain curve of the column rib A is presented. A1-2 denotes the load-strain relationship of the segment formed by point A1 and A2. As can be seen from Figure 5.10, almost all the segments have similar load-strain curve trend but with different quantity.

This different quantity indicates that the modulus and tensile strength are different in different locations of the geogrid. Similar results were also found in Fig. 5.10b. From this figure, different modulus and tensile strength can also be determined. It is noted that conventional methods usually assume that the modulus and tensile strength is uniform within the whole geogrid specimen. By using the proposed photogrammetric method no such assumption is needed and the modulus and tensile strength at any locations of the geogrid can be obtained.

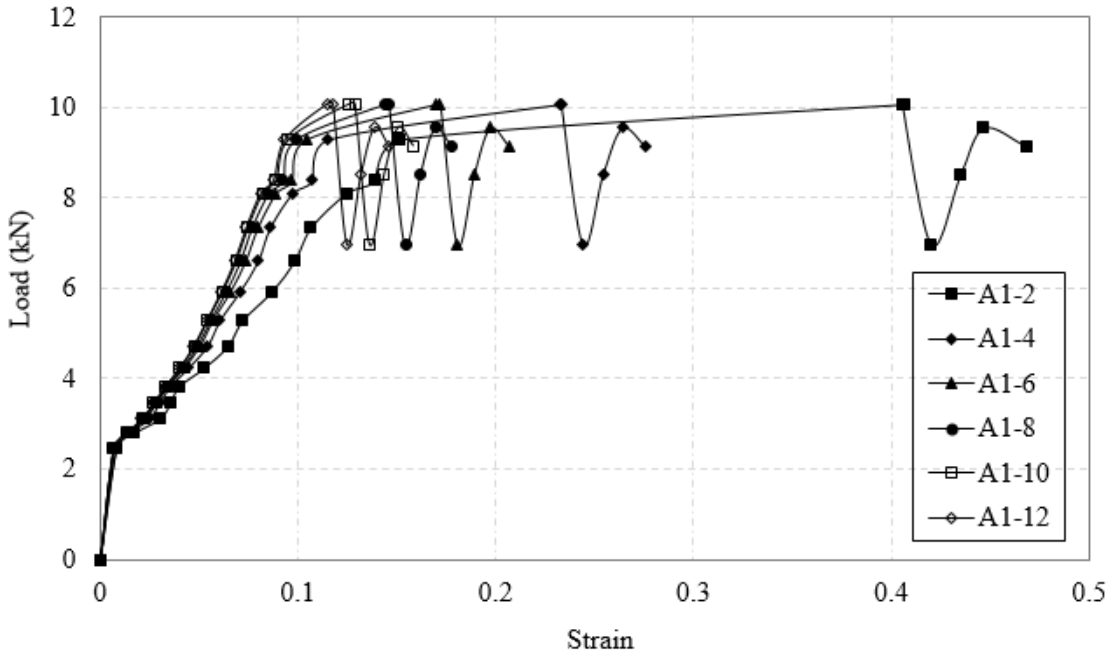

a)

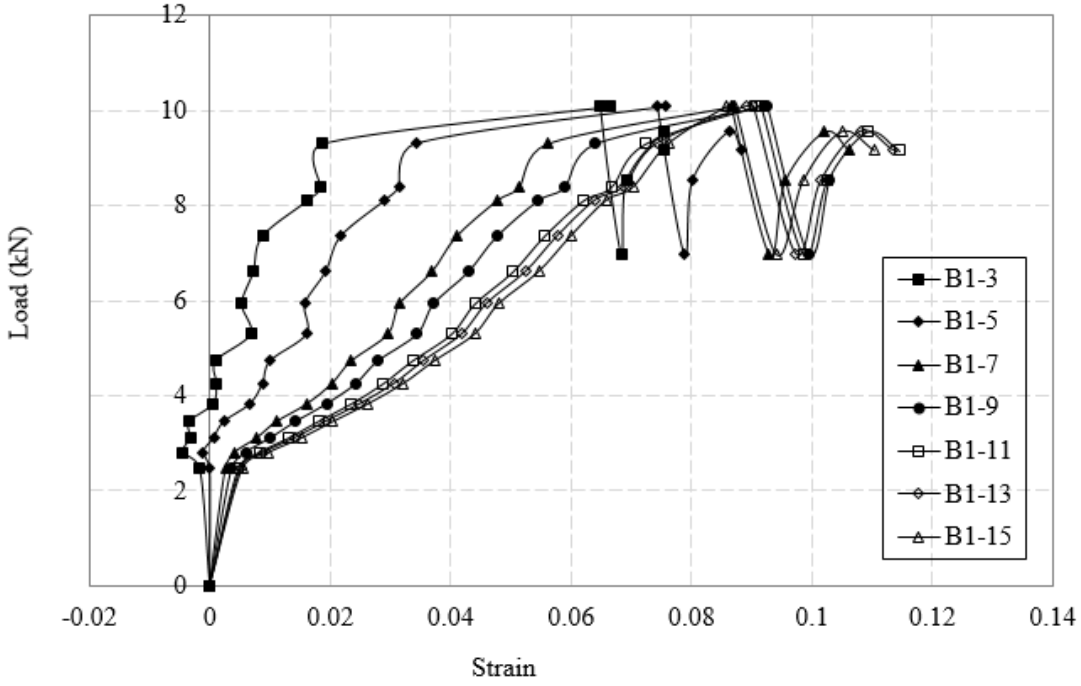

b)

Figure 5.10 Load-strain relationship curve of the geogrid: a) column A in the vertical direction; b) column B in the vertical direction

5.3.4 Evaluation of the Three-Dimensional Deformation of the Geogrids

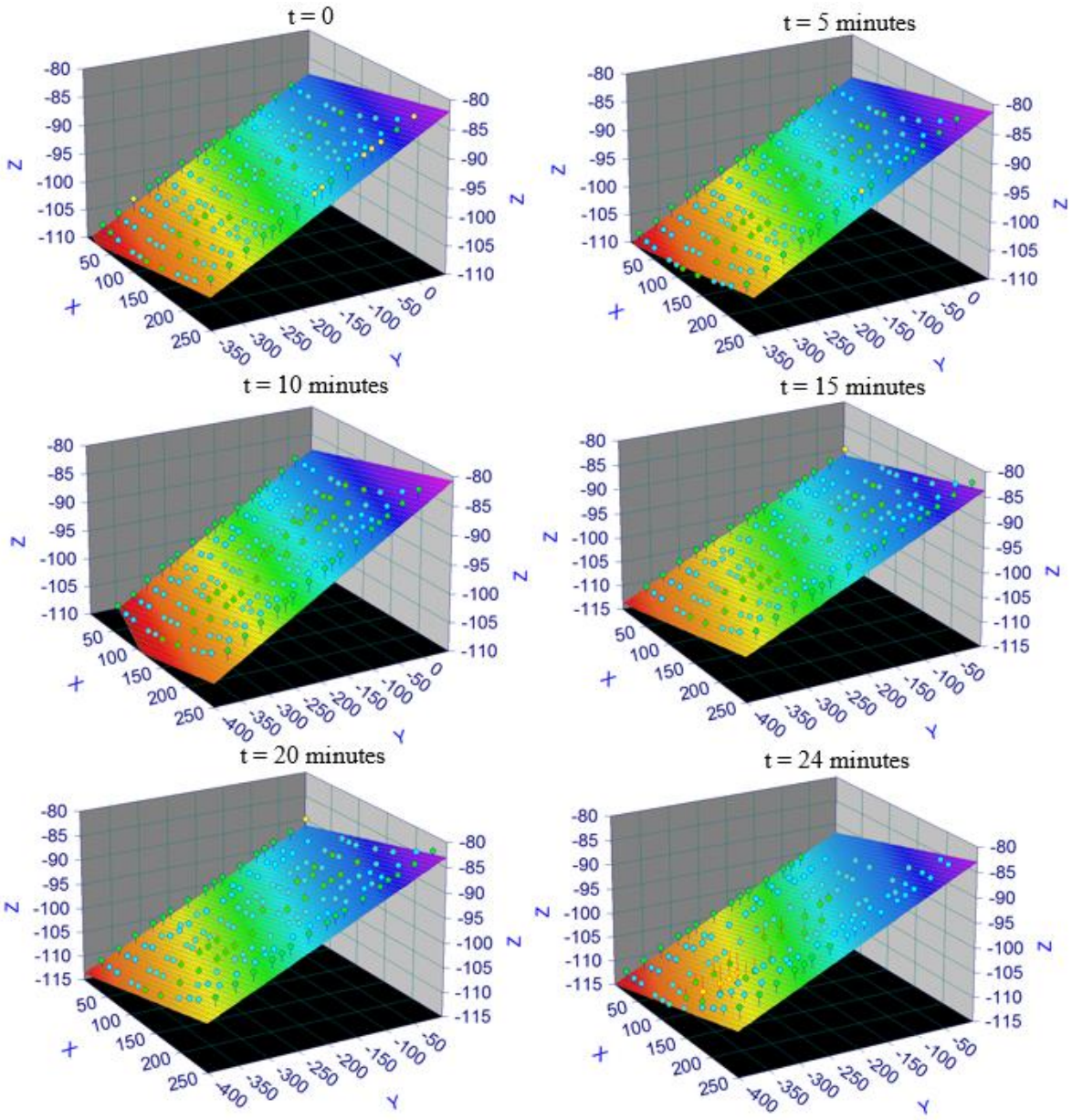

Figure 5.11 Changes in locations of the geogrid specimen in 3D space over time

Another advantage of the proposed photogrammetric method is that it can measure the three-dimensional deformation of the geogrid. As discussed previously, conventional methods assume that the geogrid is initially in one single plane and must maintain in the same plane during the whole testing. However, this assumption is proven to be invalid by evaluating the three-dimensional deformation of geogrid using the proposed photogrammetric method. Figure 5.11 shows the 3D locations of the geogrid in each time step. The points in the figure denote the coded targets which were placed on the geogrid specimen. It is noted that the viewpoint for each image in the figure is all the same so that the change in deformation and 3D locations can be compared. From these images, we can see that the geogrid plane rotated continuously as testing time increases.

This phenomenon will be confirmed in Figure 5.13 where the deviation angles of the fit planes are discussed. Therefore, it is highly possible that the geogrid will not maintain in the same plane during testing. This is further confirmed by Figure 5.12. In Figure 5.12, the best fit planes of the geogrid in each time step are presented. From the figure, it is clearly seen that the points are not on the same plane. In addition, as testing time increases, these points deviated more from the fit plane. This is reasonable because as testing increases both the in-plane deformation and out-of-plane deformation becomes larger. The R-squared and deviation of the normal direction of each fit plane are calculated and shown in Figure 5.13. The R-squared of the best-fit plane is initially 97.1% which is less than 100%. This clearly indicates that the plane is initially not in the same plane. As time increases, the R-squared decreases and the R-squared of the best-fit plane for the last image is only 95.2 %. Similar results were found in times of the deflection angle of the fit planes in different time steps. As time increases, the deflection angles become larger. The deflection angle of the best-fit plane for the last image is 0.68 degree. These

data support the phenomenon that the geogrid rotated continuously during the tensile test as discussed before. These results demonstrate that the geogrid specimen is neither initially in one single plane nor maintains a plane during the tensile tests. In fact, the geogrid undergoes significant out-of-plane deformation during the tests. Therefore, the planar assumption in the existing methods for measuring the deformations of geogrids is not valid.

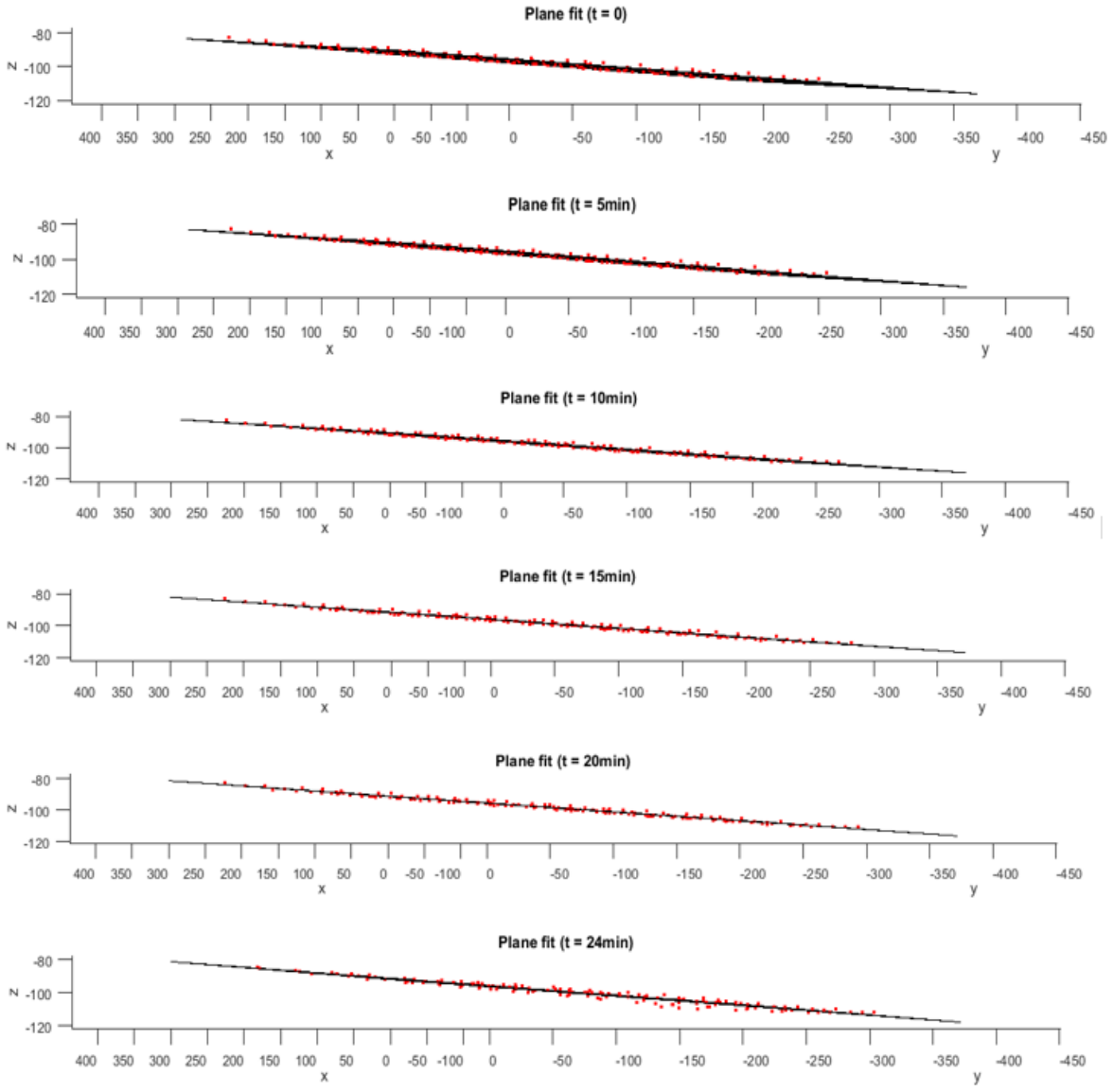

Figure 5.12 Best fit planes of the geogrid specimen over time

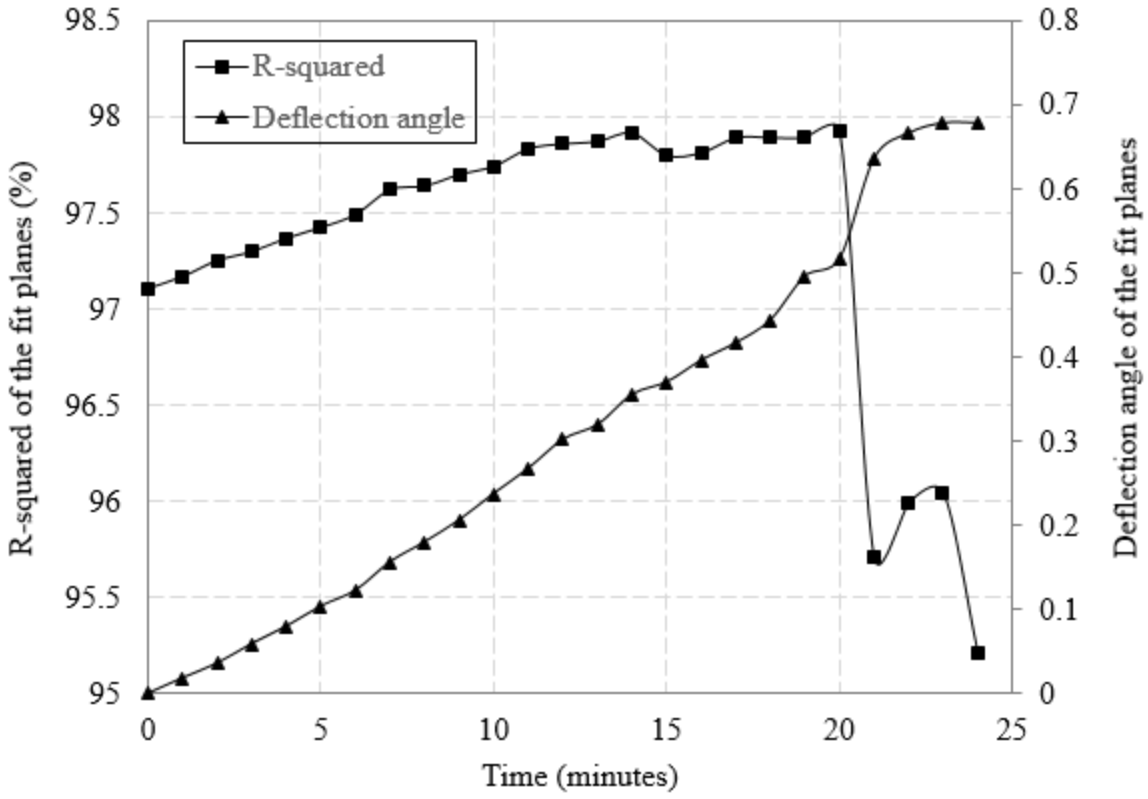

Figure 5.13 R-squared and deflection angles of the best fit planes of the geogrid specimen over time.

CHAPTER 6 SUMMARY AND CONCLUSIONS

The aim of this study was to develop an accurate, efficient, and cost-effective 3D reconstruction method to measure both global and localized deformations of unsaturated soils during triaxial tests. To this end, literature review was performed first to summarize the progress and limitations of previous studies related to triaxial tests on unsaturated soils, target recognition, and 3D reconstruction. Next, a deep learning-based method was developed to accurately and efficiently detect the coded targets on the triaxial cells and soil membranes. The ID numbers of each coded target were also determined using image processing techniques. Using these coded target detection results as input, a 3D reconstruction approach was proposed for determining the 3D points on the triaxial cell and frame rods. A multi-ray tracings technique was proposed to correct the refraction occurred at the air-acrylic cell-interface and the acrylic cell-water interface, and the 3D points on the unsaturated soils can also be obtained. Finally, the application of the photogrammetric method has been extended to the geosynthetics tests. A multi-cameras-based photogrammetric method was developed and used to measure the 3D full-field displacements of the geogrids. Based on the testing results and analyses, the following conclusions were made:

- A deep learning-based method for highly accurate target recognition was developed. In this method, a multi-stage detection approach using faster R-CNN algorithm and transfer learning technique was proposed. The triaxial cell detection, sub-region detection, and target detection were performed consecutively. This multi-stage detection approach has proven to be five times more efficient than the template matching method. Based on the deep learning aided target recognition results, the high precision target center has been obtained by the image processing technique. Results indicated that the average pixel

coordinate difference obtained from the proposed method and commercial software is only 0. 1 pixel.

- Validation of the proposed target recognition method has been performed on both a cylinder and a triaxial cell. The cylinder recognition achieved performance with 96.7% accuracy with 30 test images. The triaxial recognition achieved performance with 100% accuracy with 120 test images. The target identification tests on both cylinder and the triaxial cell were capable of achieving a nearly 100% accuracy.
- This is the first study to successfully perform accurate and automated target recognition using deep learning. This study demonstrated that the deep learning aided target recognition method is suitable for target recognition even with a relatively small image dataset. In addition, a target recovery algorithm has been proposed to recognize more targets. The proposed approach produces highly automated and accurate target recognition results which can be used as input to 3D reconstruction projects for many different applications, such as volume-change measurement of unsaturated soils.
- A joint approach from both photogrammetry and computer vision to determine the camera poses from which the accurate 3D models of the unsaturated soils was proposed. Since it makes full use of the benefits of both photogrammetry and computer vision, this joint approach has the advantages of both high-accuracy and high-efficiency. The performance of this proposed method was validated by computing the camera poses and reconstructing the 3D models of a cylinder sample.
- A method capable of creating accurate 3D models of target objects, like unsaturated soil specimens, from multiple views in a highly automated way, was also developed in this study. Combined use of computer vision technique and photogrammetry enables the 3D

reconstruction process to be highly automated and accurate. The whole process was implemented in a Matlab program. Validation test results indicate that the relative error of our method is 0.067%. This method is easy to integrate with a newly proposed ray tracing technique and a fully automated and accurate program for measuring volume changes of unsaturated soil specimens in triaxial tests can be obtained.

- The proposed photogrammetric method is based on conventional photogrammetry and a proposed multi-camera-based photogrammetric method which extends from one-camera based photogrammetry to multi-camera based photogrammetry. This method can be successfully used in dynamic tests where the displacements continue to increase such as tensile tests on geosynthetics.
- The proposed photogrammetric method is a non-contact, cost-effective and highly accurate method. It is equivalent to installing unlimited non-contact LVDTs on the geosynthetics with high accuracy and large measurement ranges. Thus, much more information regarding the deformational and strength properties, such as displacement, strain, modulus and tensile strength at any locations of the geosynthetics can be obtained from the proposed photogrammetric method. Apart from conventional tensile test equipment, it only requires two commercially available digital cameras which cost about $ 2000. The average absolute difference in displacement obtained by the machine and the proposed photogrammetric method is 0.25%, and the average absolute error is 0.038 mm.
- Conventional methods assume that the geogrid is initially in one single plane and must maintain in the same plane. As a result, very often they only measure two-dimensional deformation of geogrid. In contrast, the proposed photogrammetric method can accurately determine the 3D coordinates of the points on the geogrid so that the 3D deformation of

the geogrid can be obtained. Results obtained from the proposed photogrammetric method indicate that the geogrid is not initially in one single plane and the geogrid plane continues to rotate and change in direction. The initial R-squared of the best-fit plane was 97.1 % and decreased to 95.2% at the final stage of the test. And the deflection angle of the normal direction of the best fit planes continued to increase. These findings indicate that the assumption in the conventional method that the geogrid is always in one unchanged single plane is invalid and may lead to unreliable and inaccurate results.

REFERENCES

Adams, B.A., Wulfsohn, D., and Fredlund, D.G. 1996. Air volume change measurement in unsaturated soil testing using a digital pressure-volume controller. ASTM Geotechnical Testing Journal, 19(1): 12-21.

Ahn, S. J., and Schultes, M. (1997). A new circular coded target for the automation of photogrammetric 3D-surface measurements. Optical 3-D Measurement Techniques IV (Eds.A. Gruen &H. Kahmen).Wichmann, Heidelberg, Germany. 225–234.

Alshibli, K.A., Sture, S., Costes, N.C., Frank, M.L., Lankton, M.R., Batiste, S.N., and Swanson, R.A. 2000. Assessment of local deformation in sand using X-ray computed tomography. ASTM Geotechnical Testing Journal, 23(3): 274-299.

ASTM D6637/D6637M-15 Standard Test Method for Determining Tensile Properties of Geogrids by the Single or Multi-Rib Tensile Method, West Conshohocken, PA, 2015.

Aydilek, A.H., Guler, M., and Edil, T.B. 2004. Use of image analysis in determination of strain distribution during geosynthetic tensile testing. Journal of Computing in Civil Engineering, 18(1), 65-74.

Barazzetti, L., & Scaioni, M. (2010). Development and implementation of image-based algorithms for measurement of deformations in material testing. Sensors, 10(8), 7469-7495.

Bernat, K., & Tokarczyk, R. (2013). Automation of measurements of selected targets of photopoints in application to photogrammetric reconstruction of road accidents. Geomatics and Environmental Engineering, 7.

Beyer, H. A., Uffenkamp, V.anddervan Vlugt, G.(1995). Quality control in the industry with digital photogrammetry. Optical 3-D Measurement Techniques III(Eds.A. Gruen &H. Kahmen). Wichmann, Heidelberg, Germany. 533 pages: 29–38.

Bhandari, A.R., Powrie, W., and Harkness, R.M. 2012. A digital image-based deformation measurement system for triaxial tests, ASTM Geotechnical Testing Journal, 35(2): 209-226.

Bishop, A. and Donald, I. 1961. The experimental study of partly saturated soil in the triaxial apparatus. In Proceedings of the 5th international conference on soil mechanics and foundation engineering, Paris, July 17-22, 1:13-21.

Briechle, K., & Hanebeck, U. D. (2001). Template matching using fast normalized cross correlation. In Optical Pattern Recognition XII. International Society for Optics and Photonics. (Vol. 4387, pp. 95-102).

Cha, Y. J., Choi, W., & Büyüköztürk, O. (2017). Deep learning-based crack damage detection using convolutional neural networks. Computer-Aided Civil and Infrastructure Engineering, 32(5), 361-378.

Cha, Y. J., Choi, W., Suh, G., Mahmoudkhani, S., & Büyüköztürk, O. (2018). Autonomous structural visual inspection using region-based deep learning for detecting multiple damage types. Computer-Aided Civil and Infrastructure Engineering, 33(9), 731-747.

Chupin, O.A., Rechenmacher, L., and Abedi, S. 2012. Finite strain analysis of nonuniform deformation inside shear bands in sands. International Journal for Numerical and Analytical Methods in Geomechanics, 36(14): 1651-1666.

Clayton CRI, Khatrush SA (1986) A New Device for Measuring Local Axial Strains on Triaxial Specimens. Géotechnique, 36(4): 593-597.

Clayton CRI, Khatrush SA, Bica AVD, Siddique A. 1989. The use of Hall effect semiconductors in geotechnical instrumentation. ASTM Geotechnical Testing Journal, 12(1): 69-76.

Cronk, S., Fraser, C.and Hanley, H. (2006). Automated metric calibration of color digital cameras. Photogrammetric Record, 21(116): 355–372.

Desrues, J. 2004. Tracking strain localization in geomaterials using computerized tomography. X-ray CT for Geomaterials: 15-41.

Dai, J., Li, Y., He, K., and Sun, J. (2016). R-FCN: Object detection via region-based fully convolutional networks. Proc., Advances in Neural Information Processing Systems, Neural Information Processing Systems Foundation, Barcelona, Spain, 379–387.

Desrues, J., and Viggiani, G. 2004. Strain localization in sand: an overview of the experimental results obtained in Grenoble using stereophotogrammetry. International Journal for Numerical and Analytical Methods in Geomechanics, 28(4): 279-321.Easa, S. M. (2010). Space resection in photogrammetry using collinearity condition without linearisation. Survey Review, 42(315), 40-49.

Fraser, C. S. (1997). Innovations in automation for vision metrology systems. Photogrammetric Record, 15(90):901–91.

Fredlund, D. G., and Rahardjo, H. (1993). Soil Mechanics for Unsaturated Soils. New York: John Wiley and Sons, ISBN: 978-0-471-85008-3.

Fryer, J., Mitchell, H. and Chandler, J. (Eds.).(2007). Applications of 3D Measurements from Images. Whittles, Dunbeath, Scotland. 304 pages.

Gachet, P., Geiser, F., Laloui, L., and Vulliet, L. 2007. Automated digital image processing for volume change measurement in triaxial cells. ASTM Geotechnical Testing Journal, 30(2), 98-103.

Geiser F. 1999. Comportément mécanique d'um limon non saturé: étude expérimentale et modélisation constitutive. Ph.D. thesis, Swiss Federal Institute of Technology, Lausanne, Switzerland.

Geiser, F., Laloui, L., Vulliet, L., Rahardjo, H., Toll, D., and Leong, E. 2000. On the volume measurement in unsaturated triaxial test. In Unsaturated soils for Asia. Proceedings of the Asian Conference on Unsaturated Soils, UNSAT-Asia 2000, Singapore, May 18-19, pp. 669-674.

Girshick, R., Donahue, J., Darrell, T., and Malik, J. (2014). Rich feature hierarchies for accurate object detection and semantic segmentation. Proc., IEEE Conf. on Computer Vision and Pattern Recognition, IEEE, Piscataway, NJ, 580–587.

Grussenmeyer, P., & Al Khalil, O. (2002). Solutions for exterior orientation in photogrammetry: a review. The photogrammetric record, 17(100), 615-634.

Jones, D., (2000). Wide-width geotextile testing with video extensometry. Grips, Clamps, Clamping Techniques, and Strain Measurement for Testing of Geosynthetics. ASTM International.

Hartley, R. I., & Mundy, J. L. (1993). Relationship between photogrammmetry and computer vision. In Integrating photogrammetric techniques with scene analysis and machine vision. International Society for Optics and Photonics. 92-106.

Hattori, S., Akimoto, K., Okamoto, A., Hasegawa, H.andFraser, C. S. (1999). The design and use of coded targets for automatic measurement with a CCD camera. ASPRS Annual Convention, Portland, Oregon, USA. 928–935.

Hattori, S., Akimoto, K., Fraser, C.andImoto, H. (2002). Automated procedures with coded targets in industrial vision metrology. Photogrammetric Engineering & Remote Sensing, 68(5): 441–446.

He, K., Zhang, X., Ren, S., and Sun, J. (2015). Spatial pyramid pooling in deep convolutional networks for visual recognition. IEEE Trans. Pattern Anal. Mach. Intell., 37(9), 1904–1916.

He, K., Zhang, X., Ren, S., and Sun, J. (2016a). Deep residual learning for image recognition. Proc., IEEE Conf. on Computer Vision and Pattern Recognition, IEEE, Piscataway, NJ, 770–778.

Hoyos, L. R., Laloui, L., and Vassallo, R. 2009. Mechanical testing in unsaturated soils. In Laboratory and Field Testing of Unsaturated Soils, pp. 63-77. Springer Netherlands.

Krizhevsky, A., Sutskever, I., and Hinton, G. E. (2012). ImageNet classification with deep convolutional neural networks. Proc., Advances in Neural Information Processing Systems, Neural Information Processing Systems Foundation, Stateline, NV, 1097–1105.

Kutay, M. E., Murat, G., and Aydilek, A. H. 2006. Analysis of factors affecting strain distribution in geosynthetics. Journal of geotechnical and geoenvironmental engineering. 132(1), 1-11.

Laloui L, Pe´ron H, Geiser F, Rifa'i A, and Vulliet L 2006. Advances in volume measurement in unsaturated triaxial tests. Soils and Foundations, 46(3): 341-349.

Laudahn, A., Sosna, K., and Bohdp, J. 2005. A simple method for air volume change measurement in triaxial tests, ASTM Geotechnical Testing Journal, 28(3): 313-318.

Lin, H. and Penumadu, D. 2006. Strain localization in combined axial-torsional testing on kaolin clay, Journal of Engineering Mechanics, 132(5): 555-564.

Li, L. and Zhang, X, 2018. A New Approach to Measure Shrinkage Curves of Cohesive Soils. ASTM Geotechnical Testing Journal. 42(1), 1-18.

Li, Y., Qi, H., Dai, J., Ji, X., and Wei, Y. (2017). Fully convolutional instance-aware semantic segmentation. Proc., IEEE Conf. on Computer Vision and Pattern Recognition, IEEE, Piscataway, NJ.

Luhmann, T., Robson, S., Kyle, S., & Boehm, J. (2013). Close-range photogrammetry and 3D imaging. Walter de Gruyter.

Macari, E.J., Parken, J., and Costes, N.C. 1997. Measurement of volume changes in triaxial tests using digital imaging techniques, ASTM Geotechnical Testing Journal, 20(1): 103-109.

Mazurowski, M. A., Buda, M., Saha, A., & Bashir, M. R. (2019). Deep learning in radiology: An overview of the concepts and a survey of the state of the art with focus on MRI. Journal of Magnetic Resonance Imaging, 49(4), 939-954.

Mikhail, E.M., Bethel, J.S., and McGlone, J.C. 2001. Introduction to modern photogrammetry. Wiley. New York. ISBN 0-471-30924-9.

Mishra, S. R., Mohapatra, S.R., Sudarsanan, N., Rajagopal K., and Robinson R. G., 2017. A simple image-based deformation measurement technique in tensile testing of geotextiles. Geosynthetics International, 1-15.

Moriyama, T., Kochi, N., Yamada, M., & Fukaya, N. (2008). Automatic target-identification with the color-coded-targets. In The International Archives of Photogrammetry and Remote Sensing, Beijing, XXI Congress, WG (Vol. 1, pp. 39-44)

Ng, C.W., Zhan, L., and Cui, Y. 2002. A new simple system for measuring volume changes in unsaturated soils, Canadian Geotechnical Journal, 39(3): 757-764.

Nieder€ost, M.andMaas, H.-G. (1997). Automatic deformation measurement with a digital still video camera. Optical 3-D Measurement Techniques IV(Eds.A. Gruen &H. Kahmen). Wichmann, Heidelberg, Germany. 266–271.

Nöll, T., Pagani, A., & Stricker, D. (2011). Markerless camera pose estimation-an overview. In OASIcs-OpenAccess Series in Informatics (Vol. 19). Schloss Dagstuhl-Leibniz-Zentrum fuer Informatik.

Parker, J. K. 1987. Image processing and analysis for the mechanics of granular materials experiment. In ASME Proceedings of the 19th SE Symposium on System Theory, Nashville.

Rampino C, Mancuso C, Vinale F (1999) Laboratory testing on an unsaturated soil: equipment, procedures, and first experimental results. Canadian Geotechnical Journal, 36(1):1-12.

Rechenmacher, A. L. 2006. Grain-scale processes governing shear band initiation and evolution in sands. Journal of the Mechanics and Physics of Solids, 54(1): 22-45.

Rechenmacher, A. L., and Medina-Cetina, Z. 2007. Calibration of soil constitutive models with spatially varying parameters. Journal of Geotechnical and Geoenvironmental Engineering, 133(12): 1567-1576.

Rechenmacher, A., and Saab, N. 2002. Digital image correlation (DIC) to evaluate progression and uniformity of shear bands in dilative sands. In 15th ASCE Engineering Mechanics Conference, Columbia University, NY. June 5.Remondino, F. (2006). Detectors and descriptors for photogrammetric applications.International Archives of Photogrammetry, Remote Sensing and Spatial Information Sciences, 36(3): 49–54.

Ren, S., He, K., Girshick, R., and Sun, J. (2015). Faster R-CNN: Towards real-time object detection with region proposal networks. Proc., Advances in Neural Information Processing Systems, Neural Information Processing Systems Foundation, Montréal, 91–99.

Romero, E., Facio, J., Lloret, A., Gens, A., and Alonso, E. 1997. A new suction and temperature controlled triaxial apparatus. Proceedings of the 14th International Conference on Soil

Mechanics and Foundation Engineering, Vol. 1, Hamburg, Germany, September 6-12, pp. 185-188.

Sachan, A., and Penumadu, D. 2007. Strain localization in solid cylindrical clay specimens using digital image analysis (DIA) technique. Soils and Foundations, 47(1): 67-78.

Salazar, S. E., & Coffman, R. A. (2014). Consideration of internal board camera optics for triaxial testing applications. Geotechnical Testing Journal, 38(1), 40-49.

Scaioni, M., Feng, T., Barazzetti, L., Previtali, M., & Roncella, R. (2015). Image-based deformation measurement. Applied Geomatics, 7(2), 75-90.

Schneider, C.-T.andSinnreich, K. (1992). Optical 3-D measurement systems for quality control in industry. International Archives of Photogrammetry and Remote Sensing, 29(B5): 56–59.

Sermanet, P., Eigen, D., Zhang, X., Mathieu, M., Fergus, R., & LeCun, Y. (2013). Overfeat: Integrated recognition, localization and detection using convolutional networks. arXiv preprint arXiv:1312.6229.

Sharma, R. S., Hong, L., and Singhal, S. 2006. Developments in measurement of volume change in triaxial testing of unsaturated soils. In Advances in Unsaturated Soil, Seepage, and Environmental Geotechnics, ASCE, pp. 93-101. doi: 10.1061/40860(192)8.

Shortis, M. R., Clarke, T. A.andShort, T. (1994). Comparison of some techniques for the subpixel location of discrete target images. Videometrics III, SPIE, 2350: 239–250.Shortis, M. R., & Seager, J. W. (2014). A practical target recognition system for close range photogrammetry. The Photogrammetric Record, 29(147), 337-355.

Simonyan, K., and Zisserman, A. (2015). Very deep convolutional networks for large-scale image recognition. Proc., Int. Conf. on Learning Representations, Cornell Univ. Library, San Diego, 1–14.

Skochdopole, T. R., Cassady, L., Pihs, D., and Stevenson, P. E., 2000. Comparative Study of Roller and Wedge Grips for Tensile Testing of High Strength Fabrics with Laser Extensometry: Comparisons to LVDT and Crosshead Extension. Grips, Clamps, Clamping Techniques, and Strain Measurement for Testing of Geosynthetics. ASTM International.

Taketomi, T., Okada, K., Yamamoto, G., Miyazaki, J., & Kato, H. (2014). Camera pose estimation under dynamic intrinsic parameter change for augmented reality. Computers & Graphics, 44, 11-19.

Tsai, R, 1987. A versatile camera calibration technique for high-accuracy 3D machine vision metrology using off-the-shelf TV cameras and lenses. IEEE Journal on Robotics and Automation, 3(4), 323-344.

Uijlings, J. R., van de Sande, K. E., Gevers, T., and Smeulders, A. W. (2013). Selective search for object recognition. Int. J. Comput. Vision, 104(2), 154–171.

Van den Heuvel, F. A. Kroon, R. J. G. A., and Le Poole, R. S. (1992). Digital close-range photogrammetry using artificial targets. International Archives of Photogrammetry and Remote Sensing,29(B5): 222–229.

Wheeler, S. 1988. The undrained shear strength of soils containing large gas bubbles, Géotechnique, 38(3): 399-413.

White, D., Randolph, M. F., and Thompson, B. 2005. An image-based deformation measurement system for the geotechnical centrifuge. International Journal of Physical Modelling in Geotechnics, 5(3): 1-12.

William A. Hoff. (2014). Epipolar Geometry and the Essential Matrix [PowerPoint slides]. Retrieved from http://inside.mines.edu/~whoff/courses/E

ENG512/lectures/EpipolarAndEssential.pdf.

Wolf, P. R., & Dewitt, B. A. (2000). Elements of photogrammetry: with applications in GIS (Vol. 3). New York: McGraw-Hill.

Yang, G., Li, Q. J., Zhan, Y., Fei, Y., & Zhang, A. (2018). Convolutional Neural Network–Based Friction Model Using Pavement Texture Data. Journal of Computing in Civil Engineering, 32(6), 04018052.

Zatarain, M., Mendikute, A., & Inziarte, I. (2012). Raw part characterisation and automated alignment by means of a photogrammetric approach. CIRP annals, 61(1), 383-386.

Zeng, H. (2010). Iterative algorithm of space resection using Rodrigues matrix. In Environmental Science and Information Application Technology (ESIAT), 2010 International Conference on 191-194. IEEE.

Zhang, X., Li, L., Chen, G., & Lytton, R. (2015). A photogrammetry-based method to measure total and local volume changes of unsaturated soils during triaxial testing. Acta Geotechnica, 10(1), 55-82.

Zhang, Z. (2000). A flexible new technique for camera calibration. IEEE Transactions on pattern analysis and machine intelligence, 22(11), 1330-1334.